

# $C_{60}$ as a template for the creation of metal and semiconductor nanoclusters

**Dissertation**

zur Erlangung des Doktorgrades  
der Mathematisch-Naturwissenschaftlichen Fakultäten  
der Georg-August-Universität zu Göttingen

vorgelegt von  
Helge Kröger  
aus Flensburg

Göttingen, 2005

D 7

Referent: Prof. Dr. Petra Reinke

Koreferent: Prof. Dr. Reiner Kirchheim

Tag der mündlichen Prüfung: 13.12.2005

# Contents

<b>1</b>	<b>Introduction</b>	<b>3</b>
<b>2</b>	<b>Material properties</b>	<b>6</b>
2.1	Fullerene molecules . . . . .	6
2.1.1	History of $C_{60}$ . . . . .	6
2.1.2	Material properties of $C_{60}$ molecules . . . . .	8
2.1.3	Properties of crystalline fullerene solids . . . . .	12
2.2	Properties of metal and semiconductor clusters . . . . .	15
2.2.1	Materials investigated within this work . . . . .	20
2.3	Interaction of $C_{60}$ and foreign atoms or clusters . . . . .	22
2.3.1	Endohedral doping . . . . .	22
2.3.2	Substitutional doping . . . . .	23
2.3.3	Exohedral doping . . . . .	23
<b>3</b>	<b>Methods</b>	<b>26</b>
3.1	UHV chamber and sample synthesis . . . . .	26
3.2	Photoelectron spectroscopy . . . . .	29
3.2.1	Theory of photoemission . . . . .	34
3.3	UV-VIS spectroscopy . . . . .	40
3.4	Photoluminescence measurements . . . . .	42
3.5	Transmission electron microscopy . . . . .	44
3.6	Atomic force microscopy . . . . .	45
3.7	Rutherford backscattering . . . . .	47
<b>4</b>	<b>2D systems</b>	<b>49</b>
4.1	Gold . . . . .	49
4.1.1	Conclusions . . . . .	62
4.2	Vanadium . . . . .	63
4.2.1	Conclusions . . . . .	79
<b>5</b>	<b>3D systems</b>	<b>82</b>
5.1	Gold . . . . .	82

5.1.1	Conclusions . . . . .	94
5.2	Germanium and iron . . . . .	95
<b>6</b>	<b>Summary and outlook</b>	<b>100</b>
	<b>List of Figures</b>	<b>106</b>
	<b>List of Tables</b>	<b>109</b>
	<b>References</b>	<b>110</b>
	<b>Acknowledgments</b>	<b>125</b>
	<b>Lebenslauf</b>	<b>127</b>

# 1 Introduction

Nanotechnology is a field of growing importance. The driving force behind the search for nanosize materials is the continuing demand for a decrease in size and dimension of electronic devices and storage media, while at the same time optimizing the performance of those devices. With the reduction of size and dimension, these materials develop unique properties, which can be very different from those of the corresponding bulk materials. The properties of very small clusters (a few atoms up to a few hundred atoms) are due to quantum size effects (see chapter 2.2). Metal and semiconductor clusters can have a strong influence on the mechanical and optical properties of composite materials (for a review see [1]). This influence is due to the electronic structure, which is determined by the number of atoms in the cluster. The resulting electron confining potential in turn is defined by the cluster-substrate and the cluster-vacuum interface [2, 3, 4, 5]. As the size of the cluster is of great importance to its physical properties, this poses considerable challenges for their synthesis [6]. To optimize these properties it is important to understand the cluster-substrate (or cluster-ligand) interaction [2].

One goal in this endeavor for nanoscale devices is the creation of cluster arrays of single size clusters. Ideally, this cluster array should grow by self organization. For this a suitable substrate has to be found. A possible candidate for such a substrate are the highly stable, covalently bonded carbon fullerenes [7]. The highly symmetric  $C_{60}$  molecule is of interest due to its unique structure (see chapter 2.1). It is the only known pure van der Waals crystal and the surface of a  $C_{60}$  film provides a lattice of troughs (the interstitial vacancies) in between the molecules, which are large enough to contain clusters of up to 20 atoms. By exploiting the properties of these large round, chemically inert molecules it is possible to explore cluster arrays in a two and three dimensional matrix (surface and bulk) [8, 9, 10, 11].

The growth behavior of a given material on the  $C_{60}$  surface is driven by topography, ad-atom mobility, and preference in bonding environment. A wide range of variability in cluster nucleation and overlayer growth can be expected. In order to form cluster arrays in a controlled manner the troughs have to function as primary nucleation centers and favorable bonding sites. The fullerene layer itself can adopt a crystalline or disordered structure, which is mirrored in the overall organization

of the final cluster array. A recent study showed that, in the case of Si, the troughs indeed perform as preferred adsorption sites for Si atoms and the fullerene surface functions as a template [12].

The possibility of creating a fullerene-silicon fulleride by co-deposition of  $C_{60}$  and Si has been demonstrated [13] and it could be shown that the 2D system (deposition of Si on a  $C_{60}$  surface) is a valuable model system to investigate the interface chemistry, electronic properties, and Si bonding sites. The long term goal of the present investigation is to understand the metal/semiconductor - fullerene interactions and to form two and three dimensional cluster arrays or fulleride materials (comprised of carbon fullerenes and another element) from a variety of elements.

The overlayer growth of the 2D system can provide valuable information on the possible formation of clusters and is investigated for gold and vanadium (see chapter 4). Metallic nanoclusters are especially of interest, as they show considerable potential for application in nanoelectronic devices [14]. Au in particular is chosen as an example for a d-metal in this investigation (see chapter 4.1), because numerous studies are devoted to Au clusters on varying (mostly semi-conducting) substrates [15, 16, 17, 18, 19, 20, 21, 22]. A second material of interest is vanadium (see chapter 4.2), as vanadium oxides are widely used as catalysts [23, 24, 25, 26, 27, 28, 29, 30]. The overlayer/cluster formation for these two systems is investigated by observing the early stages of growth, covering the range of 0.01 *nm* up to a few nanometers with photoelectron spectroscopy. The highly reactive vanadium offers the possibility of investigating a further aspect of interest in creating nano catalysts within a fullerene matrix, which is the permeability of a  $C_{60}$  film with respect to oxygen. This can be achieved by studying the oxidation of a vanadium layer buried under a few nanometers of fullerenes (see chapter 4.2).

The possible creation of clusters on a fullerene surface is only the first step in creating either an array of clusters within a fullerene matrix or the formation of a binary cluster material. Combinations of fullerenes with other elements can be achieved through endohedral doping (see chapter 2.3.1), substitutional doping (see chapter 2.3.2), and exohedral doping (see chapter 2.3.3). This considerably expands the properties and thereby the potential usefulness of fullerenes. The formation of clusters in a fullerene matrix in some ways resembles exohedral doping. Selected sites of the fullerene lattice are employed to incorporate foreign atoms outside the

---

$C_{60}$  cage. The highest concentration of a dopant achieved in this manner so far is  $Na_{11}C_{60}$  [31]. Exohedrally doped fullerenes are also known as fullerides. They represent novel materials with intriguing and surprising new properties, like, for example, the superconductivity of  $K_3C_{60}$  [32]. These ionic fullerides with alkali and some earth alkalis have been proven to be thermodynamically stable [33, 34]. For other possible dopants like transition metals, the stability has yet to be shown. Thermodynamical considerations for these materials indicate that, due to the large cohesive energies, segregation is favored. Therefore, a kinetically driven synthesis route may be the only feasible one. Fullerides with Ti, Yb, and Nb have been created by rapid condensation of the reactants from the gas phase [35, 36, 37, 38]. This suggests the general possibility of creating fullerides and similar non-ionic materials comprised of a wide range of elements.

The extension to 3-dimensional composite samples resembling fullerides is attempted for different materials (see chapter 5). The fullerene films provide a dielectric matrix for the possible formation of clusters. In case of gold for example, the size of the clusters is an important factor not only for the optical properties, but also, for example, in their usefulness as a catalyst [39]. Therefore, it is important to be able to control their size and distribution within the dielectric matrix. To investigate this aspect, samples with varying Au concentrations have been deposited and examined with transmission electron microscopy and Rutherford backscattering spectroscopy. Further information on the topography of these composite samples can be gained by atomic force microscopy.

Small metal and semiconductor clusters are known to have interesting optical properties like photoluminescence, for example. As fullerenes possess an indigenous luminescence, the composite materials could be of interest as opto-electronic devices. The semiconductor germanium is an especially interesting candidate for a luminescent material, because germanium nanocrystals show strong quantum size effects for relatively large structures [40]. The optical properties of fullerene-germanium composite samples are investigated by means of photoluminescence measurements as well as UV-VIS spectroscopy (see chapter 5.2). Since germanium is chemically very similar to silicon, the promising results with silicon [12, 13] encourage an attempt at creating germanium clusters in the same manner.

## 2 Material properties

In this chapter the properties of the materials used throughout the experiments described in this work will be summarized. In particular an overview of the unique properties of the third carbon allotrope, the fullerene molecule, will be given, as this is the main component in all the samples created in this work.

### 2.1 Fullerene molecules

#### 2.1.1 History of $C_{60}$

Fullerene molecules are made up of carbon atoms. The most abundant one (and best known) is the  $C_{60}$  molecule, which is a regular truncated icosahedron. This shape was already known to Leonardo da Vinci in about 1500 [41, 42]. Fig. 1 shows a representation attributed to Leonardo da Vinci alongside a representation of the structure of a  $C_{60}$  molecule. In the early 20th century, some theoretical work was done on the point group symmetry of these icosahedral molecules [43],

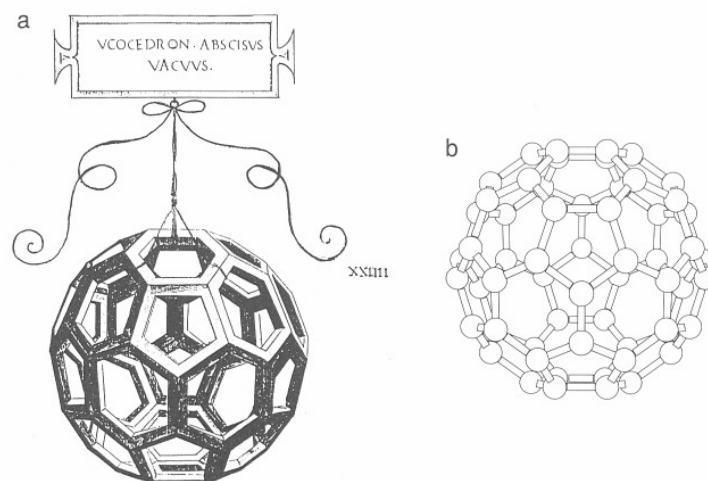


Figure 1: a: Regular truncated icosahedron from an Italian translation of the "Liberus" published in 1509 by the mathematician Luca Pacioli in his book "De Divina Proportione". The design is thought to be by Leonardo da Vinci [41, 42]. b: In the  $C_{60}$  molecule each carbon atom is at an equivalent position on the corners of a regular truncated icosahedron (taken from ref [7].)



decades before they were actually found in laboratory experiments [44]. The first hint of their existence was actually discovered by astrophysicists, who found unusual infrared (IR) emissions in the spectra of red giant carbon stars [45, 46, 47]. During the same period (at Rice University) a laser vaporization technique was developed by Smalley and co-workers for synthesizing clusters, and in particular carbon clusters [48]. These experiments offered the possibility of creating the same kind of molecules that had been discovered in the IR spectra of the red giant stars. This led to a collaboration between Kroto and Smalley and co-workers, and it was during this collaboration that a 60 carbon atom cluster with unusual stability was discovered [49, 50]. Shortly thereafter it was proposed that  $C_{60}$  was indeed a molecule with icosahedral symmetry [44]. What is so special about the  $C_{60}$  molecule, is that in the cage structure made up of pentagons and hexagons with carbon atoms at the 60 vertices of the regular truncated icosahedron, the carbon atoms have no dangling bonds. The pentagons are isolated from each other, thus creating greater electronic and chemical stability. This exceptional stability is noteworthy as it enables the molecule to withstand temperatures of up to 1000 °C as well as collisions with other species within an energy range of hundreds of eV. It is the largest stable molecule made up of only one element. A stereographic projection of a  $C_{60}$  molecule is given in fig. 2.

The name given by Kroto and Smalley to the family of molecules with cage-structure in the gas phase is "fullerene". The name "buckminsterfullerene" or simply "buckyball" was given specifically to the  $C_{60}$  molecule. The name was chosen because of the likeness of the molecules to the geodesic domes designed and built by R. Buckminster Fuller [51, 52, 53], an example of which can be seen in the left part of fig. 3. The Right part shows a US stamp, released in honor of R. Buckminster Fuller, showing a small range of things he thought about or invented during his lifetime. As dome-shaped structures provide maximum volume for minimal surface area combined with a relatively strong structure, they have found widespread use all over the world. Also, in biology and biochemistry there are a lot of examples for molecules or microstructures with fivefold symmetry axes, comparable to those found in a  $C_{60}$  molecule. Many living systems are made up on the nanometer scale of structures exhibiting this fivefold symmetry, self-assembled in intriguing ways to fulfil very specific functions [54]. Studying these natural materials could provide us

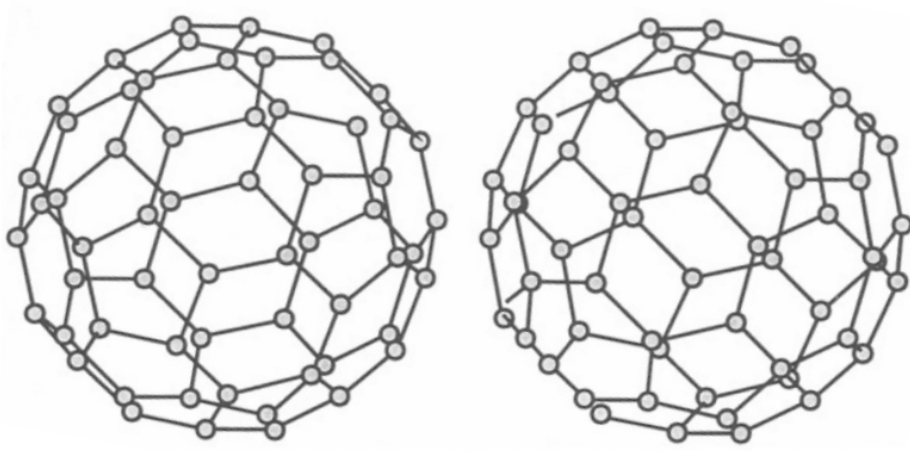


Figure 2: Stereographic projection of  $C_{60}$ . To visualize the 3D image the picture must be held at about 15 cm from the eyes and the eyes must focus at infinity (taken from ref. [7]).

with insight into how to achieve self-assembled nanometer-scale materials.

### 2.1.2 Material properties of $C_{60}$ molecules

Any closed cage molecule made up of only pentagonal and hexagonal faces is a fullerene. For this there have to be exactly 12 pentagonal faces and an arbitrary number  $h$  of hexagonal faces. This was first concluded by Euler in the theorem for polyhedra

$$f + v = e + 2 \quad (1)$$

where  $f$ ,  $v$ , and  $e$  are the numbers of faces, vertices, and edges of the polyhedra, respectively. Considering polyhedra comprising of  $h$  hexagonal and  $p$  pentagonal faces leads to

$$\begin{aligned} f &= p + h \\ 2e &= 5p + 6h \\ 3v &= 5p + 6h \end{aligned} \quad (2)$$

These three relations yield

$$6(f + v - e) = p = 12 \quad (3)$$

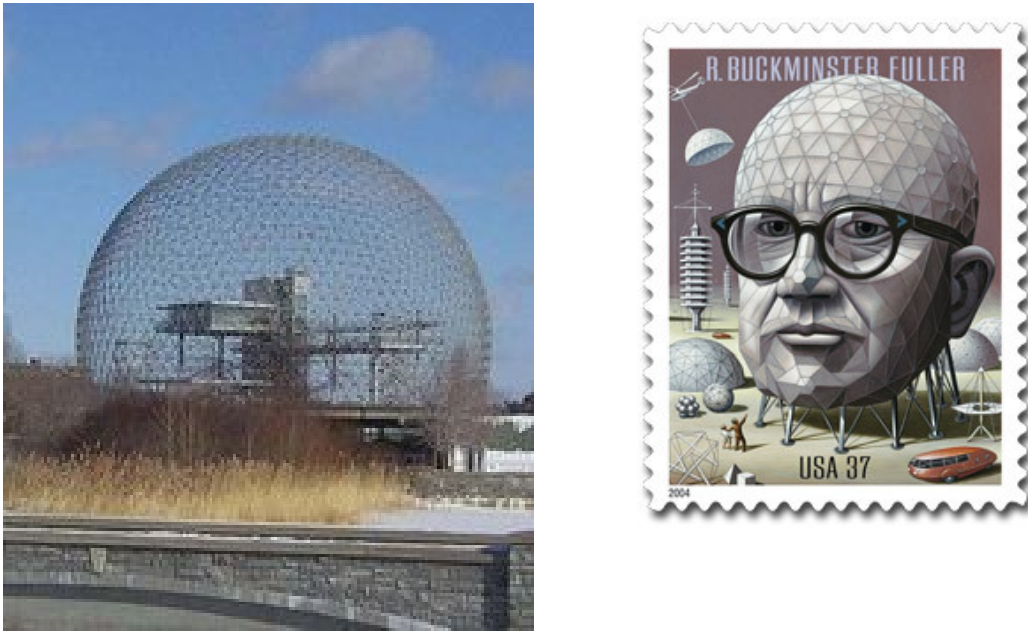


Figure 3: Left: The American pavilion of the Expo 1967 in Montreal, designed by Buckminster Fuller, which today is the home of the Biosphere. Right: In the US postage stamp commemorating Buckminster Fuller and his contributions to architecture and science, some of his inventions are visible. Most notably, his head is shaped after one of his geodesic domes (pictures taken from [www.wikipedia.org](http://www.wikipedia.org)).

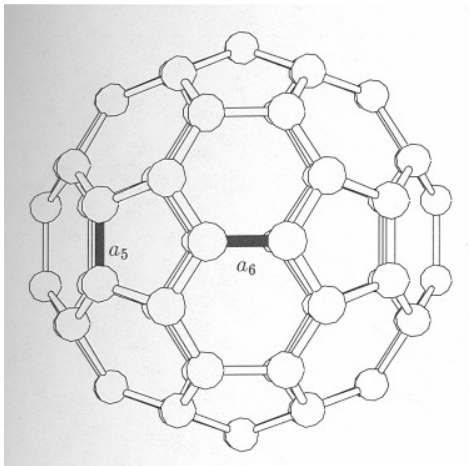


Figure 4:  $C_{60}$  molecule, showing single bonds ( $a_5$ ) and double bonds ( $a_6$ ) (taken from ref. [7]).

from which it can be concluded, that all fullerenes with only hexagonal and pentagonal faces must have exactly 12 pentagonal faces, whereas the number of hexagonal faces is arbitrary. It is energetically less favorable to have adjacent pentagons within the molecule, because this introduces a stronger local curvature and therefore more strain. This leads directly to the so called "isolated pentagon rule", which suggests higher stability for molecules in which the pentagons are separated from one another by hexagons. The smallest fullerene molecule satisfying the isolated pentagon rule

is  $C_{60}$ . Fullerenes with fewer carbon atoms are generally not found in the soot com-

monly used for extracting fullerenes. The ones that have been produced require stabilization by saturating dangling bonds with hydrogen, one example is  $C_{20}H_{20}$  [55].

Even though all carbon atoms in the molecule are considered to be equal, there is a slight difference in the bonds emanating from each atom. Two of them are electron-poor single bonds located on the pentagonal edges, while the other one is an electron-rich double bond that joins two hexagonal faces. This alternating bond structure located around the hexagonal faces is known as the Kekulé structure, and is illustrated in fig. 4. The bond lengths of the  $a_5$  single bonds are 1.46 Å, whereas the  $a_6$  double bond has a length of 1.40 Å. As the bonding requirements of all valence electrons are satisfied, it is to be assumed that  $C_{60}$  has filled molecular orbitals. Because of the closed shell of the  $C_{60}$  molecule, the  $sp^2$  bonding of adjacent carbon atoms takes place on a curved surface. This curvature leads to a slight admixture of  $sp^3$  bonding, characteristic of diamond and absent in planar graphite. An overview of the physical constants of the  $C_{60}$  molecule is given in table 1.

On the one hand, as the cage structure produces a very small value for the nearest neighbor carbon-carbon distance in  $C_{60}$ , it is to be expected that the molecule is nearly incompressible [67]. On the other hand, in the solid state the large van der Waals spacings between the molecules results in a soft and compressible solid [68].

In the following, we will take a look at the reactivity of the  $C_{60}$  molecule. Due to its double bonds, chemists often classify  $C_{60}$  as an alkene. But as the molecule consists of pentagons as well as hexagons, most chemists would not generally classify it as aromatic, because those are ring molecules with alternating single and double bonds that resonate with one another [69]. Also, the delocalization is an important characteristic of aromatic molecules. The pentagons in  $C_{60}$  localize the double bonds at specific sites, which sets the molecule apart from aromatic molecules like benzene, in which the  $\pi$  electrons are delocalized around the hexagonal ring. Double bonds are believed to be absent in the pentagons due to the attendant strain energy [70]. For an alkene molecule,  $C_{60}$  has an unusual amount of equivalent reaction sites, one for each double bond. This leads to a large number of possible reaction products, which are the result of the reaction of a single reagent. Due to this, most reactions with fullerenes are not selective.

In general, fullerenes are electrophilic, they attract electrons [70, 71]. Therefore, chemical reactions with nucleophiles (electron donating species) are preferred. This also means, that  $C_{60}$  is easily reduced, which is why fullerenes are considered to be mild oxidizing agents. Other possible reactions include functionalization of the molecules by attaching different chemical groups, which in turn may allow further reactions. Some general categories of chemical reactions occurring for  $C_{60}$  are shown in fig. 5. In this figure, the various fullerene derivatives have been grouped according to their structural similarities. From this three main groups can be identified. About half of the reaction products are derived from either hydrogenation, alkylation or amination. All of these reactions result in a radial covalent bond between the  $C_{60}$  and the adduct. A second group in the figure is made up of derivatives, which are formed by attaching an adduct by means of a bridge whose ends are bonded across the reactive double bond in a pyracylene unit of the  $C_{60}$  molecule. It is also possible to attach multiple larger adducts of the same type in this manner. This way, one

Table 1: Physical constants for  $C_{60}$  molecules.

Quantity	Value	Reference
Average C-C distance	1.44 Å	[56]
C-C bond length on a pentagon	1.46 Å	[57]
C-C bond length on a hexagon	1.40 Å	[57]
$C_{60}$ mean ball diameter <sup>a</sup>	7.10 Å	[58]
$C_{60}$ outer diameter <sup>b</sup>	10.34 Å	-
Moment of inertia $I$	$1.0 \cdot 10^{-43} \text{kgm}^2$	[59]
Volume per $C_{60}$	$1.87 \cdot 10^{-22} \text{cm}^3$	-
Number of distinct C sites	1	-
Number of distinct C-C bonds	2	-
Binding energy per atom <sup>c</sup>	7.4 eV	[60]
Heat of formation (per g C atom)	10.16 kcal	[61]
Electron affinity	$2.65 \pm 0.05 \text{ eV}$	[62]
Cohesive energy per C atom	1.4 eV/atom	[63]
Spin-orbit splitting of C(2p)	0.00022 eV	[64]
First ionization potential	7.58 eV	[65]
Second ionization potential	11.5 eV	[66]
Optical absorption edge <sup>d</sup>	1.65 eV	[60]

a) Determined by NMR, the calculated geometric value is 7.09 Å

- b) This value for the outer diameter is found by assuming the thickness of the  $C_{60}$  shell to be 3.35 Å. In the solid, the  $C_{60} - C_{60}$  nearest neighbor distance is 10.02 Å.
- c) The binding energy of  $C_{60}$  is believed to be  $\sim 0.7 \text{ eV/C}$  atom less than for graphite, though literature values for both are given as 7.4 eV/C atom. The reason for the apparent inconsistency is attributed to differences in calculational techniques.
- d) Literature values for the optical absorption edge for free  $C_{60}$  molecules in solution range from 1.55 eV to 2.3 eV.

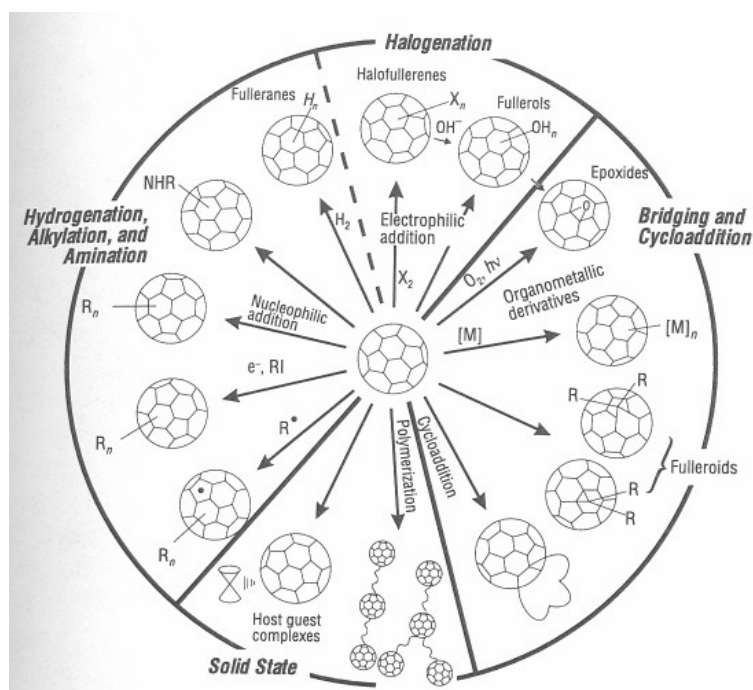


Figure 5: Some general categories of reactions known to occur with  $C_{60}$ , taken from ref. [7], based on a figure from ref. [70].

reagent can generate a variety of different fullerene derivatives, which only differ in the number of adducts. The last group in fig. 5 consists of the derivatives that are usually associated with the solid state, like polymers, so called host-guest solids, clathrates and intercalation compounds like  $K_xC_{60}$ , which will be discussed briefly in the next section. More detailed information on the specific chemical reactions involving  $C_{60}$  can be found in reference [7] and the references therein.

### 2.1.3 Properties of crystalline fullerene solids

First of all it should be mentioned, that all of the attributes of the cubic structure described here have been established for single crystals grown from vapor sublimation of  $C_{60}$  molecules. At room temperature, solid  $C_{60}$  crystallizes into a cubic structure with a lattice constant of  $14.17 \text{ \AA}$  and a nearest neighbor distance of  $10.02 \text{ \AA}$  [72]. In this state, it has a density of  $1.72 \text{ g/cm}^3$ , corresponding to  $1.44 \cdot 10^{21} C_{60}$  molecules/ $\text{cm}^3$  (see table 2).

Table 2: Physical constants for crystalline  $C_{60}$  in the solid state

Quantity	Value	Reference
<i>fcc</i> lattice constant	14.17 Å	[73]
$C_{60} - C_{60}$ distance	10.02 Å	[72]
$C_{60} - C_{60}$ cohesive energy	1.6 eV	[74]
Tetrahedral interstitial site radius	1.12 Å	[72]
Octahedral interstitial site radius	2.07 Å	[72]
Mass density	1.72 g/cm <sup>3</sup>	[72]
Molecular density	1.44 · 10 <sup>21</sup> /cm <sup>3</sup>	[72]
Compressibility ( $-d \ln V/dP$ )	6.9 · 10 <sup>-12</sup> cm <sup>2</sup> /dyn	[75]
Bulk modulus <sup>a</sup>	6.8, 6.8 GPa	[76, 77]
Young's modulus <sup>b</sup>	15.9 GPa	[78]
Transition temperature ( $T_{01}$ ) <sup>c</sup>	261 K	[79]
$dT_{01}/dp$ <sup>c</sup>	11 K/kbar	[80, 81]
Vol. coeff. of thermal expansion	6.1 · 10 <sup>-5</sup> /K	[82]
Optical absorption edge	1.7 eV	[83]
Work function	4.7 ± 0.1 eV	[84]
Velocity of sound $v_t$	2.1 · 10 <sup>5</sup> cm/s	[78]
Velocity of sound $v_l$	3.6 – 4.3 · 10 <sup>5</sup> cm/s	[78, 85]
Debye temperature	185 K	[86, 87]
Thermal conductivity (300 K)	0.4 W/mK	[88]
Electrical conductivity (300 K)	1.7 · 10 <sup>-7</sup> S/cm	[89]
Phonon mean free path	50 Å	[88]
Static dielectric constant	4.0 – 4.5	[90, 91]
Melting temperature	1180 °C	[92]
Sublimation temperature	434 °C	[93]
Heat of sublimation	40.1 kcal/mol	[93]
Latent heat	1.65 eV/ $C_{60}$	[94]

- a) The bulk modulus is 6.8 GPa at room temperature in the *fcc* phase and 8.8 GPa in the *sc* phase below  $T_{01}$  [76]. Earlier reported values for the bulk modulus were in the range 14 – 18 GPa [75, 95, 68, 96]. The conversion of units for pressure measurements is 1 GPa = 10<sup>9</sup> N/m<sup>2</sup> = 0.99 kbar = 7.52 · 10<sup>6</sup> torr = 10<sup>10</sup> dyn/cm<sup>2</sup>. Also, 1 atm = 760 torr = 1.01 · 10<sup>5</sup> Pa.
- b) For solvated  $C_{60}$  crystals measured by vibrating reed method [78]. Measurements on film samples suggest a higher Young's modulus [97].
- c) Structural phase transition

It has been shown by nuclear magnetic resonance (NMR), that  $C_{60}$  molecules in the molecular solid are rotating rapidly [98, 99, 100, 101, 102]. They have three degrees of freedom, and the molecular centers are arranged on a face-centered cubic (*fcc*) lattice. In this arrangement, there is one  $C_{60}$  molecule in each primitive *fcc* unit cell, or four molecules per simple cubic unit cell. There is no orientational order to the crystal, because the molecules are rapidly spinning about their position in the lattice. All measurements, performed for a time that is long compared to the average rotational period of 10<sup>-11</sup> s of the molecules, show them all to be equivalent. This makes the pertinent space group for the rapidly rotating molecules  $O_h^5$  or  $Fm\bar{3}m$ , using Schoenflies or International Crystallographic nomenclature

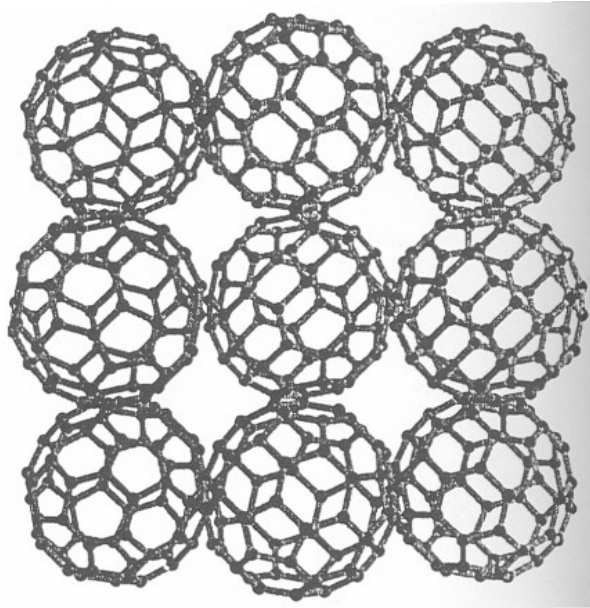


Figure 6: Basal plane projection of the low temperature crystal structure of solid  $C_{60}$  (space group  $Pa\bar{3}$ ) [103] (taken from ref. [7]).

respectively. At room temperature, it has been possible to directly measure the space group employing x-ray and neutron diffraction [82, 104, 105]. Investigation of the room temperature crystal structure with x-ray diffraction (XRD) has also shown that there are some orientational correlations between adjacent  $C_{60}$  molecules [106, 107]. This is consistent with a rapid ratcheting motion model, as opposed to a constant angular momentum rotation. At room temperature, the rotational re-orientation time, based on NMR, is  $9 - 12$  ps [98, 99, 101, 57, 108].

Compared to graphite, solid  $C_{60}$  is about three times as compressible. It has an isothermal volume compressibility of  $6.9 \cdot 10^{-12} \text{ cm}^2/\text{dyn}$  [75]. This is due to the electron cloud around the  $C_{60}$  molecules, which can be compressed in three dimensions more easily than the van der Waals bond in one dimension in the case of graphite.

The room temperature crystal structure persists down to temperature  $T_{01} = 261 \text{ K}$ , at which there is a phase transition to a simple cubic (sc) phase. The molecules lose two of their three degrees of rotational freedom below  $T_{01}$ . The rotation occurs around the four  $\langle 111 \rangle$  axes, and therefore is a hindered rotation.



Adjacent fullerene molecules develop strongly correlated orientations [82, 105, 109, 110], and the orientation along the cubic crystalline axes becomes important in the ordered phase. The simple cubic phase has space group  $T_h^6$  or  $Pa\bar{3}$ , as seen in fig. 6, with lattice constant  $a_0 = 14.17 \text{ \AA}$  and four  $C_{60}$  molecules per unit cell, because the molecules within the fcc structure become inequivalent below  $T_{01}$  [82, 105]. Physically, the lowering of the crystal symmetry is caused by an assignment of a specific  $\langle 111 \rangle$  direction vector to each of the four molecules in the unit cell. This causes the reduction of the rotational freedom from practically free rotation down to a rotation about a specific threefold axis. This freezing of the rotational degrees of freedom has consequences for many physical properties of crystalline  $C_{60}$ . Anomalies are detected in many property measurements like XRD [111], differential scanning calorimetry [112], specific heat [86, 113, 114], electrical resistivity [115], NMR [98, 99, 101, 112, 116, 57, 58], inelastic neutron scattering [56, 117, 118, 119], electron diffraction [120], sound velocity and ultrasonic attenuation [78, 121], elastic properties [122], Raman spectroscopy [123, 124, 125, 126], thermal conductivity [88], and the thermal coefficient of lattice expansion [82, 127]. As the temperature is lowered further, there is a second phase transition at a temperature  $T_{02}$ , which is caused by an alignment of the molecules in such a way, that electron-rich double bonds are placed opposite electron-poor single bonds. However, the value of  $T_{02}$  depends on the property being measured and on the time required for the excitation to make the measurement [122]. The value is somewhere between 90  $K$  and 165  $K$ . Evidence for the phase transition has been observed in many different experiments, such as studying velocity of sound and ultrasonic attenuation [78, 121], specific heat [86, 114], thermal conductivity [88], elasticity [78, 122, 121], high-resolution capacitance dilatometry [127], Raman scattering [123, 126], and neutron scattering [109, 110], to name just a few.

## 2.2 Properties of metal and semiconductor clusters

Small particles have been of interest for centuries. Even the artisans of the middle ages knew about the effect the introduction of metal into their stained glasses had on the color. They developed elaborate recipes for introducing gold into glass to obtain specific desired colors. Faraday studied the size effects of colloidal gold particles,

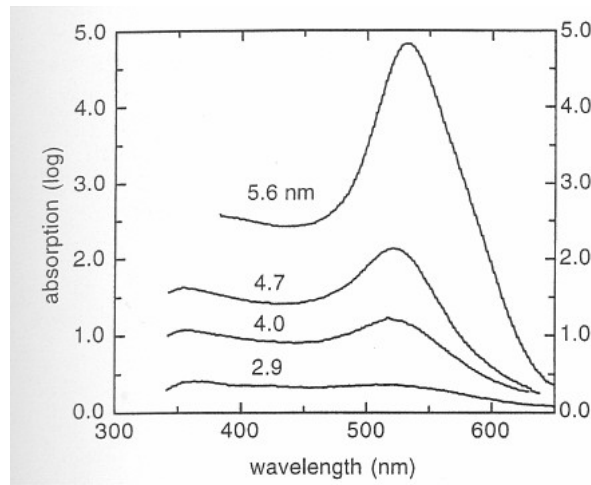


Figure 7: Several examples of measured optical absorption spectra of small gold particles imbedded in a noble gas matrix showing evidence of a single large absorption peak which is identified as the plasma resonance (taken from ref. [140]).

whilst he was looking for effects of the hypothetical ether, which should have been brought forward due to the reduced size. Although he missed his intended goal, he still succeeded in finding size effects due to the reduced dimensionality, namely the red color of colloidal gold and the colors of thin films due to surface plasmons. The effects remained unexplained until the electrodynamics were theoretically analyzed by Rayleigh and Mie [128]. The interest in small nano-size particles has significantly increased in the last two decades, and many reviews on the subject are available [129, 130, 131, 132, 133, 134, 135, 136].

Considering the free electron picture, one can use the Drude dielectric function [137] to determine the resonance frequency  $\omega_r$  for a spherical metal particle with  $N$  electrons and a radius  $R$ , which is much smaller than the wavelength:

$$\omega_r = Ne^2/m_e R^3 \quad (4)$$

in which  $m_e$  is the electron mass. This equation, however, is only applicable for simple metals. Noble metals require an important contribution from the d band electrons [138, 139]. Specifically gold was investigated, as gold nanoparticles had been used for centuries. Some experimental results from absorption measurements performed on Au nanoparticles [139] in a noble gas environment are shown in fig. 7.

If the particle size is much smaller than the excitation wavelength, then according to Mie's theory, one maximum of the absorption cross section should be at the surface plasma resonance. It is related to the dielectric function via

$$\sigma(\omega) = C(R)\omega\epsilon_2/[(\epsilon_1 + 2)^2 + \epsilon_2^2] \quad (5)$$

where  $\epsilon_1$  and  $\epsilon_2$  are the real and imaginary parts of the dielectric function of the material.  $C(R)$  is a constant which is independent of  $\omega$  [138, 141], therefore there is a peak in the absorption for  $\epsilon_1 = -2$ . Furthermore, the Drude model [138] predicts that

$$\begin{aligned} \epsilon_1 &= 1 - \omega_p^2/(\omega^2 + \Gamma^2) \\ \epsilon_2 &= \omega_p^2\Gamma/(\omega^3 + \omega\Gamma^2) \end{aligned} \quad (6)$$

with the square of the plasma frequency  $\omega_p^2 = \pi n_e e^2/m_e$ ,  $\Gamma$ , is the dampening rate, and  $n_e$  and  $m_e$  are electron density and mass respectively. Therefore, using equations 5 and 6, one can calculate the absorption maximum of small particles. In the case of gold, this yields a result of  $\omega_p = 8.89 \text{ eV}$  (e.g. [139]). According to the Drude analysis, there should be no size dependence on the shape of the absorption cross section for small particles, apart from an overall factor.

The bulk dielectric function is suitable for reasonably large particles, but it will eventually break down as one approaches smaller particle sizes due to quantum confinement effects [141, 142]. These produce a discrete energy level spectrum, accompanied by a discrete structure in the dielectric function. The decreasing size leads to an increasing importance of the surface, which in turn causes a dampening of the electronic oscillations with a characteristic time of the order  $\nu_F/(2R)$ ,  $\nu_F$  being the Fermi velocity [138, 143]. Physically, the damping is caused by a coupling of the collective electronic motion to single particle excitations, which are caused by the boundaries, the so called wall dissipation [144, 145]. This is related to Landau dampening in the extended solid [146]. Experiments have shown, that the bulk dielectric function is a good description for the optical properties of Au clusters down to about 10 nm. Once the size is reduced below this value, deviations are observed, which indicate a breakdown of the bulk description, as demonstrated in experiments for very small passivated nanoclusters [139].

One of the main motivations for investigating metal clusters has been the search for electron confinement due to quantum size effects. The effects should be especially significant for particle sizes that are of the same order of magnitude as the Fermi wavelength, reflecting the shape of the cluster in the electronic structure. The unusual thing about the electronic structure of small clusters (as mentioned above) is the discrete electronic structure, as opposed to the quasi-continuous bands of the bulk material. For sufficiently low temperatures  $T$ , the discrete nature of the energy spectrum will manifest itself in physical properties of the clusters. This is the case for  $kT < \Delta E$ . On average, the spacing between energy levels at the Fermi level for a box shaped simple metal particle with  $N$  conduction electrons is [137]

$$\Delta E = \frac{2}{3} \frac{E_F}{N}. \quad (7)$$

The Fermi energy is the width of the conduction band, which for a simple metal can be written as [137]

$$E_F = \hbar^2 (3\pi^2 n)^{1/3} / 2m \quad (8)$$

where  $n = 1/\Delta E$  is the density of states. Equation 7 is in need of further information about the distribution of the energy levels. There are several possible ways to approach the problem. One can use quantum chemistry to try and reconstruct the energy level spacing by precisely calculating the geometrical and electronic structure of the the system. This can be done to high accuracy by fully considering every participating atom with all their electrons, including all their possible interactions [147]. As it is highly complicated to do this, only the smallest clusters are possible to be calculated ab initio in this manner. Another approach is to characterize the electronic structure of clusters using methods similar to those commonly employed in nuclear physics. For this, the interactions of the electrons are treated statistically. Using this approach, it was possible to predict features of the energy level spectrum, which could be extrapolated towards large particles.

Different models have been developed to describe the behavior of small metal clusters. The simplest model is the Liquid Drop Model (LDM). It is a classical electrostatic model, which assumes the metal cluster to be a uniformly conducting sphere. This model has been applied successfully to derive a multitude of size dependent effects. Mie's theory [128] is based on the LDM, and the most important

information derived from this theory is the surface plasmon frequency  $\omega_s$ . According to Mie's theory, the plasmon frequency is blue shifted relative to the plasmon frequency of a bulk metal  $\omega_p$  by an amount proportional to the inverse radius of the cluster. The corresponding line width is also proportional to the inverse cluster radius and decreases for an increasing radius. For silver particles of diameter  $2 \text{ nm} < D < 10 \text{ nm}$ , for example, Mie's theory predicts the experimental energy ( $\hbar\omega_s$ ) and the line width  $\gamma$  of the surface plasmon resonance [148]:

$$\hbar\omega_s(D)/eV = 3.21 + \frac{0.58}{(D/nm)} \quad (9)$$

$$\gamma(D)/eV = 0.04 + \frac{0.59}{(D/nm)} \quad (10)$$

While the LDM describes some properties of small clusters well, it fails for others. For example, in the mid 1980s, a periodic pattern of intense peaks in the mass spectra of alkali metal clusters was discovered [149]. The nuclearities corresponding to these peaks ( $N = 2, 8, 20, 40, 58, \dots$ ) were called "magic numbers". These clusters were attributed with enhanced stability compared to their immediate neighbors. The corresponding model is called the Spherical Jellium Model. In this model, the cluster is perceived as a uniform, positively charged sphere filled with an electron gas. For this, the Schrödinger equation is solved for an electron constrained to move within the cluster sphere under the influence of an attractive mean field potential, which is due to the nuclei or ionic cores. Further information on this can be found, for example, in reference [148]. Strictly speaking, the jellium model is only valid for liquid clusters.

For crystallized clusters, there is a different model, called the Geometric Shell Structure Model. The geometric shell clusters are based on the twelve-vertex polyhedra (for example icosahedra, decahedra and cuboctahedra). They consist of  $K$  concentric shells and are characterized by the following magic numbers ( $N^*$ ), which resemble closed shells [148]:

$$N^*(K) = \frac{1}{3}(10K^3 + 15K^2 + 11K + 3). \quad (11)$$

This results in values  $N^* = 13, 55, 147, 309, 561, 923, \dots$ , but these values are closely related to the assumed geometric structure. This results in different values for different geometries [150]. The closed shell magical clusters are considered to be

thermodynamically more stable, and at least for Au<sub>55</sub> this has also been shown experimentally [151]. However, this is only valid for free clusters. Whether or not the enhanced stability is valid for clusters in a dielectric matrix is unclear at the moment.

### 2.2.1 Materials investigated within this work

The materials used in this work were gold (Au), vanadium (V), germanium (Ge), and iron (Fe). Gold was used, because Au clusters are especially of interest, as they have some intriguing applications. For example, the catalytic growth of Au nanoclusters can be exploited to create glucose biosensors [152]. It was not until fairly recently that the catalytic effects of Au nanoclusters were recognized, as the bulk material does not show potential as a catalyst, due to its weak reactivity. Since this discovery, the catalytic properties of gold nano particles have been studied intensely (for a review see references [25, 153]). It has been found that the reactivity of the gold clusters increases significantly as their size decreases below 4 nm [39]. This is why it is important to achieve small clusters with a narrow size distribution. The support of the clusters can influence reactivity considerably [25], but it is difficult to predict the role that  $C_{60}$  could play in the catalytic use of Au nanoclusters.

The second material chosen for this work is vanadium. Vanadium is one of the most abundant and widely distributed metals in the earth's crust. It can be found in 152 different minerals, in iron ores, and also in the form of organic complexes in some crude oils, for example in V-porphyrin complexes [155, 156]. It is widely used as a steel additive, as it makes steel shock- and vibration-resistant. From a

Table 3: Industrial catalytic processes using vanadium oxides [23, 24, 25, 26, 27, 28, 29, 30] (taken from [154]).

Industrial process	Catalyst material
Oxidation of $SO_2$ to $SO_3$ in the production of sulfuric acid	$V_2O_5$
Oxidation of benzene to maleic anhydride	$V_2O_5$
Oxidation of naphthalene to phthalic anhydride	$V, Mo$ oxides
Oxidation of butene to phthalic anhydride	$V, P$ oxides
Oxidation of <i>o</i> -xylene to phthalic anhydride	$V, Ti$ oxides
Selective reduction of $NO_x$ with $NH_3$	$V_2O_5/WO_3/TiO_2$

chemical point of view, Vanadium is most interesting as a catalyst. Some of the industrial processes employing vanadium oxide catalysts are summarized in table 3. These catalysts are used in the production of important chemicals like sulfuric acid or phthalic anhydride, as well as in the reduction of environmental pollution (like, for example, the reduction of nitrogen oxides from flue gas produced by power plants) [23, 24, 25, 26, 27, 28, 29, 30].

The creation of V clusters on a fullerene surface could be of interest for future applications in catalysis. So far, little is known about the interaction of vanadium with  $C_{60}$ . It has been reported, that under irradiation with a laser, vanadium destroys the fullerene cage [157]. Also, a dumbbell structure of  $V - C_{60}$  clusters has been created by laser vaporization [158]. The interaction of vanadium deposited on a fullerene surface has not been studied yet. Also, due to the clearly distinguishable core level binding energies of V in the different oxides, vanadium offers the opportunity to study the oxygen permeability of a  $C_{60}$  thin film.

The third element investigated was germanium. Bulk germanium is a group IV semiconductor, which has many useful direct and indirect band gap transitions. Germanium nanocrystals are being investigated because of their optical properties. Compared to silicon, germanium should exhibit quantum size effects for relatively large structures [40]. For a size of 75 Å, the confinement energy of germanium particles has been reported to be 0.5 eV [159]. Especially of interest is the visible photoluminescence (PL) of germanium clusters, which has been reported for clusters produced by various methods [160, 161, 162, 163, 164, 165, 166, 167]. Since cluster size plays an important role in the characteristic of the PL, it would be desirable to grow size-selected Ge clusters in a  $C_{60}$  matrix.

Finally, iron was investigated, because of the prospect of being able to grow size-selected magnetic clusters in a dielectric matrix. There are many promising applications for devices built from nanosize magnetic clusters, like magnetic random access memory, high density magnetic recording media, and magnetic sensors [168, 169, 170, 171, 172, 173]. It is important to find a fabrication method that provides good control over size selectivity, separation of the particles, and purity. All of this could possibly be provided by a fullerene matrix, a superparamagnetic mixture of iron oxide and  $C_{60}$  was created recently [174].

## 2.3 Interaction of $C_{60}$ and foreign atoms or clusters

A unique aspect of fullerene solids is, that they can be doped in many different ways. These consist of endohedral doping (where the dopant is inside the fullerene cage), substitutional doping (where the dopant is incorporated into the carbon cage), and exohedral doping (where the dopant is located inbetween several fullerene shells or simply outside the cage). These doped fullerene crystals are often referred to as fullerides. Doping can often lead to charge transfer between the dopant and the  $C_{60}$  cage. In other cases, there appears to be no charge transfer. These fullerides are called clathrate fullerene-based compounds. In the following paragraphs, a closer look at the different kinds of doping will be taken. Especially the exohedral doping is of interest, because the growth of metal clusters in a fullerene matrix in some ways resembles the creation of these fullerides.

### 2.3.1 Endohedral doping

The first doping method that shall be described here is the addition of a foreign atom or ion into the interior hollow core of the fullerene molecule. This way they form an endohedrally doped molecular unit, which is also known as either a metallofullerene or an endofullerene [175]. Many different species can be included inside the cage, and, depending on the species used, up to four metal atoms or ions have been introduced simultaneously [176]. Soon after the original discovery of the  $C_{60}$  molecule scientists were trying to incorporate different atoms or ions into its hollow interior [44, 177]. In early theoretical work on the subject, it was realized that the inclusion of La into  $C_{60}$  does not effect the electronic structure of the highest occupied molecular orbital (HOMO) level [178]. Instead, the result is a partial hybridization of the partially filled lowest unoccupied molecular orbital (LUMO) between the carbon  $2p$  and the La  $5d$  orbitals. When La is inside a fullerene molecule, it has a valence of +3, which has been shown by many different techniques [179, 180, 181]. This indicates the presence of three delocalized electrons on the  $C_{60}$  cage in anti-bonding states. If it were possible to create a solid comprised of these endohedrally doped fullerenes, these electrons would be available for conduction. Both of the iso-electronic  $Y^{3+}$  and  $Sc^{3+}$  have also been introduced into the fullerene cage [181]. All three of these species are filled-shell ions, and they have a corresponding angular



momentum of  $J = 0$ . Endohedral ions with  $J \neq 0$  could have magnetic moments.

### 2.3.2 Substitutional doping

Substitutional doping is the substitution of a carbon atom at the surface of the  $C_{60}$  cage for an impurity atom with a different valence state. This kind of doping is common for group IV solids like silicon, germanium, diamond, and graphite. Because of the small size of the carbon atom, substitutional doping is limited to very few species. Since the  $C - C$  distance in  $C_{60}$  is very close to that of graphite, it is expected that the only likely substitutional candidate is boron. Substitutional doping with nitrogen, phosphorus and aluminum may also be possible [182, 183], but no substitutional doping has been demonstrated experimentally. In the case of boron, electronic structure calculations indicate that electrons are transferred from the cage to the substitutional boron atom [184, 185]. This leaves a hole in the HOMO level of  $BC_{59}$ . It has also been demonstrated that it is possible to substitute two boron atoms on a given fullerene molecule [176].

### 2.3.3 Exohedral doping

This group of materials is of particular interest, as new solid state compounds could be made from them. The fullerenes form a sublattice while dopant atoms or molecules fill the interstitial voids in this sublattice. To determine whether or not the intercalation energy  $E_{intc} > 0$ , an empirical criterion based on electronic energy arguments has been introduced [187]. By this criterion it can be decided, whether or not a specific metal species will intercalate into crystalline  $C_{60}$ :

$$E_{intc} = E_{LUMO} - e\Phi - E_{COH} \quad (12)$$

where  $\Phi$  is the workfunction,  $E_{LUMO}$  is the energy of the lowest unoccupied molecular orbital, and  $E_{COH}$  is the cohesive energy of the metal-fullerene complex. From this equation it can be seen, that alkali and alkaline earth metals should intercalate into crystalline  $C_{60}$  [187]. As transition metals, noble metals and group III metals have high cohesive energies, their intercalation energy is negative. Gold, for example, yields a negative  $E_{intc}$ , making it an unlikely candidate for intercalation [187], but at the same time it makes gold a likely candidate for clustering.

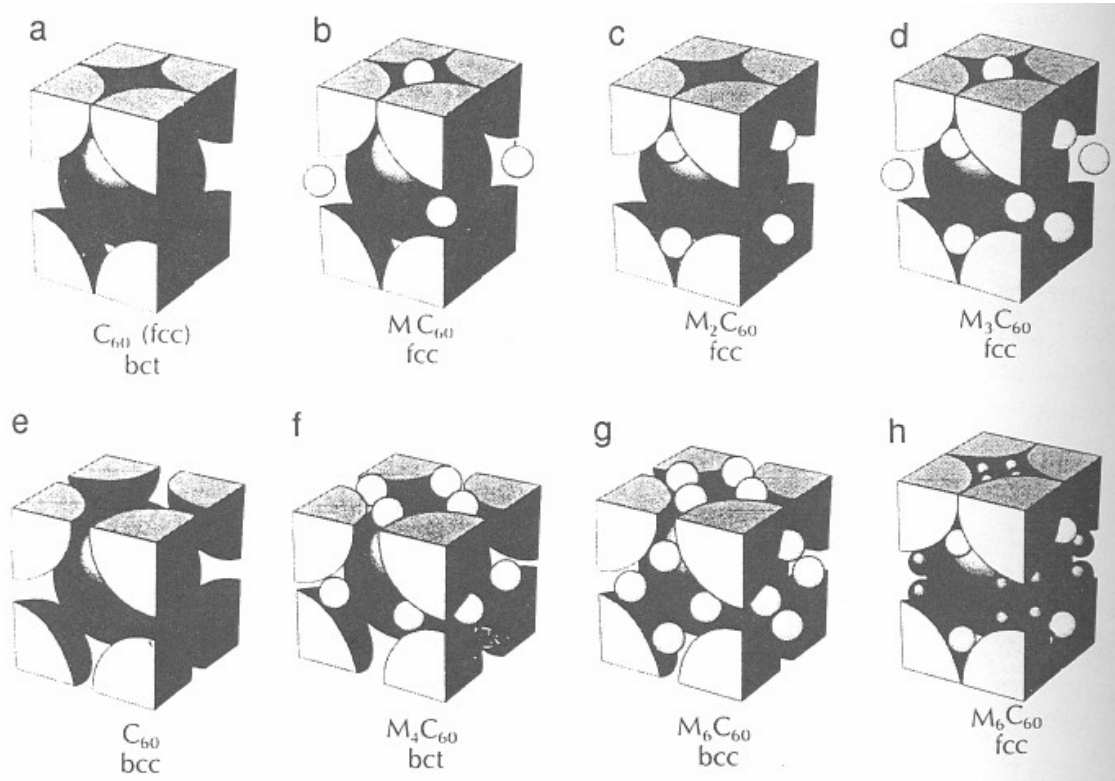


Figure 8: Crystal structures for the alkali metal fullerides (a) undoped fcc  $C_{60}$ , (b)  $MC_{60}$ , (c)  $M_2C_{60}$ , (d)  $M_3C_{60}$ , (e) undoped hypothetical bcc  $C_{60}$ , (f)  $M_4C_{60}$ , and two structures for  $M_6C_{60}$ , (g)  $M_6C_{60}$  (bcc) for  $M = K, Rb, Cs$ , and (h)  $M_6C_{60}$  (fcc), which is appropriate for  $M = Na$  [186]. The large balls denote  $C_{60}$  molecules and the small balls are alkali metal ions (taken from ref. [7]).

Most exohedrally doped fullerenes fall under the category of charge transfer compounds. These are intercalated crystals, in which the dopant (usually an alkali or alkaline earth metal  $M$ ) is introduced into the interstitial positions between adjacent molecules. Due to the size of the fullerene molecules, the cavities inbetween the molecules can be large enough to provide space for various foreign species. In these compounds, the charge is transferred from the metal  $M$  to the  $C_{60}$  molecule, leaving a positively charged metal and a negatively charged cage with mostly delocalized electrons. These exohedral doped fullerene solids are called fullerides. The guest species that has been investigated the most is the alkali metal dopant. These metals donate electrons to the fullerene sublattice. There is a wide range of

binary  $M_xC_{60}$  compounds with well-defined crystal structures for  $M = K, Rb, Cs$  [186, 188, 189, 190]. In general, values of  $0 < x \leq 6$  are possible. For the small alkali metal Na, stable compounds with  $x$  as low as 1 and as high as 11 have been reported [31]. An overview of the possible structures of  $M_xC_{60}$  compounds is shown in fig. 8. These novel materials can have intriguing and surprising new properties like the superconductivity of  $K_3C_{60}$  [32]. It has been shown that these ionic fullerides with alkalis and some earth alkalis are thermodynamically stable [33, 34]. The stability of fullerides with other elements and transition metals remains an open question, although thermodynamic considerations indicate that the large cohesive energies favor segregation and thus only a kinetically driven synthesis route is feasible. The formation of Ti, Yb, and Nb fullerides has indeed been achieved by rapid condensation of the reactants from the gas phase [35, 36, 37, 38], which suggests the possibility of creating a range of fullerides and similar materials incorporating a wider range of elements.

Finally, among the exohedrally doped fullerenes, there is the group of dopants which are only weakly bound by van der Waals force. In these so-called clathrates there is no charge transfer between the dopant and the fullerene molecule. For some molecular species like  $O_2$  and  $H_2$ , the space in the interstitial octahedral voids of pristine fcc  $C_{60}$  are large enough for them to fit into. In the case of some larger molecules, some rearrangement of the fullerene molecules in the crystal can occur. These clathrate crystals are of interest, because they could provide a growth environment for small clusters in a fullerene matrix.

## 3 Methods

### 3.1 UHV chamber and sample synthesis

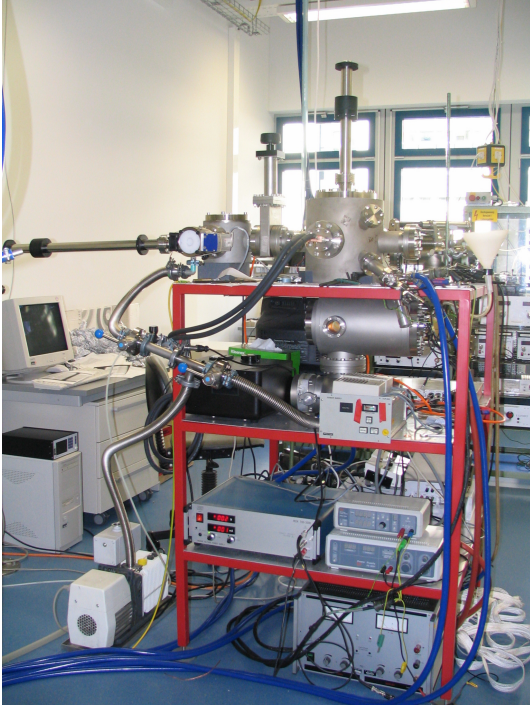


Figure 9: Picture of the UHV chamber constructed for the deposition of composite samples of  $C_{60}$  and metals or semiconductors.

In order to keep the samples as clean as possible, a ultra-high vacuum (UHV) chamber was constructed (see fig. 10). Samples are introduced into the vacuum via a lock, which provides a pressure of approximately  $1 \cdot 10^{-7}$  mbar pumped by a small turbo molecular pump. Once this pressure is reached the sample holder can be transferred through a gate valve into the UHV chamber. The UHV chamber is pumped by a turbo molecular pump and an additional titanium sublimation pump. This titanium sublimation pump is built into a cooling shroud, which can be filled with liquid nitrogen during sample deposition. This leads to a further decrease in pressure. With this combination of pumps a base pressure of approximately  $1 \cdot 10^{-10}$  mbar is readily achieved. The

sample holder can hold two substrates, one on the front and one on the back, which can be turned to face the different deposition sources.

The chamber is equipped with two different sources for depositing different materials onto the substrates. Fullerenes are deposited by an MDC Re-Vap<sup>tm</sup> 900 system. It consists of an electrical feedthrough which leads to a tungsten filament. This filament is wrapped around a quartz crucible, in which commercially available fullerene powder (MerCorp) is placed. The powder consists of 99.9% pure  $C_{60}$ . A thermocouple is inserted into the crucible through an opening to check the temperature of the evaporant.

The second deposition source is an Omicron EFM3 electron beam evaporator (EBE), which can be used to evaporate different metals and semiconductors. For

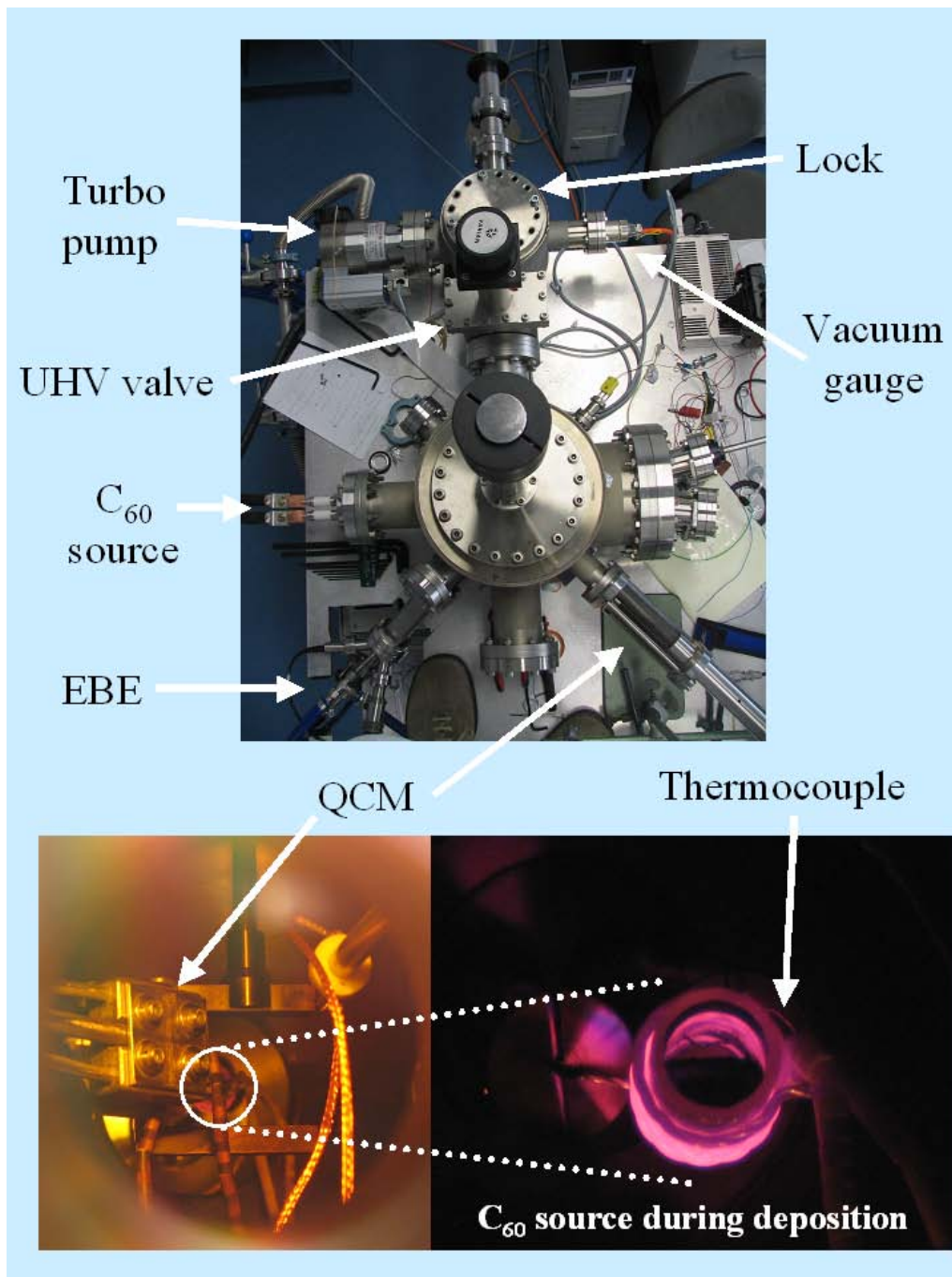


Figure 10: Top: top view of the UHV chamber. Bottom: view of the inside of the UHV chamber.

this a tungsten filament is placed in front of a metal crucible (the type of metal depends on the evaporant). Once the filament reaches a certain temperature it emits electrons. The electrons are then accelerated towards the crucible which is put on a high voltage potential. Through the electron bombardment the crucible and thereby the evaporant inside it are heated. A flux monitor provides information on the rate of evaporation. The spot size of the EBE has a radius of about 1.5 *cm* at the position of the sample holder.

The actual deposition rate at the position of the sample can be determined by using a quartz crystal monitor (qcm), which can be moved into the position of the sample holder once it is retracted. The qcm utilizes the piezoelectric sensitivity of a quartz crystal to monitor added mass. When a voltage is applied across the faces of a properly shaped piezo crystal, the crystal is distorted and changes shape in proportion to the applied voltage. At certain discrete frequencies of applied voltage a condition of very sharp electro-mechanical resonance is encountered. When mass is added to the face of a resonating quartz crystal, the frequency of these resonances is reduced. This change in frequency is very repeatable and is well understood for specific oscillating modes of quartz. In the late 1950's it was noted by Sauerbrey [191, 192] and Lostis [193] that the change of a frequency  $\Delta f = f_q - f_c$  of a quartz with uncoated and coated frequencies,  $f_q$  and  $f_c$  respectively, is related to the change in mass from the added material  $M_f$  as follows:

$$\frac{M_f}{M_q} = \frac{\Delta f}{d_f} \quad (13)$$

where  $M_q$  is the mass of the uncoated quartz crystal and  $d_f$  is the film density. Simple substitutions lead to the equation that can be used for to determine a deposition rate:

$$T_f = \frac{N_{at} \cdot d_q \cdot \Delta f}{f_q^2 \cdot d_f} \quad (14)$$

where thickness  $T_f$  is proportional to the frequency change  $\Delta f$ , and inversely proportional to the density of the film  $d_f$ .  $N_{at}$  is the frequency constant of AT cut quartz ( $= 166100 \text{ Hz} \cdot \text{cm}$ ), and  $d_q (= 2.649 \frac{\text{g}}{\text{cm}^3})$  is the density of single crystal quartz. Under the assumption of a frequency shift  $\Delta f$  of 1 *Hz* and the density for bulk material of the deposited substance a thickness change can be calculated.

To achieve composite samples simultaneous deposition with both sources is employed. The two sources are attached to the chamber at an angle of approximately  $45^\circ$  to each other, and the EBE is also mounted under an angle of  $45^\circ$  to the horizontal to prevent the liquefied evaporant from running out of the crucible. Different kinds of substrates were employed to ensure the best possible results with the different analysis methods. For photoluminescence measurements (PL, see section 3.4) silicon substrates were used as silicon should not have an indigenous luminescence that would influence the results from the fullerene or cluster luminescence. The samples deposited on silicon were also used for atomic force microscopy (AFM) measurements (see section 3.6) and Rutherford backscattering spectroscopy (RBS, see section 3.7). For the samples used in the transmission electron microscopy (TEM) analysis (see section 3.5), a copper TEM grid was fixed onto the silicon substrates in order to ensure that they are made up of exactly the same composite films as used in the PL and AFM measurements. On the other side of the sample holder, a quartz single crystal, polished on both sides, was used as a substrate. After depositing the samples on the silicon and TEM grids a sample was also deposited on these quartz substrates for investigating the optical properties of the films with ultraviolet-visible (UV-VIS) spectroscopy (see section 3.3). For this the sample holder was simply turned round without stopping the deposition, that way ensuring that the films on the quartz also have the same composition as the ones on silicon and the TEM grids.

After the deposition on both substrates the sample was taken out of the deposition site and the qcm was used to re-check the deposition rate to make sure that the composition of the samples was still as intended in the beginning of the deposition. During the deposition the flux monitor of the EBE provides a means of controlling the stability of the evaporation rate of the non-fullerene component of the film. The fullerene deposition rate is very stable and can also be controlled by monitoring the temperature within the crucible.

## 3.2 Photoelectron spectroscopy

Photoelectron spectroscopy (PES) is based on the phenomenon of photoemission, which was discovered by Hertz in 1887 [194]. In his experiment Hertz found that

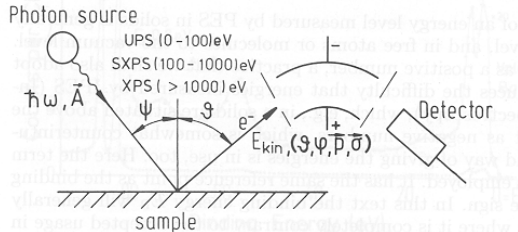


Figure 11: Sketch of a modern PES experiment. The light source is a UV discharge lamp, an X-ray tube or a storage ring. The electrons are detected by an electrostatic analyzer (taken from [195]).

the radiation from an electrical discharge arc could trigger another arc shielded by different materials. This was ultimately explained by Einstein in 1905 by introducing the quantum nature of light [196]. Basically, PES experiments are performed today much the same way as they were a hundred years ago. A typical setup for such an experiment is shown in fig. 11. The light source is usually consists of a UV discharge lamp for ultraviolet photo-

electron spectroscopy (UPS) or an X-ray tube for X-ray photoelectron spectroscopy (XPS), but other light sources like synchrotron radiation are also used. The light impinges on the sample, which can be a gas or the surface of a solid. The electrons excited by the photoelectric effect are analyzed with respect to their kinetic energy  $E_{kin}$  and their momentum  $\vec{p}$  in an electrostatic analyzer. If the energy of the incident light is known in addition to the work function  $\phi$ , then one can determine the binding energy  $E_B$  of the electrons in the sample from the following equation:

$$E_{kin} = \hbar\omega - \phi - |E_B| \quad (15)$$

The binding energy is generally referred to the Fermi level in solids, given as a positive number. The outgoing electron has a momentum  $p$  determined by its kinetic energy:

$$\begin{aligned} E_{kin} &= \frac{p^2}{2m} \\ p &= \sqrt{2mE_{kin}} \end{aligned} \quad (16)$$

In fig. 12 the schematic energy-level diagram and the energy distribution of photoelectrons as they are measured at the analyzer is shown. A solid sample has core levels and a valence band. In the presented example a metal is shown, which has its Fermi energy at the top of the valence band and is separated from the vacuum level  $E_{vac}$  by  $\phi$ . If an electron absorbs a photon in a core level with binding



energy  $E_B$  ( $E_B = 0$  at  $E_F$ ) then the photoelectrons are detected with kinetic energy  $E_{kin} = \hbar\omega - \phi - |E_B|$  in the vacuum. When one plots the energy distribution of the photoelectrons in the manner of fig. 12 then their number per energy interval often provides a replica of the electron-energy distribution in the solid and thereby of the material investigated. In actual data acquisition the reference point for molecules and atoms is taken to be  $E_{vac}$ , while in solids  $E_F$  is used as the "natural" zero. In general, however,  $E_B$  is plotted instead of the kinetic energy according to (15). This is generally done, because that way the results can be presented independent from the excitation source. Also, it allows for the results from different excitation sources to be compared directly.

The core levels are usually investigated by XPS, standard photon energy is aluminum  $K_\alpha$  (1487 eV). To prevent satellites in the recorded spectra the radiation is monochromatized before hitting the target. For the investigation of the valence band (VB) lower photon energies are preferable, because that way one can achieve higher energy and angular resolution. This can be an ultraviolet light source like a helium discharge lamp with photon energies of 21.2 eV (HeI) and 40.8 eV (HeII).

The implementation of PES depends on ultrahigh vacuum (UHV) being reached. This becomes obvious when considering fig. 13. It shows the electron mean free path  $\lambda$  in  $\text{\AA}$  as a function of the electron kinetic energy for a few selected metals [195]. From the graph it is apparent that in the region of interest, between 10 and 2000 eV, the electron mean free path is only a few tenths of a nanometer. Accordingly, investigation of the photoelectrons from a sample only probes the first few monolayers (ML) of the sample. Therefore it is imperative to work with very clean

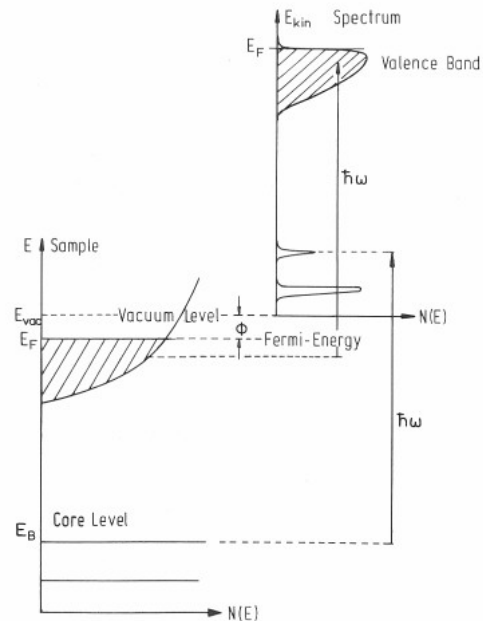


Figure 12: Relationship between the energy levels in a solid and the electron energy distribution produced by photons of energy  $\hbar\omega$ . The natural abscissa for the photoelectrons is the kinetic energy, with its zero at the vacuum level of the sample (taken from [195]).

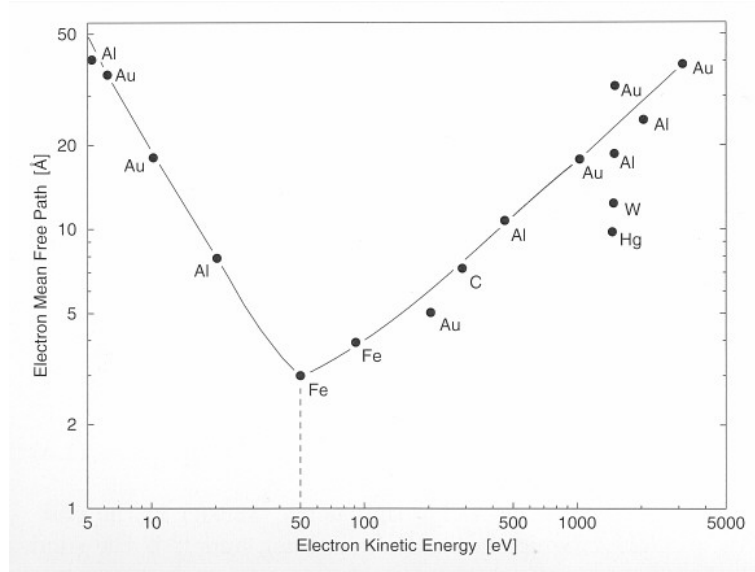


Figure 13: Electron mean free path as a function of their kinetic energy for various metals. The data indicate a universal curve with a minimum of  $2 - 5 \text{ \AA}$  for kinetic energies of  $50 - 100 \text{ eV}$ . The scatter of the data is evident from the values obtained at  $E_{kin} = 1480 \text{ eV}$  (taken from [195]).

sample surfaces, which requires UHV conditions. UHV provides a contaminant free environment, in which there is only little adsorption of oxygen or water. To give an example, if one considers a sticking coefficient of 1 (meaning every atom that reaches the surface becomes adsorbed) one reaches a coverage of one ML in less than an hour at a pressure of  $1 \cdot 10^{-9} \text{ mbar}$ . The universal mean free path depicted in fig. 13 can be used to determine whether a sample grows layer-by-layer or whether adatoms form clusters or islands. For this, the intensity of the PES substrate signal is monitored as a function of the thickness of the overlayer. The electron current  $dI$ , which stems from a sampler layer of thickness  $dz$  at a depth  $z$  detected under an angle  $\theta$  with respect to the surface normal, can be written as

$$dI \propto \exp(-z/\lambda \cos \theta) dz. \quad (17)$$

From this one can determine the overlayer ( $l$ ) signal

$$I_l = I_l^\infty [1 - \exp(-l/\lambda_l \cos \theta)] \quad (18)$$

or that of the substrate ( $s$ )

$$I_s = I_s^0 \exp(-t/\lambda_s \cos \theta). \quad (19)$$

$I_l^\infty$  is the photocurrent from the thick overlayer and  $I_s^0$  is the signal from the substrate without the overlayer. If the measured substrate core level signal intensity and the overlayer signal intensity correspond to the exponential functions, the deposited species follows a layer-by-layer growth mode. This is also known as the Lambert-Beer law.

There are two types of scattering influencing the mean free path of an electron: electron-electron and electron-phonon collisions. The latter of these only plays a role at very low energies. For the energy range of interest here, the electron-electron interaction determines the electron mean free path. The cross-section for electron-electron scattering is given by [197]:

$$\frac{d^2\sigma}{d\Omega d\omega} = \frac{\hbar^2}{(\pi e a_0)^2 q^2} \text{Im} \left\{ -\frac{1}{\epsilon(\vec{q}, \omega)} \right\} \quad (20)$$

where  $\hbar\vec{q}$  is the momentum transfer and  $\omega$  the energy transfer in the scattering process,  $a_0 = 0.0529 \text{ nm}$  is the Bohr radius, and  $\Omega$  is the solid angle into which the electrons are scattered. The inverse of the mean free path  $\lambda^{-1}$  is obtained from (20) by integration over all possible  $\hbar\vec{q}$  and  $\omega$ . Obviously  $\lambda^{-1}$  is determined mainly by the dielectric function  $\epsilon(\vec{q}, \omega)$ . As this is a material constant, the mean free path in principle represents a characteristic property of each material. For the relevant energy ranges the electrons in solids can be approximately described by a free-electron gas, as the bonding properties are no longer of great importance. The reason for this is that the binding energy of a valence electron lies in the range of  $10 \text{ eV}$ . Therefore, for  $E_{kin} \gg 10 \text{ eV}$  the electron mean free path will approximately follow a universal curve as shown in fig. 13, while for  $E_{kin} < 10 \text{ eV}$  specific material effects will be observed. In a recent experiment the mean free path of photoelectrons in  $C_{60}$  was found to be  $1.6 \text{ nm}$  (kinetic energy  $1200 \text{ eV}$ ) [198] which is commensurate with the universal curve of the mean free path given by Seah *et al.* [199]. For the case of the free-electron gas the plasma frequency is only a function of the electron density (which is equal to the mean electron-electron distance  $r_s$ ) and determines the energy loss function. In this case the inverse of the electron mean free path is

described by  $r_s$ , which is approximately the same for all materials. This leads to [197]:

$$\lambda^{-1} \simeq \sqrt{3} \frac{a_0 R}{E_{kin}} r_s^{3/2} \ln \left[ \left( \frac{4}{9\pi} \right)^{2/3} \frac{E_{kin}}{R} r_s^2 \right] \quad (21)$$

where  $R = 13.6 \text{ eV}$ , and  $r_s$  is measured in units of the Bohr radius  $a_0$ . Thus almost all materials show a similar energy dependence of the electron mean free path.

As demonstrated above, the escape depth of the photoelectrons is small and therefore PES mainly samples the near-surface region. In this way, PES can be used to quantitatively study physisorption and chemisorption. This is why this kind of analysis was named Electron Spectroscopy for Chemical Analysis (ESCA) [200]. For the analysis of the spectra, the so called "three step model" is useful. It breaks the photoexcitation up into three independent processes, which are illustrated in fig. 14. In the first step a photon enters the sample and excites an electron. The second step is the path of the electron through the sample towards the surface. In the third step the electron escapes through the surface into the vacuum where it is detected.

### 3.2.1 Theory of photoemission

In this section, the processes underlying the principles of photoemission will be explained in more detail. As mentioned above, PES is a technique in which an electron is liberated from a sample under investigation. This leads to a distinct final state, in which an electron is missing from the initial configuration or a positive charge has been added. Therefore the final state is substantially different from the initial state, and the change can be very complex for systems with many electrons. Consequentially the theory describing PES is a complex manybody theory, and there will be only a very basic description of the processes involved in PES. For a more detailed theory one can refer to the literature [201, 202, 203, 204, 205, 206, 207, 208].

Some qualitative arguments about the nature of PES spectra are easily given. For example, there will be a difference between valence band and core level spectra, as the energy of core levels does not depend on the wave vector because of its localization of the wave function. A core level spectrum will accordingly be in the simplest case a Lorentzian, and its measured width is a convolution of the core-hole state and the instrumental width. The next step is to refine the model with the

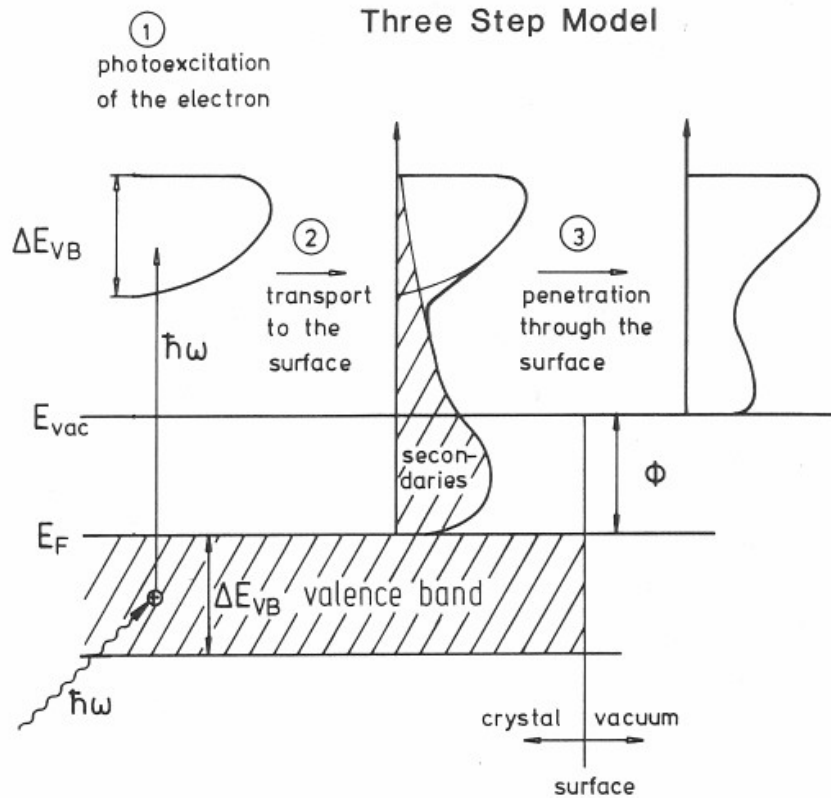


Figure 14: Sketch of the three step model: (1) photoexcitation of electrons; (2) travel to the surface with production of secondaries (shaded); (3) penetration of the surface barrier and escape into the vacuum (taken from ref. [195]).

interaction of the photoionized system with the potential created by the core hole. The charge contained in the valence band will be affected strongest by this. Under the assumption that the valence band is comprised of discrete energy levels these can be excited by the core-hole potential and appear in the core-level spectra as so called satellites at lower kinetic energies (higher binding energies).

Underlying the theory of PES there is the sudden approximation. This means that the response of the system to the creation of the photohole is assumed to be instantaneous, and that there is no interaction between the escaping photoelectron and the final state potential of the charged system (see also [207]). This model has been created for the high energy photoelectron limit. The photocurrent in PES

experiments results from photoexcitation of electrons from an initial state  $i$  with wave function  $\Psi_i$  to the final state  $f$  with wave function  $\Psi_f$  by the photon field with the vector potential  $\vec{A}$ .

Under the assumption of a small perturbation  $\Delta$  the transition probability  $w$  per unit time between the  $N$ -electron states  $\Psi_i$  (initial) and  $\Psi_f$  (final) is calculated by Fermi's Golden Rule, resulting in:

$$w \propto \frac{2\pi}{\hbar} |\langle \Psi_f | \Delta | \Psi_i \rangle|^2 \delta(E_f - E_i - \hbar\omega) \quad (22)$$

Neglecting two photon processes, this leads to

$$\Delta = \frac{e}{mc} \vec{A} \cdot \vec{p}, \quad (23)$$

where  $\vec{p}$  is the momentum operator  $\vec{p} = i\hbar\nabla$ , and  $\vec{A}$  is the vector field potential. For  $\hbar\omega = 10 \text{ eV}$  one gets  $\lambda = 10^2 \text{ nm}$  and can therefore assume that for a wide range of experiments the wavelength is large compared to the atomic distances. Based on this, one can take  $\vec{A}$  as a constant  $\vec{A}_0$ . Under consideration of the commutation relation, one can write the transition probability  $w$  (concentrating on core-level photoemission) as

$$w \propto \frac{2\pi}{\hbar} |\langle \Psi_f | \Delta | \Psi_i \rangle|^2 \delta(E_f - E_i - \hbar\omega), \quad (24)$$

if the Hamiltonian of the electron in the solid in absence of a magnetic field is

$$H = (\vec{p}^2/2m) + V(\vec{r}). \quad (25)$$

A simple approximation for a discussion of the elements of the transition matrix is a one-electron-view for the initial and final state wave function of an  $N$  electron system. This leads to an additional free electron with kinetic energy  $E_{kin}$  in the final state. The initial state wave function can be written as a product of the orbital  $\Phi_k$  from which the electron is excited and the wave function of the remaining electrons  $\Psi_{i,R}^k(N-1)$ , where  $k$  indicates that the electron with quantum number  $k$  has been left out as it was photoexcited. This leads to:

$$\Psi_i(N) = C \Phi_{i,k} \Psi_{i,R}^k(N-1) \quad (26)$$

where  $R$  stand for remaining, and  $C$  is the operator that antisymmetrizes the wave function. This can be done analogously with the wave function for the final state

effect (one just needs to replace every index  $I$  with  $f$  for final state). Together with equation (24) this gives the transition matrix elements as

$$\langle \Psi_f | \vec{r} | \Psi_i \rangle = \langle \Phi_{f,E_{kin}} | \vec{r} | \Phi_{i,k} \rangle \langle \Psi_{f,R}^k(N-1) | \Psi_{i,R}^k(N-1) \rangle. \quad (27)$$

In a first approximation one can assume that the remaining orbitals are the same as the ones in the initial state, i.e.  $\Psi_{f,R}^k(N-1) = \Psi_{i,R}^k(N-1)$ . In this case the PES experiment measures the negative Hartree-Fock orbital energy

$$E_{B,k} = -\epsilon_k, \quad (28)$$

which is also known as Koopman's binding energy.

Naturally, this is not a good approximation as the system will immediately try to re-adjust the remaining  $N-1$  electrons after ejecting the electron from orbital  $k$  to minimize its energy. This process is called relaxation. Relaxation involves the rearrangement of the remaining electrons (Auger effect, x-ray fluorescence) and the neutralization of the remaining ion by acquiring an electron from the substrate. This is usually unproblematic for bulk metals, and can be assumed to be instantaneous. For small metal clusters on semi-conducting or insulating substrates though, the relaxation of the photohole can be delayed. This final state effect is due to the small size of the system [140, 209, 210, 211], and can be seen in the core level spectra as well as in the VB spectra of small metal clusters.

The final state effects in this case dominate the peak shift of the core level, because the relaxation happens on the same timescale as the emission of the photoelectron. If the cluster is still positively charged when the electron is emitted, it has to overcome an additional electrostatic potential, which will reduce the kinetic energy of the photoelectron, and therefore the spectra are shifted to a larger binding energy. The efficiency of the electron transfer from the substrate to the cluster, as well as the actual cluster size, determine the relaxation of the photohole. The cluster acts as a spherical capacitor and the relaxation time is proportional to  $1/r$ . The peak is not only shifted by this, but it is also broadened, because both of the processes have a probability distribution in time. The problem gets more complex when the clusters in the system do not exhibit a single size but possess a size distribution with a certain width. In this case, there is an additional broadening of the peak due to the overlap of the various contributions from differently sized clusters.

The peak shift observed for gold clusters on an amorphous carbon substrate has been investigated in detail, and can reach values of up to 1 eV for the smallest cluster sizes observed ( $Au_5$ ) [210]. From this it is possible to deduce cluster size distributions in equivalent systems.

Quantum mechanically, it is necessary to sum over all possible excited states of a system to refine Koopman's assumption. If a system is strongly correlated many of the probabilities for removing an electron from an orbital ( $|c_s|^2$ ) are non-zero. In the PE spectrum, this means that one gets a *main line* as well as additional *satellite lines*. If on the other hand the correlation is weak one has only one peak. This allows the photocurrent  $I$  detected in a PE experiment to be expressed as [195]

$$I \propto \sum_{f,i,k} |\langle \Phi_{f,E_{kin}} | \vec{r} | \Phi_{i,k} \rangle|^2 \sum_s |c_s|^2 \times \delta(E_{f,E_{kin}} + E_s(N-1) - E_0(N) - \hbar\omega) \quad (29)$$

where  $E_0(N)$  is the ground state energy of the  $N$ -electron system,  $s$  is the number of states, and  $k$  the index of the orbital from which the electron was removed. Therefore, the PE spectrum consists of the lines created by the photoionization of the various orbitals  $k$ , where each line may be accompanied by satellites from the  $s$  excited state created in the final state system. This is often written as

$$A = \sum_s |c_s|^2 \quad (30)$$

where  $A$  is called the spectral function.

Core level PES of metals requires a different formulation due to its almost infinite degrees of freedom [206]. In this case one has to write [206]

$$A(E) = \sum_s |\langle i | f_s \rangle|. \quad (31)$$

Time variation of the outer electron system has to be considered, and the dynamical response of the outer electron system to the core hole is obtained as  $g(t) = \langle i | f(t) \rangle$ . The spectral function can then be calculated by a Fourier transform of  $g(t)$  [195]:

$$A(E) = \frac{1}{\pi} \text{Re} \int_0^{+\infty} dt \exp \left[ i \left( \frac{E - E_B}{\hbar} \right) t \right] g(t), \quad (32)$$

where the many-body effects are contained in  $g(t)$ , which is the dynamical response of the valence electron system to the core hole. In the case where there is no



interaction between the core hole and the valence electrons ( $H_{int} = 0$ ) one gets  $g(t) = 1$  which leads to

$$A(E) = \frac{1}{\pi} \delta(E - E_B). \quad (33)$$

If the conduction electrons screen the core hole  $g(t) = 1/t^\alpha$  and

$$A(E) = \frac{1}{(E - E_B)^{1-\alpha}} \quad (34)$$

with  $\alpha = 2 \sum_l (2l+2)(\delta_l/\pi)^2$ .  $l$  is the angular momentum of the conduction electron and  $\delta_l$  is the phase shift of the conduction electron with angular momentum  $l$ . This is an asymmetric line that diverges at the binding energy, which has its origins in the creation of the electron-hole pair.

When considering valence band photoemission, one has to consider that the electronic states have to be treated with wave vector dependency because of the delocalization of the electrons. Also, the response in this case is determined by the system from which the electron is photoexcited. This complicates the matter at hand considerably. It is why it is very difficult to extract quantitative information from UPS spectra. The complex mathematics underlying these considerations can be looked up for example in reference [195].

Information on the valence band of a system can be gained either by XPS or by UPS. XPS can be used in the valence band as well for core levels, but its resolution in this energy regime is about one order of magnitude worse than that of UPS. In solids, XPS is hardly restricted by direct transition selection rules. The relaxation of  $\vec{k}$ -conservation at high energy allows for transitions throughout the whole Brillouin zone due to the finite acceptance angle of the electrons. Therefore, with XPS one essentially measures a density of valence band states.

UPS has a large cross-section for states with low angular momentum compared to XPS. The dipole transition matrix element is proportional to the overlap integral between the initial-state wave function and the wave function of the outgoing electron. The variation of the wave function of both a low-kinetic final-state electron as well as a low-angular-momentum initial-state electron is small over the volume of the atom. This leads to a large dipole matrix element. The opposite is true for the reverse assumption of a high-energy final-state electron and high-angular-momentum initial states. Therefore, the low energy photons used in UPS

experiments yield a large photoelectron excitation cross-section in the valence band energy regime compared to XPS.

The PES measurements presented in this work have been performed at the Universität Basel, Switzerland. The fullerenes were evaporated from a simple sublimation source, that consists of a molybdenum crucible with a shutter, heated by a UHV button heater which is attached to the back of the crucible. The deposition rate of the fullerenes was between  $1.7 \text{ pm/s}$  and  $12.9 \text{ pm/s}$ . The samples were prepared in a UHV chamber with a base pressure of  $7 \cdot 10^{-10} \text{ mbar}$  which increased during deposition to  $2 \cdot 10^{-9} \text{ mbar}$ . In between deposition steps the sample was transferred in vacuo to the analysis chamber to perform photoelectron spectroscopy analysis. No residual oxygen contamination was detected in any of the experiments. Monochromatized X-ray photoelectron spectroscopy (MXPS) and ultraviolet photoelectron spectroscopy (UPS) measurements were carried out in a FISOONS ESCALAB-210 electron spectrometer equipped with a small spot X-ray source. Monochromatized Al  $K_\alpha$  radiation ( $h\nu = 1486.6 \text{ eV}$ ) was used to perform chemical analysis of the sample surface and to investigate the valence-band (VB) structure. A helium gas discharge lamp emitting light in the ultraviolet region (HeI:  $h\nu = 21.22 \text{ eV}$ ; HeII:  $h\nu = 40.82 \text{ eV}$ ) was employed for investigating the VB as well. The typical resolution is  $0.6 \text{ eV}$  for the MXPS spectra and about  $0.1 - 0.2 \text{ eV}$  for the UPS measurements respectively. The core level spectra were recorded using a constant pass energy, and for the VB spectra a constant retardation ratio was used. The spectra are presented without satellite subtraction and the energies are referenced to the Fermi level. The Fermi energy reference was a sputter-cleaned gold film, and the Fermi energy was set to  $84.0 \text{ eV}$ . No charging was observed for the fullerene layers in any of the experiments. The layers are sufficiently thin to allow for efficient charge equilibration from the substrate.

### 3.3 UV-VIS spectroscopy

Information on the optical properties of the composite samples was obtained using ultraviolet-visible (UV-VIS) spectroscopy. Fig. 15 shows a schematic picture of the Varian Cary 50 spectrometer employed for the UV-VIS measurements of this work. It is a tabletop setup, capable of carrying out measurements in a spectral range of

190 *nm* to 1100 *nm*.

The energies corresponding to the wavelengths employed by the spectrometer are sufficient to promote or excite an electron to a higher energy orbital. Fig. 16 shows a diagram of the possible electronic transitions in organic molecules with aromatic bonding. Of the six possible transitions shown in fig. 16 only the two on the left are energetically possible for the energy range available. In general, the energetically favored electron promotion is from the highest occupied molecular orbital (HOMO) to the lowest unoccupied molecular orbital (LUMO), producing an excited state. As light travels through a sample, some of the molecules or atoms along the path can absorb the photons, if they have an energy matching that of a possible transition in the molecule or atom. The two possible transitions in this energy regime are the  $n \rightarrow \pi^*$  and  $\pi \rightarrow \pi^*$  (see fig. 16). These transitions need an unsaturated group in the molecule to provide the  $p$  electrons.

Many inorganic species show charge-transfer absorption. To demonstrate charge-transfer behavior, one of its components must have electron donating properties and

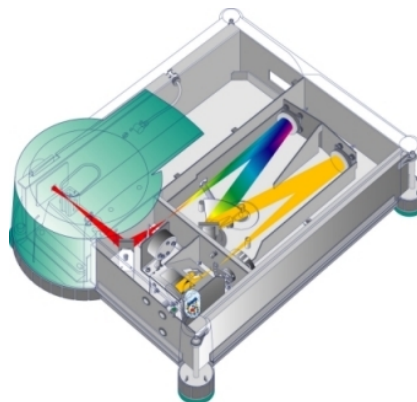


Figure 15: Schematic image of the Varian Cary 50 spectrometer used for the UV-VIS measurements (taken from [www.varianinc.com](http://www.varianinc.com)).

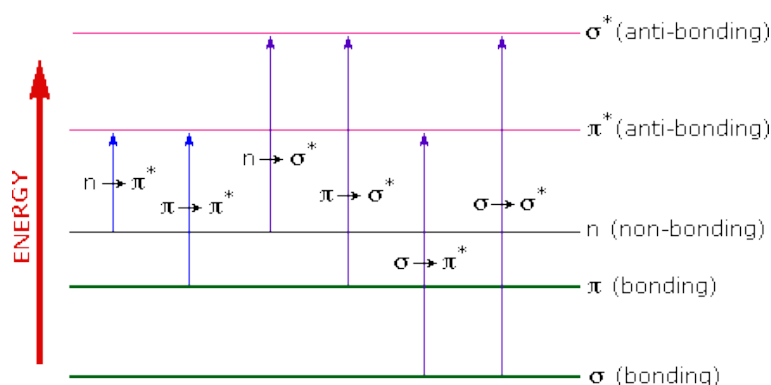


Figure 16: Diagram of possible electronic transitions in an organic molecule (taken from [www.cem.msu.edu](http://www.cem.msu.edu)).

another one must be able to accept electrons. Absorption of radiation then involves the transfer of an electron from the donor to the associated orbital of the acceptor.

### 3.4 Photoluminescence measurements

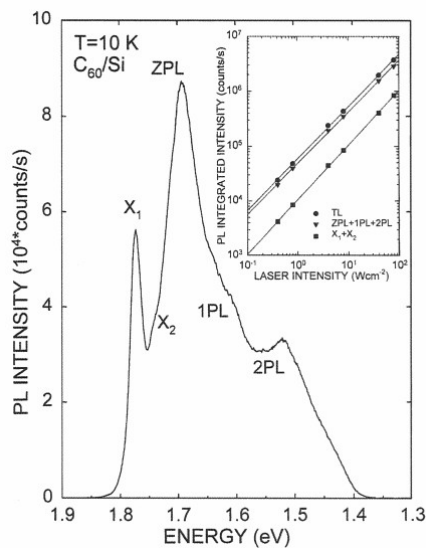


Figure 17: Photoluminescence spectrum of a polycrystalline 300 nm fullerene film (taken from ref. [212]).

Photoluminescence (PL) measurements were performed on fullerene gold composite samples in order to investigate the interaction of the Au and the surrounding  $C_{60}$  matrix. Pure fullerene films show a luminescence within the bandgap, an example of which is shown in fig. 17. Au for example, incorporated into the  $C_{60}$  layer, may have an influence on the electronic structure of the fullerene matrix, which could show up in the luminescence of the samples.

A schematic drawing of the PL setup is shown in fig. 18. Samples are mounted on the head of a helium closed-cycle refrigerator, which is located inside a vacuum chamber. The pressure during measurements is usually  $\sim 10^{-7}$  mbar. The samples are irradiated with a He-Cd laser (Topag, HCL-30 Ymc, 30 mW), which emits light at 325 nm. Before entering the chamber, the light passes through a short pass filter to suppress unwanted laser lines. After passing through the filter, the light is directed into the chamber via focusing lenses and beam directors. The luminescent light is collected by an achromatic lens pair, after which it can be passed through a long pass filter in order to filter out higher order luminescence. In the next step, the light is focused into the spectrograph, where it is dispersed. After the dispersion in the spectrograph, the light is focused onto one of two possible exit slits.

The chamber containing the sample holder is made up of non-magnetic stainless steel, and holds several sapphire windows, which allow light transmission in the range of 180 nm up to several micrometers. There are multiple flanges, which allow attachment of an electron gun, a vacuum gauge, electrical feed-throughs, and a

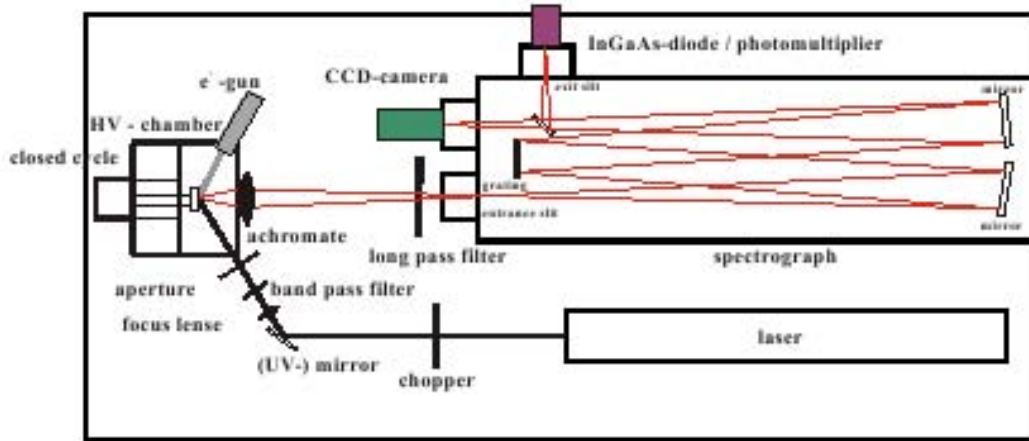


Figure 18: Schematic diagram of the luminescence setup (taken from ref. [213]).

ventilation valve. Most of the flanges are directed onto the sample position. The standard angle of incidence is  $60^\circ$ . The chamber is anodized black to avoid reflection of stray light by the chamber walls.

The sample holder is made up of oxygen-poor copper. It allows for the attachment of several samples within an area of  $1.5 \times 1.5 \text{ cm}^2$ . One of two temperature sensors (silicon diode) is also attached to the sample holder close to the mounted samples. The sample holder is mounted on the head of a CTI-Cryogenics model 22C/350C closed-cycle helium refrigerator. The refrigerator head holds a resistive heater, which is controlled by an external temperature controller (LakeShore<sup>R</sup> Model 331). It allows temperature adjustment in the range of  $10 \text{ K}$  to  $300 \text{ K}$  with an accuracy of about  $0.1 \text{ K}$ .

The spectrometer for the dispersion of the luminescent light is a single grating Czerny-Turner spectrograph (Jobin Yvon 1000M) with a focal length of  $1000 \text{ mm}$ , which is computer controlled via a serial interface. The entrance slit is manually adjustable. After passing it, the light is collected and parallelized by a toroidal mirror, before it is dispersed using exchangeable gratings. All of the spectra taken were recorded using a grating of  $600 \text{ l/nm}$  ( $700 \text{ nm}$ ). The dispersed light is then collected by a second toroidal mirror and directed to one of the exit slits. The

wavelength accuracy of the setup is established by calibrating the monochromator with a mercury lamp. Deviations between measurements of two well separated lines are found to be in the range of less than  $0.1 \text{ nm}$ .

The light is detected by a CCD camera (Yobin-Yvon Spectrum-One, liquid nitrogen cooled), which is built from a UV-enhanced silicon charged coupled device with 1024 individual pixels (EEV, model CCD20-11, back illuminated, anti-reflection coating, quantum efficiency:  $> 50 \%$  from  $220 \text{ nm}$  to  $940 \text{ nm}$ ). The CCD is located in a vacuum-sealed housing with a transparent entrance window, allowing for detection of wavelengths in the of  $200 \text{ nm}$  to more than  $1000 \text{ nm}$ .

### 3.5 Transmission electron microscopy

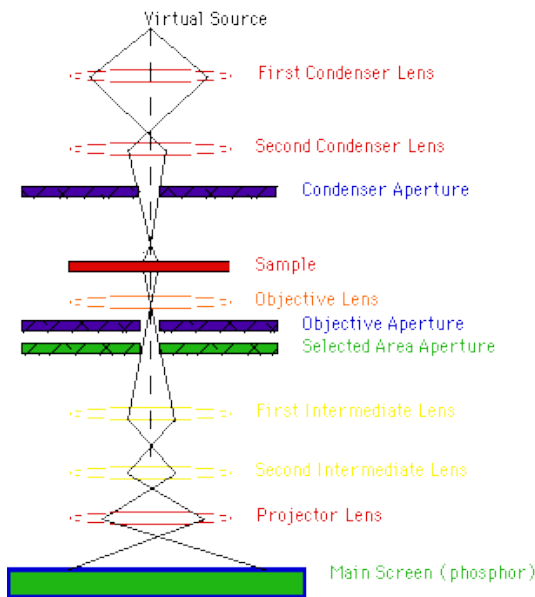


Figure 19: Diagram of a typical TEM setup (taken from [www.unl.edu](http://www.unl.edu)).

Information on the possible formation of clusters within the fullerene matrix can be gained by high-resolution transmission electron microscopy (HRTEM). The samples were deposited on commercially available TEM grids (Plano), which consist of a copper grid ( $200 \text{ mesh}$ ) that supports a  $20 \text{ nm}$  film of amorphous carbon. Onto this the samples are deposited. The microscope used for the investigation of the cluster formation and size distribution was a Philips CM 200-UT of the Institut für Halbleiterphysik at the Universität Göttingen, equipped with a field emission electron source. The

measurements were performed by Inga Hannstein.

Fig. 19 shows a typical TEM optical column. At the top of the diagram, a "virtual source" represents an electron gun, which produces a stream of monochromatic electrons. The condenser lenses 1 and 2 focus the electrons into a small, thin, and coherent beam. The general size range of the final spot that strikes the sample is determined mainly by the first lens, while the second lens actually changes the

spot size on the sample, anywhere from a wide dispersed beam to a pinpoint spot. The condenser aperture restricts the beam by knocking out high angle electrons far from the optical axis (dotted line down the center). In the next step the beam hits the sample, and parts of it are transmitted. The objective lens then focuses the transmitted portion of the beam into an image. An optional objective and a selected area metal aperture can restrict the beam further. The objective aperture enhances the contrast by blocking out high-angle diffracted electrons, while the periodic diffraction of electrons by ordered arrangements of atoms in the sample is enabled by the selected area aperture. The image is enlarged on its way down the column through the intermediate and projector lenses. In the final step, the electrons composing the image hit the phosphor image screen, generating light in the process, which in turn allows the user to see the image. The areas of the sample that fewer electrons were transmitted through appear dark. The reason for this is that these areas are either thicker or more dense, opposed to the lighter areas, which are thinner or less dense.

### 3.6 Atomic force microscopy

Information about the surface of a sample can be gained by employing atomic force microscopy (AFM). The information about the surface roughness can be used to extrapolate information on the growth mode of a given sample. A typical setup for an AFM is shown in fig. 20. The sample surface  $\textcircled{A}$  is placed under the (ideally) atomically sharp tip of a cantilever  $\textcircled{B}$ . The tip is brought into close proximity of the sample surface. The forces between the tip and the sample lead to a deflection of the cantilever according to Hooke's law, where the spring constant of the cantilever is known. Typically, the deflection is measured using a laser spot  $\textcircled{C}$  reflected from the top of the cantilever into an array of photodiodes  $\textcircled{D}$ . If the tip were kept at constant height, there would be a risk that the tip would collide with the surface, causing damage. Therefore, in most cases a feedback mechanism is employed to adjust the tip-to-sample distance. This way it is possible to keep the force between the tip and the sample constant. Generally, the sample is mounted on a piezoelectric tube. With this tube the sample can be moved in the  $z$  direction, thus maintaining

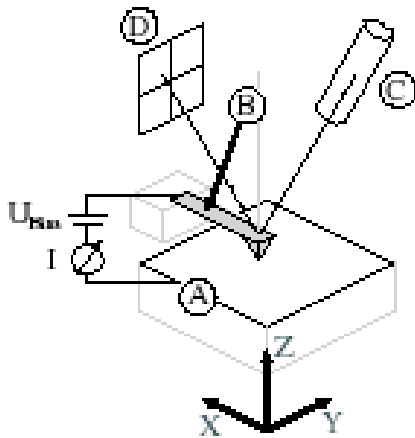


Figure 20: Schematic setup of an AFM. A laser  $\textcircled{C}$  is reflected off a cantilever  $\textcircled{B}$ , which is scanning the surface of a sample  $\textcircled{A}$ . The reflection is registered by a segmented photodiode  $\textcircled{D}$  [214].

a constant force. The  $x$  and  $y$  directions can be moved for scanning the sample. The image recorded in this way resembles the surface topography of the sample.

Many different modes of operation have been developed over the years for the AFM. The most commonly used ones are contact mode, non-contact mode, and dynamic contact mode. In contact mode operation, the force between the tip and the surface is kept constant during scanning by maintaining a constant deflection. For the non-contact mode it is possible to have the cantilever oscillating at or close to its resonance frequency by means of an external force. The tip-sample interaction force modifies the oscillation. Information on the sample characteristic

can be gained through monitoring the changes in the oscillation with respect to the external reference. The problem with this mode is that most samples develop a liquid meniscus layer. Keeping the tip close to the surface while at the same time preventing it from getting stuck in the meniscus layer is a big problem in ambient conditions. To circumvent this problem, the dynamic contact mode was developed by Zhong *et al.* [215]. In this mode, the cantilever is oscillated with so much force, that it even though it gets into direct contact with the surface on each oscillation, it gets detached from it again.

The non-contact and dynamic contact mode operation can be used for example either under frequency modulation or the more common amplitude modulation. When measuring with frequency modulation, information about a sample's characteristics is provided by monitoring changes in the oscillation frequency. Amplitude modulation, which is better known as intermittent contact or tapping mode, provides information on the sample surface topography by monitoring changes in the oscillation amplitude. It is also possible to discern between different kind of materials on the surface by analyzing the phase of the oscillations in tapping mode. All of the AFM measurements for this work were performed in tapping mode on a Dig-



ital Instruments MMAFM-2 of the Institut für Halbleiterphysik of the Universität Göttingen with Nanoprobe<sup>TM</sup> SPM tips (type: TESP). Some of the measurements were performed by Dong Du Mai and Jan Müller.

### 3.7 Rutherford backscattering

Rutherford backscattering spectroscopy (RBS) was used to determine the distribution of the various species throughout the composite sample depth for the samples deposited on Si. RBS was performed at the Göttingen heavy ion implanter IONAS [217], using 900 keV  $He^{2+}$  ions and a total charge of 9  $\mu C$ . Two Si surface barrier detectors positioned at  $165^\circ$  to the beam are used. The  $\alpha$ -particle resolution of the detector is 12.5 eV, resolving in a depth resolution of approximately 10 nm.

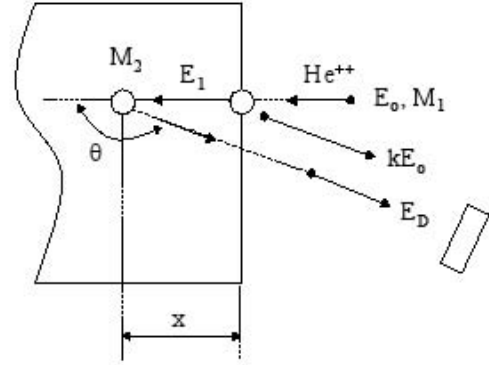


Figure 21: Schematic geometry in RBS (taken from ref. [216]).

The principle of RBS is depicted in fig. 21. It is based on the elastic scattering between an incident ion beam and the nuclei of the target. The energy of the ions  $E_0$  is typically in the range of  $E_0 = 1 - 2 MeV$ , and the ions used are usually  $\alpha$ -particles with an ion mass  $M_1$ . The scattering causes an energy loss of the ions as well as a change in direction. The energy  $E$  of the ions after a collision with a nucleus of mass  $M_2$  at the sample surface is

$$E = k(M_2, \theta)E_0 = \left( \frac{M_1 \cos \theta + \sqrt{M_2^2 - M_1^2 \sin^2 \theta}}{M_1 + M_2} \right)^2 E_0, \quad (35)$$

where  $k$  is the kinematic factor for the elastic scattering process. When the scattering takes place inside the sample, the projectile energy is changed due to dissipation. Dissipation occurs due to the interaction of the incident ions with the electrons (electronic stopping) and the nuclei (nuclear stopping) of the target. The energy that will be finally detected after scattering at a depth of  $x$  is given by

$$E_D = k \left( E_0 - \int_0^x \frac{dE}{dx} dx \right) - \int_0^{\frac{x}{\cos \theta}} \frac{dE}{d\times} dx \quad (36)$$

where  $\frac{dE}{dx}$  is the energy loss of the projectile per unit distance travelled in the target given in [ $eV/\text{\AA}$ ], which is usually called the stopping power. Stopping power tables have been collected by Ziegler *et al.* [218] for all practical purposes.

The resolution achievable in RBS is generally limited by the beam straggling, which has been formulated by Bohr [219]:

$$\Delta E_{Bohr}^2 = 4\pi Z_1^2 Z_2 N e^4 x. \quad (37)$$

$N$  is the atomic density,  $e$  is the electron charge,  $Z_1$  and  $Z_2$  are the incident and target atomic number respectively. This equation yields a good approximation of the straggling and predicts that the straggling is independent of the ion energy. All of the previous equations lead to the differential Rutherford scattering cross-section

$$\frac{d\sigma}{d\Omega} = \left( \frac{Z_1 Z_2 e^2}{4E_0} \right)^2 \frac{4}{\sin^4 \theta} \frac{\left[ \cos \theta + \sqrt{1 - (M_1/M_2)^2 \sin^2 \theta} \right]^2}{\sqrt{1 - (M_1/M_2)^2 \sin^2 \theta}} \quad (38)$$

Typically  $M_1 \ll M_2$ , which leads to the following simplification:

$$\frac{d\sigma}{d\Omega} \simeq \left( \frac{Z_1 Z_2 e^2}{4E_0} \right)^2 \frac{1}{\sin^4(\theta/2)}. \quad (39)$$

Two important things can be learned from this equation. Firstly,  $\frac{d\sigma}{d\Omega}$  is proportional to  $Z_2^2$ , which means that heavier target elements have a significantly larger scattering efficiency than lighter ones. Secondly, since the cross-section has a  $1/E_0^2$  dependence, there will be larger scattering yields at lower incident ion energies.

The element/isotope concentration profiles measured with RBS for this work were deduced using the IBA Data Furnace software [220].

## 4 2D systems

In general, there are two different ways the cluster formation in the vicinity of  $C_{60}$  can be studied. First, the interaction of foreign atoms with fullerenes can be studied by depositing them on the surface of a fullerene thin film, which is a 2D system. Second, the foreign species can be co-deposited along with the fullerenes to study the interaction in a matrix of fullerenes, which is the 3D continuation of the aforementioned approach. In this chapter, the 2D experiments are analyzed. The cluster formation on top of a  $C_{60}$  thin film has been investigated for two systems: for gold [221], and for vanadium.

### 4.1 Gold

To investigate the interaction of Au and  $C_{60}$ , three experiments were carried out. In the first experiment, a thin film of 10 *nm* gold was deposited onto highly oriented pyrolytic graphite (HOPG) after which no carbon was detectable by PES. HOPG was chosen as a substrate because of its chemical inertness with respect to Au and  $C_{60}$ . The thin Au film formed the substrate for the subsequent deposition of  $C_{60}$ . Fractions of monolayers (ML) were deposited and after each deposition step the surface was analyzed with PES. The mean diameter of the  $C_{60}$  molecule is 7.1 Å [57], the outer diameter (taking into account the  $\pi$ -electron cloud) is 1.034 *nm*. In a crystalline fullerene solid, the distance in between two  $C_{60}$  molecules is 1.002 *nm* [72], and therefore a ML of  $C_{60}$  approximately corresponds to 1 *nm*. The final nominal coverage of the  $C_{60}$  was 15 *nm*. The nominal coverage is defined as the film thickness, which is obtained if the growth proceeds via layer-by-layer growth for a given amount of material assuming a sticking coefficient of one.

In the second experiment, a thin film of (approximately 20 *nm*) of  $C_{60}$  was deposited onto HOPG, no contribution from the HOPG is detected with XPS at this film thickness. The difference in binding energy for the C1s core level is sufficient to distinguish both materials. This thin  $C_{60}$  film served as the substrate for the sequential deposition of Au. The first step consisted of 0.01 *nm* of gold, followed by several steps of 0.02 *nm*, with a final nominal thickness of 1.7 *nm*.

For the third experiment, a freshly prepared 0.2 *nm* gold film on a 20 *nm* layer of  $C_{60}$  was selected and heated to a maximum temperature of 923 *K* to investigate

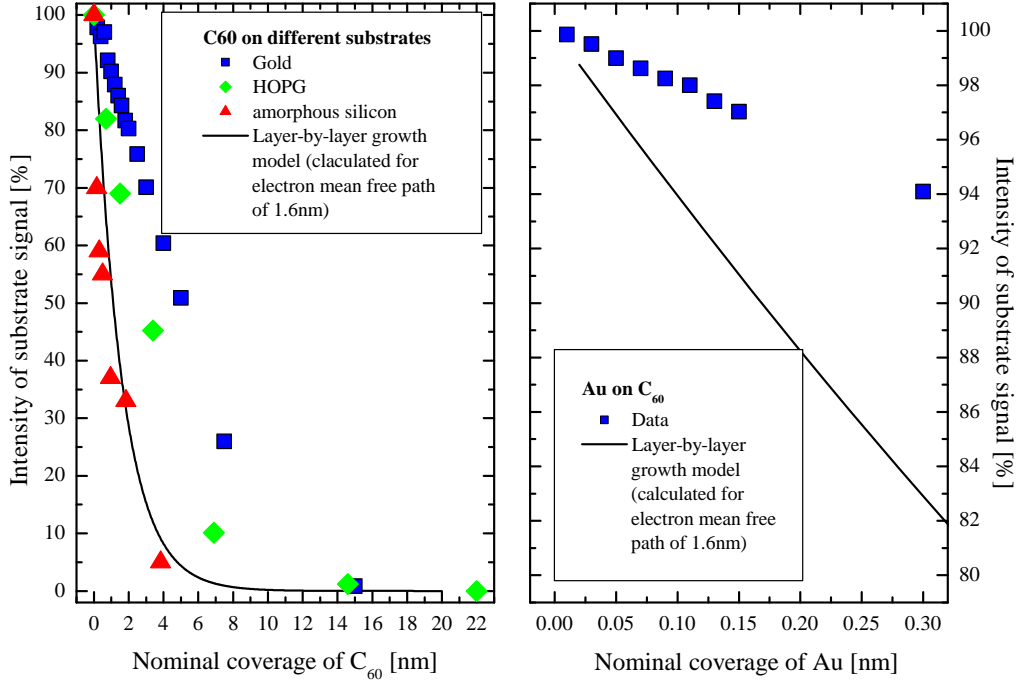


Figure 22: Left: intensity of the substrate core level as a function of the amount of  $C_{60}$  deposited on the surface. The data for HOPG and amorphous silicon have been taken from reference [222]. Right: intensity of the substrate core level as a function of the amount of Au deposited onto  $C_{60}$  [221].

the thermal stability of the film. The film was heated for ten minutes at each temperature: 573 K, 623 K, 723 K, and then in 50 K increments to 923 K. The sample was heated in situ with a UHV button heater, which is integrated into the sample holder.

Observation of the substrate signal as a function of nominal coverage allows one to deduce information on the growth mode of the overlayer [223]. The intensity of the substrate signal is shown as a function of the nominal coverage for  $C_{60}$  on Au in the left hand graph in fig. 22, for comparison the data for amorphous silicon and HOPG from [222] are included. The graph on the right hand side of fig. 22 illustrates the reduction in the substrate signal intensity for the deposition of Au

on a  $C_{60}$  surface. In a layer-by-layer growth the change in signal intensity can be described by the Lambert-Beer law, which is included in the figures as a continuous line for a sticking coefficient of one. In a recent experiment the mean free path of photoelectrons in  $C_{60}$  was found to be 1.6 nm (kinetic energy 1200 eV) which is commensurate with the universal curve of the mean free path given by Seah *et al.* [198, 199].

The experimental data for the deposition of  $C_{60}$  on gold clearly deviate from the Lambert-Beer function, indicating that  $C_{60}$  does not grow in a layer-by-layer mode, but forms islands or clusters. The island growth mode has been reported for a range of different substrate materials, such as HOPG, BN, KBr, and Au(111) [222, 224, 225], while layer-by-layer growth is less frequently reported and has been observed under well defined conditions for a-Si, NaCl, GaAs, and Mica [222, 226, 227, 228]. A strong deviation from the ideal layer-by-layer growth is also seen in the deposition of Au on the fullerene surface, which is summarized in the right hand side of fig. 22.

In fig. 23 representative carbon 1s ( $C1s$ ) core level spectra are shown as a function of nominal coverage for the deposition of  $C_{60}$  on Au and vice versa, the deposition of Au on a  $C_{60}$  surface. On the left hand side the evolution of the  $C1s$  peak during formation of the  $C_{60}$  overlayer is depicted. Prior to the first deposition of fullerenes a clean gold surface is seen in UPS and MXPS spectra (not shown here). With increasing nominal coverage of the fullerenes, the center of the  $C1s$  peak is shifted from its starting position of 284.5 eV towards higher binding energies and reaches the typical core level position (285.1 eV) of a good quality  $C_{60}$  layer for a nominal coverage of 15 nm (see bottom spectrum in the right part of fig. 23). The asymmetric peak shape and development of a shoulder, which is most clearly visible at 1.4 nm nominal coverage, indicate the presence of different bonding environments. This is supported by a fit of the  $C1s$  peak with a Doniach-Sunjic function [229, 230, 231] with two components and a Shirley background. The asymmetry of the single peaks used for this fit was negligible which is expected for an insulator such as  $C_{60}$  and the Doniach-Sunjic function becomes then equivalent to a Voigt function. The development of the binding energies of the two contributions is shown in the left part of fig. 24. The fit of the  $C1s$  peak could not be improved by increasing the number of peaks, which confirms the presence of two dominant

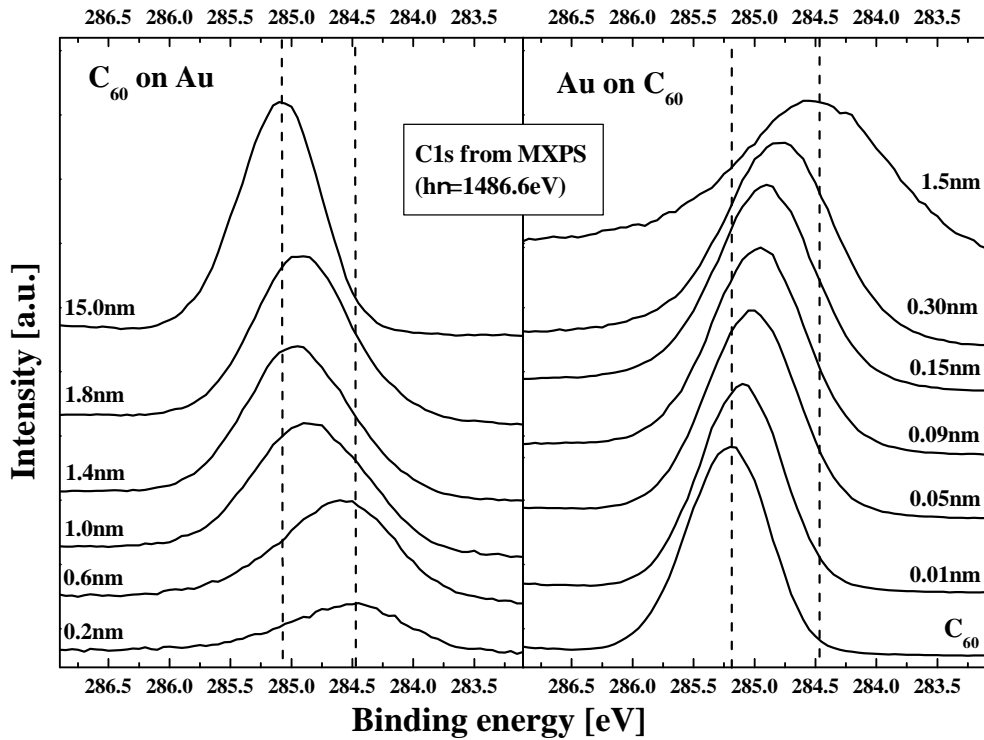


Figure 23: Left: Carbon 1s core level measured for increasing coverage of the Gold surface with  $C_{60}$ . Right: Carbon 1s core level measured for increasing coverage of the  $C_{60}$  surface with gold [221].

bonding environments. For nominal coverages of less than 0.8 nm a fit with only one peak at the low binding energy site yields better results than one with two contributions. The position of the low binding energy component is constant and the position of the high energy component is moving only slightly from 284.8 eV at the beginning of the experiment up to 285.0 eV at the end. The development of the percentages of the two components of the C1s core level is shown in the right part of fig. 24 (100% being the area for the C1s peak without fit). The intensity of the low energy component decreases rapidly with increasing nominal coverage between 0.8 nm and about 1.6 nm. For higher nominal coverages the contribution

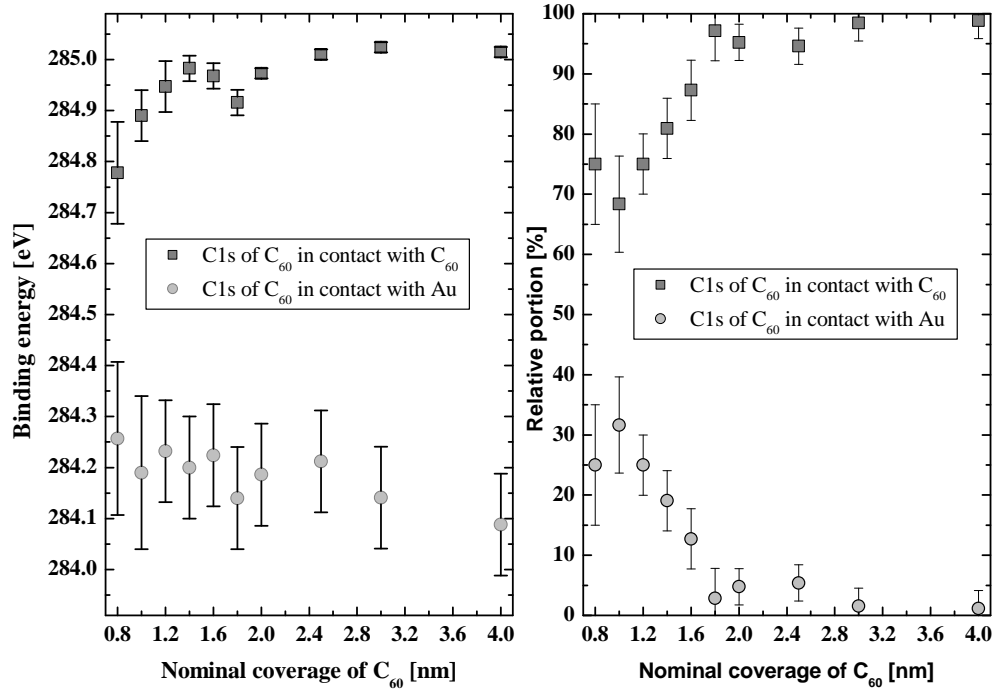


Figure 24: Left: position of the two components of the C1s determined by a fit with a Doniach-Sunjic function for increasing nominal coverage of  $C_{60}$  on gold. Right: Development of the percentages of the two separate components of the C1s core level for increasing nominal coverage [221].

of the low energy component to the peak becomes small. This indicates that the lower binding energy contribution is from  $C_{60}$  in contact with the gold substrate which leads to a chemical shift of the fullerene signal compared to a fullerene solid. For increasing nominal coverage the relative amount of  $C_{60}$  molecules which are in contact with Au decreases and the contribution from fullerenes with fullerenes as next neighbors will increase. The peak located at higher binding energy can now be attributed to these fullerenes and it consequently dominates the spectra at higher nominal coverages. The contribution at low binding energies ( $C_{60}$  - Au) is weak but can still be identified at relatively high coverages of 4.0 nm due to the island growth, which enables one to detect interface molecules even at such high nominal

coverages.

The right hand side of fig. 23 shows the evolution of the C1s peak for the deposition of gold onto a clean fullerene surface. The position of the C1s peak for the  $C_{60}$  surface is at 285.2 eV and a continuous shift of the peak to lower binding energies is observed as gold accumulates on the surface. For the largest observed nominal coverage of 1.5 nm the peak is positioned at 284.45 eV, which is equivalent to  $C_{60}$  molecules in contact with a gold surface (see left part of fig. 23). The Gaussian fwhm of the peak increases slightly and the other fit parameters (asymmetry, Lorentzian fwhm) are constant. In contrast to the deposition of  $C_{60}$  on the gold surface, a fit using two components does not yield satisfactory results and the agreement of fit and experimental curve remains poor. We attribute this failure to fit the C1s peak to the presence of a multitude of bonding environments which the Au atoms adopt on the  $C_{60}$  surface and which lead to small relative differences in binding energy of the carbon atoms. The contribution from  $C_{60}$  molecules which are not positioned at the surface dominates in the beginning of the experiment, while those located at the interface to the Au overlayer dominate the spectra after the last deposition step.

So far we only have discussed the evolution of the C1s core level. Now we will focus on the Au4f<sub>7/2</sub> core level, which can provide information on the size and size evolution of the clusters forming in the deposition of gold onto the fullerene substrate. The top part of fig. 25 shows the development of the Au4f<sub>7/2</sub> binding energy as a function of the nominal gold coverage. In the early stages of the deposition the Au4f core level is positioned at 84.38 eV, and is then shifted with increasing nominal gold coverage to lower binding energies. The bulk value of 84.0 eV is reached for a nominal coverage of 1.7 nm (not shown in the figure). The peak asymmetry and the Lorentzian fwhm are constant within the error of the fit, but the Gaussian fwhm changes with increasing nominal coverage. For the smallest coverage it has a value of 1.10(5) eV which continually decreases to 0.90(5) eV for a nominal coverage of 0.15nm. The Gaussian fwhm is primarily connected to the cluster size distribution, which influence the shift of the core level binding energy. The small size of the system has a strong influence on the photoelectron binding energy of small clusters [209, 210, 140, 211, 232]. For metal clusters on insulating or semiconducting surfaces the final state effects dominate the peak shift. The shift of the core levels



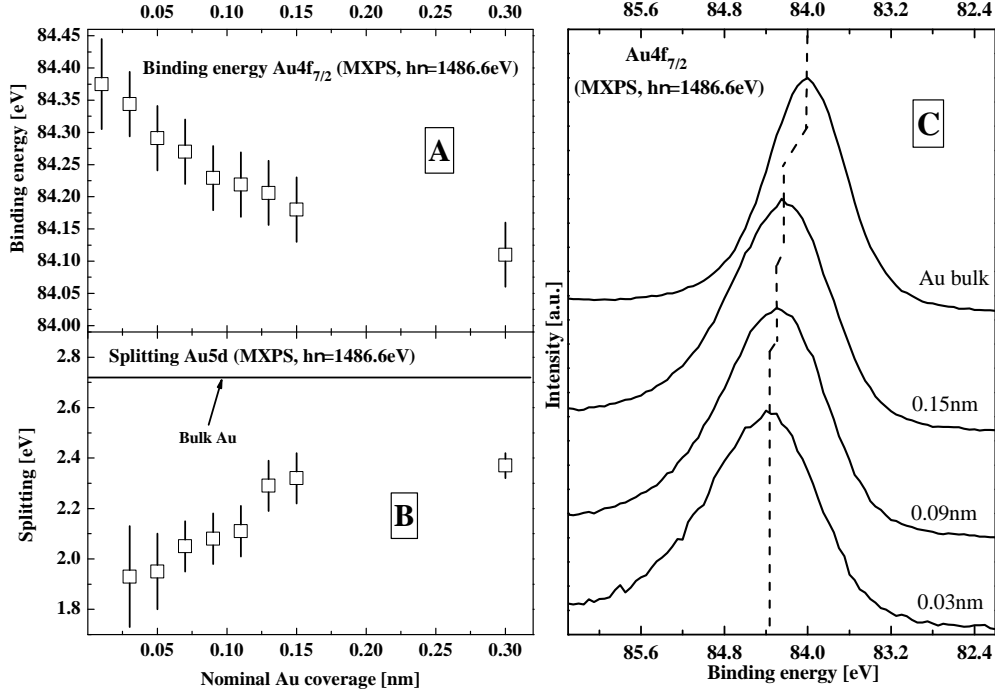


Figure 25: A: Binding energy of gold  $4f_{7/2}$  core level for the deposition of gold onto  $C_{60}$ . The binding energy reaches bulk values for a deposited amount equal to 1.7 nm. B: splitting of the two main components of the Au5d band as a function of the nominal gold coverage. C: Representative core level spectra of  $Au4f_{7/2}$  [221].

is due to poor screening of the photo-hole in small clusters, because the relaxation of the photo-hole is delayed compared to the timescale of the photoelectron emission. This leads to the clusters still being positively charged as the photoelectron is emitted. This additional electrostatic barrier reduces the kinetic energy of the photoelectron and leads to an increase in the apparent binding energy. The cluster can be viewed as a spherical capacitor and the relaxation time of the photo-hole is inversely proportional to the radius of the cluster. It is also influenced by the efficiency of the electron transfer from the substrate to the metal clusters. A peak shift is observed for clusters smaller than about 2 nm and can amount to 1 eV for very small Au clusters ( $Au_5$ ) [210].

A reliable fit of the Au4f core levels has been elusive for this system as the peak shape is severely changed by the size distribution of the clusters and the timescale of the photo-hole relaxation [211]. It is not possible to identify clearly distinguishable bonding sites as was the case for the C1s ( $C_{60}$  on Au) or for Si on a  $C_{60}$  surface [12]. In the case of Si on  $C_{60}$  the Si2p core level could be described by two components assigned to different bonding environments. The relatively large chemical shifts involved enabled us to perform a fit despite the convolution of chemical shift and final state effects. The inability to distinguish between distinct bonding sites in the Au4f core levels appears to support a model with a continuous cluster growth and the absence of preferred binding or nucleation sites for small clusters, a multitude of different bonding sites is present and thus many overlapping peaks prevent a unique assignment. A high resolution photoemission experiment could in the future help to address and answer this question. The information on the size of the gold clusters can be extracted from the core level and VB spectra and will be discussed in the next paragraph.

The cluster size is responsible for the shift of the Au4f core levels (final state effect) and it also determines the splitting of the two main components of the Au5d band [209, 233] through size dependent changes in the electronic structure, an initial state effect. This is shown in part B of fig. 25. Fig. 26 shows the binding energy shift of the Au4<sub>7/2</sub> core level as a function of the splitting energy of the two main components of the Au5d band. The plot clearly shows a linear relation between the core level shift and the splitting energy. The gradient of  $-0.39(4)$  eV is in good agreement with values derived from the pictures in reference [210], which show a slope of  $-1/3$ . The splitting was obtained from MXPS-VB spectra (normalized to unit height, spectra not shown here) by subtracting a normalized spectrum of pure  $C_{60}$  after shifting it lower binding energy. The amount of the shift was determined by comparing the position of  $C_{60}$  related features (at 10.8 eV) with those in the  $C_{60}$  prior to deposition. All features are shifted rigidly to lower binding energies, an effect which is also described in the discussion of the C1s core level spectra. According to DiCenzo *et al.* the splitting energy of the Au5d band is directly correlated to the mean coordination number of the gold atoms [233]. The d-band splitting increases with nominal Au-coverage and reaches 2.75 eV at a nominal coverage of 1.7 nm, which is equivalent to the splitting in the d-band of a gold

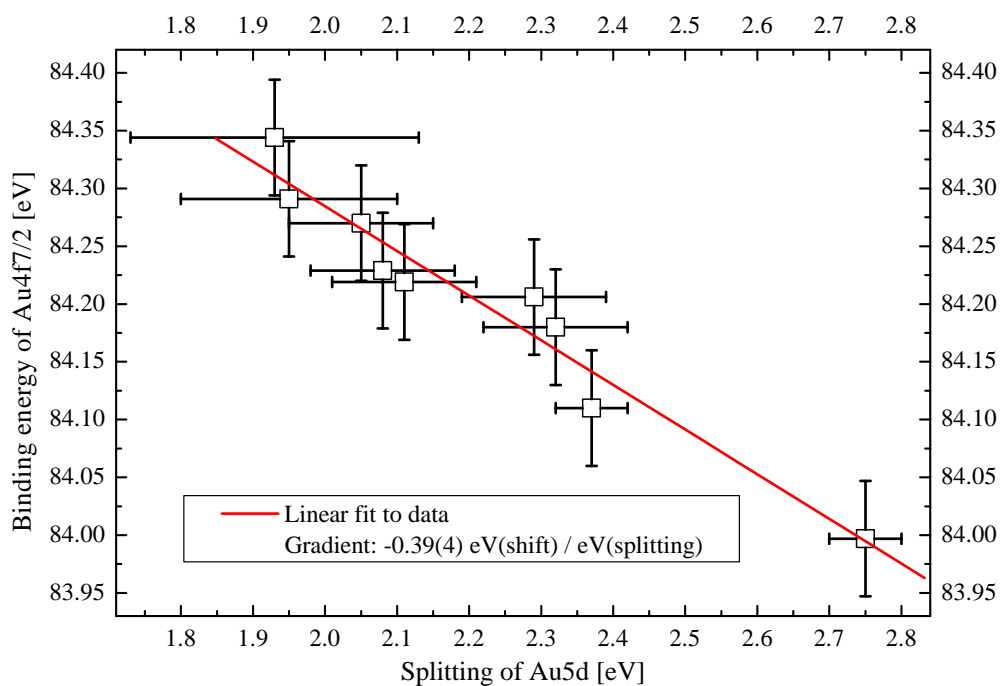


Figure 26: Plot of the binding energy of the  $\text{Au}4f_{7/2}$  core level as a function of the splitting energy of the two main components of the  $\text{Au}5d$  band.

bulk material. From this, one can deduce the cluster size of the gold clusters, which in our case is between about 55 atoms for the smallest splitting value [2] and about 150 atoms for the largest splitting observed, which is equivalent to bulk gold. The relatively large size of the smallest clusters, which are obtained for very low coverages, also indicates that preferred adsorption sites defined by the fullerene lattice are absent. Adsorption in the lattice troughs for example would lead to the formation of numerous small clusters rather than the formation of larger clusters as we observe here. For example, a nominal coverage of  $0.01 \text{ nm}$  corresponds to approximately one gold atom for each trough in the fullerene surface. Comparing the information from the initial and final state effects (d-band splitting and core level shift) on clusters size agree well. The shift of the core level is in good agreement

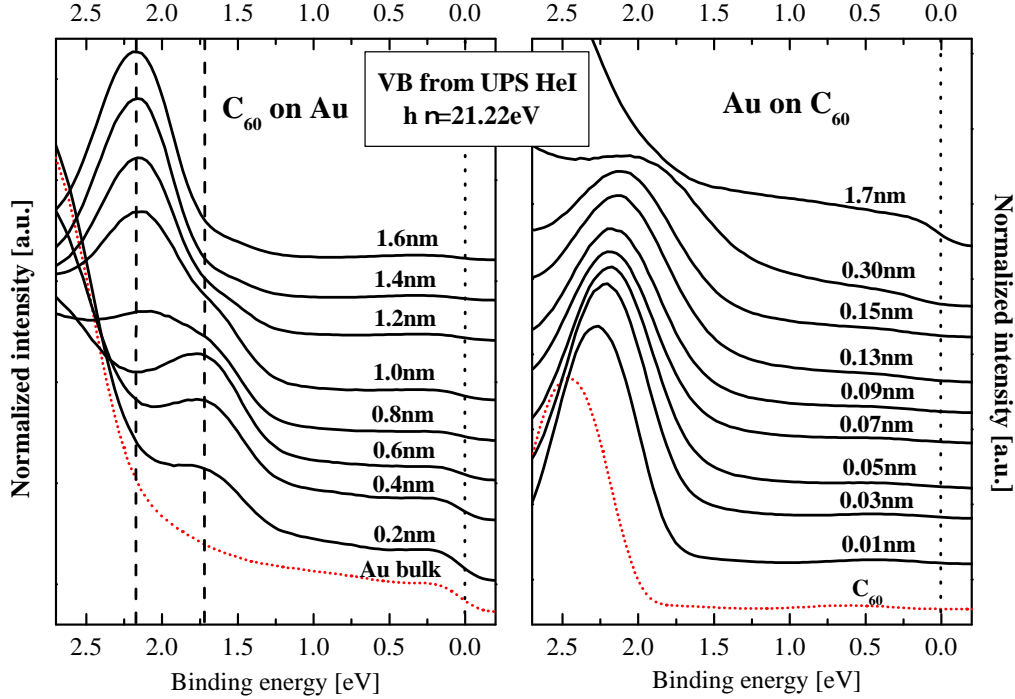


Figure 27: Left: evolution of the VB for increasing nominal coverage of  $C_{60}$  on a gold substrate. Right: evolution of the VB for increasing nominal coverage of Au on a fullerene substrate [221].

with results from Au clusters on a vitreous carbon substrate [209] as well as with results for metal clusters on amorphous carbon [210]. This shows that the charge transfer from the fullerene substrate to the Au clusters is comparable to that of amorphous carbon substrates to Au and other metal clusters.

The fullerene peaks in the UPS-VB spectra are shifted towards the Fermi energy in the same way as the  $C1s$  core level is shifted towards lower binding energies. An overview of some of the spectra for both experiments is given in fig. 27. In the left part, the evolution of the highest occupied molecular orbital (HOMO) peak during the deposition of  $C_{60}$  onto the gold substrate is shown. For the first deposition step the HOMO peak is positioned at approximately  $1.7\text{ eV}$ . The intensity of the  $C_{60}$

related features increases with the nominal coverage and an additional peak arises at 2.2 eV at a coverage of 0.8 nm. This second peak increases in intensity with a further increase in coverage while the contribution from the low binding energy peak cannot be detected anymore at the coverage of 1.6 nm. The low binding energy component appears to be the HOMO peak of  $C_{60}$  in contact with the gold substrate, and the high binding energy component stems from  $C_{60}$  in contact only with other  $C_{60}$  molecules. A closer look at the spectra reveals that the entire fullerene spectrum is duplicated for small nominal coverages, but it is best seen in the HOMO peak because the influence of the gold substrate in this area of the VB spectra is minimal (the first strong feature of the gold VB is the low binding energy component of the Au5d band). Each further  $C_{60}$  deposition step after a nominal coverage of 0.8 nm leads to a decrease in the HOMO peak contribution from the molecules in contact with the gold substrate. At the same time the intensity of the Fermi edge from the Au substrate decreases due to the increasing fullerene coverage. In the spectra for more than 1.6 nm nominal coverage the HOMO peak from the fullerenes that are only in contact with other fullerenes dominates, but all fullerene related peaks continue to shift towards higher binding energies until the last deposition step, indicating that there still is a small influence from the substrate even for a nominal coverage of more than 7.5 nm, which is an indication of band bending in the insulating fullerene overlayer. This is also in agreement with the C1s core level spectra, where a slight shift to lower binding energies is still detectable for these coverages. It should also be noted that there is no distinguishable peak near  $E_F$ , which is expected for a filling of the lowest unoccupied molecular orbital (LUMO) through charge transfer from the gold substrate to the fullerene molecules [234, 235].

The right part of fig. 27 shows the evolution of the  $C_{60}$  HOMO for an increasing nominal coverage of gold deposited on a fullerene substrate. With increasing nominal coverage the HOMO peak shifts towards the Fermi energy. In this case there is no visible component of the HOMO peak from the fullerenes in contact with the gold atoms on the surface, which is commensurate with the findings from the C1s spectra. It has to be noted that single Au and small clusters will behave differently than bulk Au due to the considerable differences in the electronic structure which drive the chemisorption and charge transfer at interfaces. However, in both cases

we see that the peak from the  $C_{60}$  HOMO is shifted, but there is no apparent filling of the LUMO. This provides further information on the electronic properties of the  $Au - C_{60}$  interface. Since all  $C_{60}$  related peaks in the UPS VB spectra are shifted towards the Fermi energy (as are the  $C1s$  core levels), this indicates a band bending in addition to the chemisorption of the first layer.

To investigate the thermal stability of the gold clusters, a film of  $C_{60}$  with a nominal Au coverage of  $0.2 \text{ nm}$  was deposited and annealed *in situ*. For this coverage, the binding energy position of the  $Au4f_{7/2}$  core level is  $84.07 \text{ nm}$ , which is in the expected range from the sequential deposition experiment (see fig. 25). In part A of fig. 28, the gold concentration is plotted as a function of the annealing temperature. The concentration is constant until a temperature of  $350^\circ C$  is reached. No change in the Au concentration is observed, albeit the change in peak shape (Gaussian fwhm and d-band splitting) indicates a modification in cluster size. The binding energy is already at the bulk position and in this range of cluster sizes not sensitive to cluster size changes any more. For annealing temperatures exceeding  $350^\circ C$ , the gold concentration slowly drops to about half of its starting value, indicating either a diffusion of gold, possibly even of whole clusters, into the sample or the evaporation of Au from the small clusters. In case of the evaporation we would expect to observe a decrease in cluster size, which could be detected in the splitting of the  $Au5d$  band but is not observed (part C of fig. 28). The increasing splitting indicates a ripening of the clusters. The first annealing step of  $200^\circ C$  increases the value from  $2.14(5) \text{ eV}$  to  $2.28(5) \text{ eV}$  which is in the range of the expected value of about  $2.3 \text{ eV}$  for sequential deposition. The splitting continues to increase up to an annealing temperature of  $450^\circ C$ , when a splitting of  $2.66(5) \text{ eV}$  is reached which corresponds to the value of bulk gold. Annealing at higher temperatures does therefore not lead to further changes of the splitting, it remains constant and cluster size changes cannot be monitored in this fashion anymore. Further indication for ripening of the clusters is given by the fwhm of the  $Au4f_{7/2}$  core level is shown in part B of fig. 28. It decreases significantly for the first annealing step of  $350^\circ C$ , after which there are only minor changes, commensurate with a ripening of the clusters and approach of Au bulk properties for larger cluster sizes. For annealing at higher temperatures, the fwhm remains constant within the error of the measurement. It is remarkable that the sublimation of the fullerene layer is suppressed through the presence of the

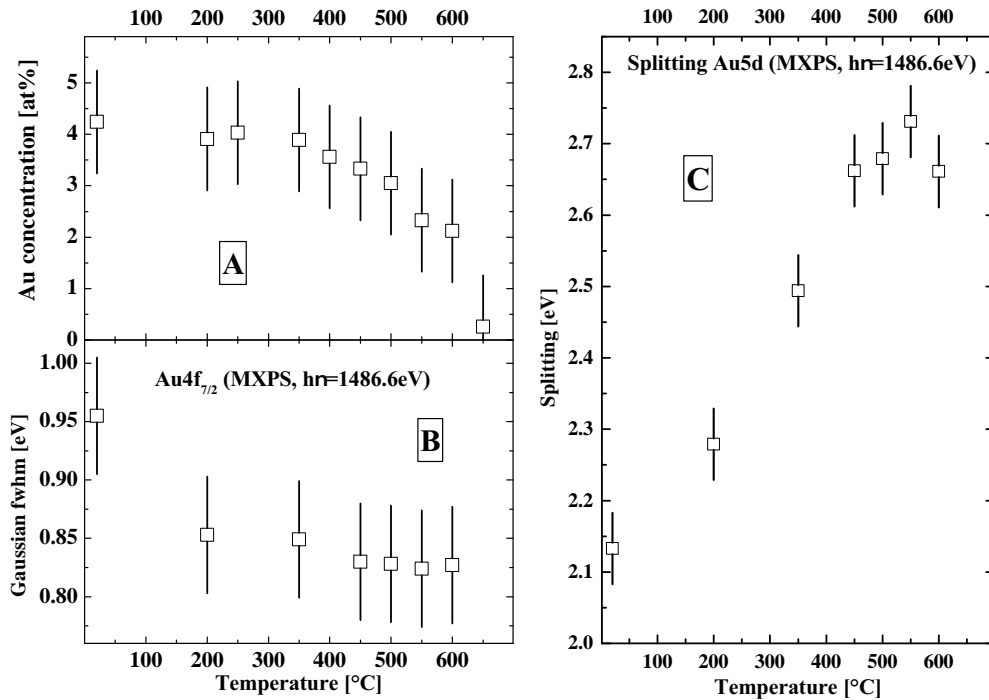


Figure 28: A: Au concentration as a function of the annealing temperature. Up to a temperature of  $350^{\circ}\text{C}$  the concentration is stable, higher annealing temperatures lead to slow decrease in gold concentration. B: Gaussian fwhm of the  $\text{Au}4f_{7/2}$  peak as a function of the annealing temperature. For the first annealing step the fwhm significantly drops. C: Splitting of the two main components of the  $\text{Au}5d$  band as a function of annealing temperature. The splitting increases up to an annealing temperature of  $450^{\circ}\text{C}$  when the value of bulk Au is reached. For an annealing temperature of  $650^{\circ}\text{C}$  the Au concentration is too small to ascertain a Gaussian fwhm of the  $\text{Au}4f$  core levels or a splitting of the  $\text{Au}5d$  band [221].

Au clusters at the surface, which offers a way to stabilize fullerene layers while at the same time preserving their bulk properties.

Several possible processes are in agreement with the XPS results: (i) the Au clusters grow with increasing temperature as is apparent from the d-band splitting, (ii) Au atoms or whole clusters diffuse into the fullerene film, leaving the detection range of XPS, and (iii) a rearrangement of fullerene molecules around the Au clusters

could lead to the formation of a  $C_{60}$  overlayer. This type of rearrangement has been observed in the interaction of  $C_{60}$  with selected Au surfaces [236] and is a process which will be explored in more detail in future experiments. The cluster growth apparently begins prior to the loss of Au atoms/clusters into the bulk of the film and can be attributed to the ease of surface diffusion as compared to bulk diffusion.

#### 4.1.1 Conclusions

The formation of clusters or islands is observed in the deposition of  $C_{60}$  on a gold substrate and in the deposition of Au on  $C_{60}$ . For the deposition of  $C_{60}$  on gold, the C1s core level and the UPS-VB spectra allow to distinguish between fullerene molecules that are in contact with the gold substrate and those from the second layer that are only in contact with other fullerene molecules. A chemisorption of the fullerene molecules on Au leads to this change in the fullerene related features for the first adsorbed layer. This distinction cannot be made in the formation of Au clusters on the highly corrugated  $C_{60}$  surface, and it is not possible to unambiguously identify specific bonding sites of the Au atoms or clusters. The smallest clusters created in this experiment consist of approximately 50 Au atoms for very small coverages and a continuous increase in cluster size is observed as the experiment progresses. The analysis of the core level and valence band spectra as well as the actual cluster size indicate that the cluster formation and growth are not controlled by the  $C_{60}$  surface topography. Unlike silicon on  $C_{60}$ , gold does not appear to nucleate at specific bonding sites [12]. The results from these experiments demonstrate that gold forms clusters on a fullerene surface and first experiments show that this can be expanded into composite films made up of Au clusters and  $C_{60}$  5.1.

In both cases (Au on  $C_{60}$  and vice versa) the C1s core level shows two identical extreme positions, which are assigned to  $C_{60}$  in contact with Au for the low energy site and by  $C_{60}$  only in contact with other  $C_{60}$  for the high energy site. The shift is partially due to chemisorption of the first layer in case of  $C_{60}$  on Au, as the shift is most prominent for the deposition of the first ML. Both the core level spectra and the VB spectra exhibit an additional small shift to higher binding energy which can be attributed to a band bending in the fullerene film. The bonding at the interface can be described as chemisorption but lacks the the signature of



a charge transfer and filling of the  $C_{60}$  LUMO. Since there is no charge transfer, the bonding is not ionic. Most likely, the interaction between the Au and the fullerene molecules is a covalent bonding of the fullerene  $\pi$  system with the surface of the Au. Au clusters on a  $C_{60}$  film surface exhibit a good thermal stability: the fullerene sublimation is suppressed and the Au clusters increase in size driven by the fullerene surface diffusion. If the temperature is increased above  $500^\circ C$  a drop in the Au concentration is observed and marks the onset of Au-diffusion into the fullerene film.

## 4.2 Vanadium

Vanadium was chosen as another 2D system because of its high reactivity and its usefulness as a catalyst. Some of the reactions that vanadium oxides are used to catalyze are shown in table 3 in chapter 2.2. A fullerene film closely packed with vanadium oxide clusters could be of interest for catalytic applications. Since specific stoichiometries are difficult to deposit, it would be useful to be able to deposit vanadium into the fullerene film and oxidize it afterwards. The permeability of  $C_{60}$  films is uncertain, which is why an experiment was designed to investigate this aspect. The different experiments carried out for this system are summarized in table 4. As with Au, the first step was to deposit sub-monolayer amounts of vanadium onto a fullerene substrate. Due to its high reactivity, this layer already contains up to 40 % of oxygen (compared to the vanadium content). The reactivity of the vanadium is an important factor in the experiment. This is why the reactivity as well as the thermal stability has been investigated. A layer of oxygen poor vanadium is buried under a few monolayers of  $C_{60}$  and then exposed to molecular oxygen. The different valences of the vanadium bound in different vanadium oxides show very distinct core level binding energies of the  $V2p$  core levels, which allows the oxidation of the vanadium to be monitored. To investigate the thermal stability of the films, the samples were annealed in situ and measured with PES while they were kept at the elevated temperature. First, UPS spectra were taken before measuring MXPS for about an hour. After measuring MXPS, another UPS spectrum was measured, which was identical to that from the beginning of the annealing step.

A series of experiments was carried out and the sequence of treatments in each

Step	V @ $C_{60}$	V @ HOPG	Oxidation <i>ex situ</i>	Oxidation <i>in situ</i>
1	20 ML $C_{60}$	5 nm V	20 ML $C_{60}$	20 ML $C_{60}$
2	0.05 ML V	15 nm V	1 ML V	1 ML V
3	0.1 ML V	annealing @ 800 °C	after 2 days in air	3 ML $C_{60}$
4	0.3 ML V		annealing @ 320 °C	after 5' @ $10^{-2}$ mbar $O_2$
5	0.5 ML V		annealing @ 510 °C	after 10' @ $10^{-2}$ mbar $O_2$
6	1.0 ML V		annealing @ 700 °C	annealing @ 300 °C
7	1.5 ML V			annealing @ 500 °C
8	2.0 ML V			annealing @ 700 °C
9	2.5 ML V			
10	annealing @ 314 °C			
11	annealing @ 395 °C			
12	annealing @ 565 °C			
13	annealing @ 735 °C			

Table 4: Overview of the steps carried out in the different vanadium experiments. Annealing was carried out *in situ* under UHV conditions. Each entry describes the situation during the PES measurement.

experiment is summarized in table 4. In the first experiment (column "V @  $C_{60}$ " of table 4), a film of  $C_{60}$  was deposited onto HOPG. PES showed the film to be a pure fullerene film without measurable contaminants. Fractions of monolayers (ML) of vanadium were deposited onto the fullerene film, and after each deposition step the surface was analyzed with PES. The nominal coverage is defined as the film thickness, which is obtained if the growth proceeds via layer-by-layer growth for a given amount of material assuming a sticking coefficient of one.

The second experiment was the deposition of V on HOPG (column "V @ HOPG" of table 4). This allows the interaction of V and  $C_{60}$  to be compared to that with a different carbon allotrope, which provides a flat surface of likewise  $\pi$ -bound carbon atoms. A thick V film was deposited and then annealed in a single step at 800 °C.

In the third experiment, a monolayer of vanadium was deposited on a fullerene thin film and stored in air for two days, before re-introducing it into the UHV chamber (column "Oxidation *ex situ*" of table 4). The oxidized sample was analyzed and then annealed in three steps. The purpose of the experiment was to study the oxidation of a V layer on a fullerene thin film under environmental conditions.

In experiment number four, the permeability of a fullerene film with respect to oxygen was investigated (column "Oxidation *in situ*" of table 4). For this, a monolayer of vanadium was buried inbetween a thick  $C_{60}$  substrate layer and a

3 *ML* film of  $C_{60}$  deposited on top of the vanadium. This sandwich structure was then exposed twice to an oxygen atmosphere of  $1 \cdot 10^{-2}$  *mbar*  $O_2$  for 5 minutes. After the oxidation, the sample was also annealed in three steps to investigate the reactivity and thermal stability of the V within the  $C_{60}$  film.

Fig. 29 shows the substrate core level intensity for a step by step deposition of fractions of a monolayer of V on a 20 *nm*  $C_{60}$  thin film. Even though the V deposition takes place in UHV (background pressure  $\sim 6 \cdot 10^{-10}$  *mbar*,  $\sim 10^{-9}$  *mbar* during deposition), the film exhibits a measurable oxygen content, which scales with the V coverage. This is probably due to the high reactivity of the vanadium. Most likely the oxygen stems directly from the deposition process, since the oxygen content does not increase during the measurements, only after deposition steps. The concentration measured after each deposition step is close to that expected for a layer-by-layer growth model, which is represented by the Lambert-Beer function (the black and blue line in fig. 29).

The small deviation from the Lambert-Beer function could be due to the fact that the surface of a fullerene substrate is not flat as with other materials. The curvature of the molecules leads to an increase in surface area compared to a flat substrate. Therefore, a larger number of atoms is needed to cover the whole surface. Employing a simple geometrical estimate, the surface of a fullerene substrate should be about 10% bigger than that of a flat substrate like HOPG, for example. The modified Lambert-Beer function is represented by the dashed lines. Also, the  $C_{60}$  substrate is not likely to grow as a flat layer on HOPG. Therefore the surface

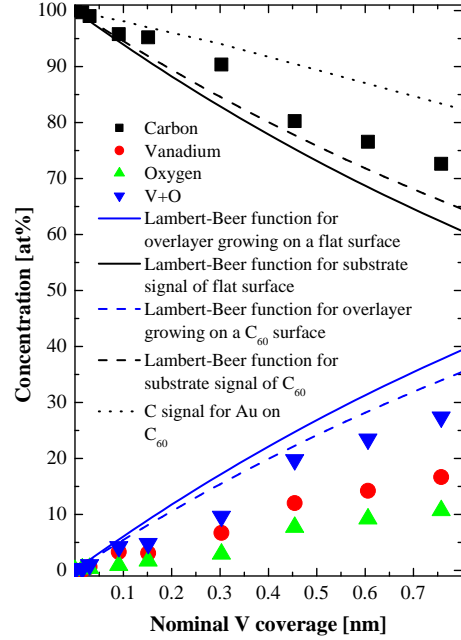


Figure 29: Intensity of the substrate core level as a function of the amount of V deposited onto  $C_{60}$ . The dotted line indicates the substrate signal intensity for the deposition of Au on  $C_{60}$  from fig. 22, the black and blue lines are the representation of the Lambert-Beer function for a layer-by-layer growth model on a flat and a  $C_{60}$  surface (dashed).

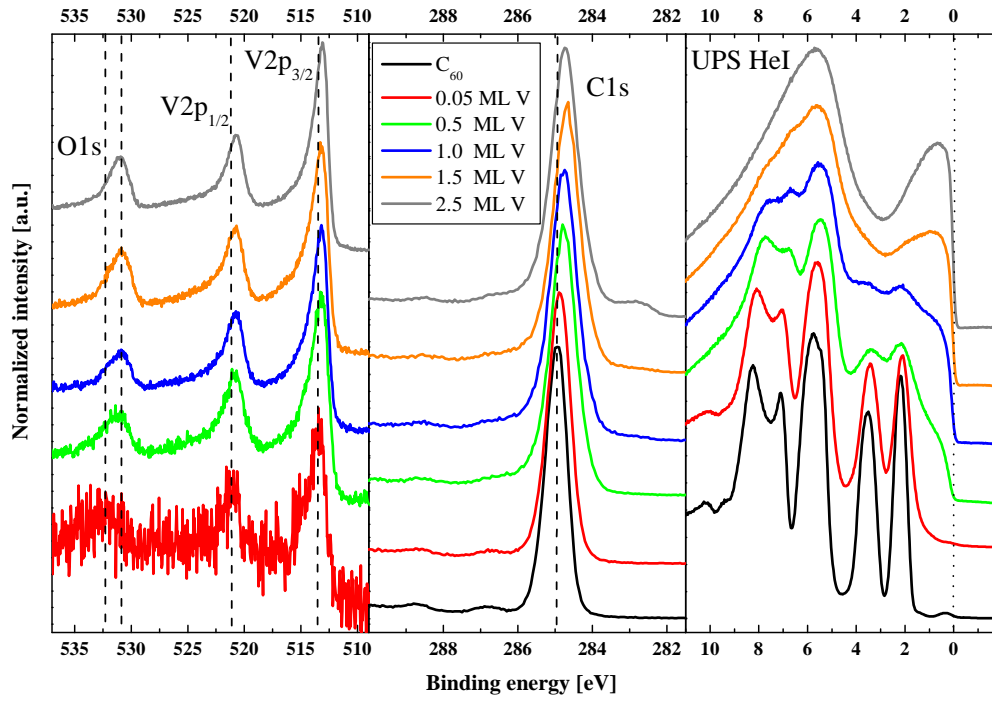


Figure 30: Overlayer formation of V on  $C_{60}$ . Left: Selection of the core level spectra of the  $O1s$ ,  $V2p_{1/2}$ , and  $V2p_{3/2}$  measured with MXPS ( $h\nu = 1486.6 \text{ eV}$ ). Middle: MXPS  $C1s$  core level spectra. Right: UPS HeI ( $h\nu = 21.22 \text{ eV}$ ) VB spectra.

roughness of the  $C_{60}$  substrate will be rather large, which could also cause a further deviation from the Lambert-Beer function. The growth of the vanadium overlayer, closely resembling a layer-by-layer growth, is in contrast to the deposition of most other elements onto a fullerene surface. As seen in chapter 4.1, Au deposited on  $C_{60}$  deviates strongly from the layer-by-layer growth model (dotted line in fig. 29), indicating a cluster formation. Especially if one considers the highly corrugated surface, this wetting effect of the forming layer of V and O is unexpected. The stoichiometry suggests that the layer is not exclusively forming one of the known vanadium oxides, as there is less than one oxygen atom per vanadium atom. The oxygen in the layer may, however, be contained in small amounts of those oxides.

A selection of some of the core level spectra of the vanadium  $2p$  core levels and

the oxygen  $1s$  core level, the carbon  $1s$  core level is given in fig. 30 along with some of the VB spectra measured with UPS HeI. The development of the  $C1s$  peak is shown in the middle part of fig. 30. In the  $C1s$  spectra, the appearance of a carbide peak at  $282.7\text{ eV}$  is observed for coverages exceeding  $1.0\text{ ML}$  of V, which corresponds to approximately  $0.3\text{ nm}$ . This is comparable to results for an overlayer formation of chromium on  $C_{60}$  found by Ohno *et al.* [237]. In their work, they find that chromium deposition leads to carbide formation, which can be seen first in the spectra for an overlayer thickness of  $0.4\text{ nm}$ . Since chromium and vanadium are chemically very similar it is not an unexpected result that for the vanadium deposition the same effect is observed. The fraction of the  $C1s$  that corresponds to a carbide increases from about  $0.7\%$  for a nominal coverage of  $1.5\text{ ML V}$  to  $2.8\%$  for  $2.5\text{ ML V}$ . The position of the carbide  $C1s$  is in good agreement with the literature at  $282.7\text{ eV}$  [238]. The position of the fullerene  $C1s$  shifts slightly from an initial binding energy of  $284.9\text{ eV}$  for pure  $C_{60}$  down to a constant  $284.8\text{ eV}$  for nominal vanadium coverages of  $0.5\text{ ML}$  and above. As in the case of gold (see chapter 4.1), this is probably due to a chemical interaction of the vanadium and the fullerenes, which is supported by the carbide formation at higher coverages.

This development is not as apparent in the evolution of the vanadium core levels depicted in the left part of fig. 30. The  $V2p_{3/2}$  core level for a nominal coverage of  $0.05\text{ ML V}$  ( $0.015\text{ nm}$ ) is positioned at  $513.3\text{ eV}$ , which corresponds to the binding energy of metallic vanadium. Increasing nominal coverage leads to a shift towards lower binding energy. The binding energy starts off at the metallic vanadium position and shifts towards the carbide position, which according to literature is at  $513.0\text{ eV}$  [239]. Usually, for small metal clusters a shift towards higher binding energies compared to that of the bulk metal would be expected. Due to the chemical interaction with the oxygen as well as with the carbon, the possible influence of cluster formation cannot be determined.

The oxygen signal in the core level spectra shows a double peak. The main signal is located at  $530.8\text{ eV}$ . There is, however, a slight shoulder at  $532.4\text{ eV}$ . This peak get less intense compared to the main feature with increasing nominal coverage. The origin of this feature is unclear. It is close to the binding energy of oxygen bound to carbon [240, 241], even though that is very unlikely, as there is no indication of that in the  $C1s$  core level spectra. There are numerous possible

binding environments for the oxygen in the system with similar binding energies and therefore an unequivocal assignment cannot be achieved.

The corresponding VB spectra measured with UPS (HeI) are shown in the right-hand part of fig. 30. Like in the C1s core level spectra, there is a slight shift of the fullerene-related features towards lower binding energies. With increasing nominal V coverage the spectra show the development of a Fermi edge. For a nominal coverage of 0.5 *ML* V the Fermi edge is shifted 0.2 *eV* towards higher binding energy. This can either be due to a shift of the metallic Fermi edge, or it could also be that the vanadium and the oxide form a mixed-valence oxide. Most of the mixed-valence vanadium oxides are semi-conductors, which show a Mott-Hubbard metal-insulator transition. At room temperatures, the only metallic mixed-valence vanadium oxide is  $V_2O_3$ . For higher nominal coverages (1.5 *ML* and above) a distinct Fermi edge is visible in the UPS spectra. This again shows the metallic character of the deposited overlayer, which corresponds to the observed binding energy of the  $V2p_{3/2}$  core level. The vanadium oxides (except for  $V_2O_3$ ) do not show a Fermi edge, the only other possibility for its formation could be vanadium carbide. Both the metallic oxide as well as the carbide show a low density of states at the Fermi edge, which manifests itself in a soft slope. The spectra here show a very steep slope at the Fermi edge, indicating that it is dominated by metallic vanadium. The large peak at about 6 *eV* stems from the oxygen contained in the deposited overlayer. The peak is comparatively large because the photo-excitation cross-section of UPS HeI for oxygen is large.

In the next step, the deposited sample was annealed. The composition as a function of the annealing temperature is shown in fig. 31. The vanadium concentration in the annealing experiment stays constant for all temperatures. The spectra were taken while the sample was kept at the depicted temperature, and UPS spectra taken at the beginning of the measurement are identical to those taken after the core level measurements. The carbide fraction of the C1s increases linearly up to an annealing temperature of about 550 °C. Annealing at a higher temperature does not affect the carbide formation further. For an annealing temperature of 565 °C, the oxygen content of the overlayer decreases, and at 735 °C the oxygen has almost completely disappeared. This indicates that the formation of a vanadium oxide on a fullerene substrate is energetically less favorable than the formation of the vana-

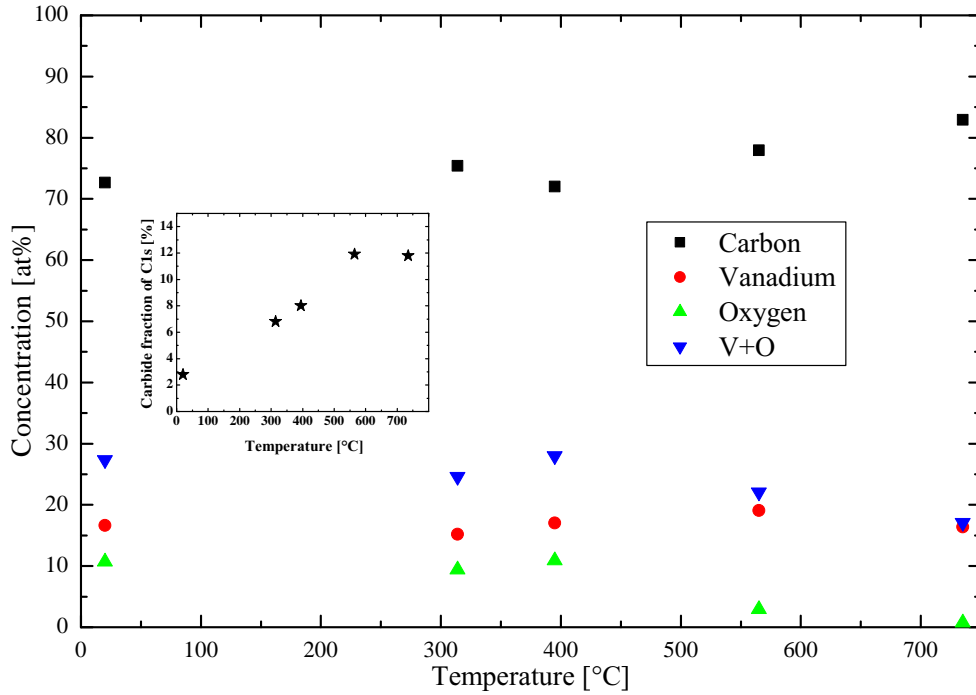


Figure 31: Concentration of V, C, and O as a function of the annealing temperature for an overlayer of  $0.75 \text{ nm}$  V on  $C_{60}$ . The inset shows the fraction of the C1s that corresponds to a carbide as function of annealing temperature.

dium carbide. It should be pointed out that the sample appears to be exceptionally stable, as even for the highest annealing temperature there is no loss of vanadium or of  $C_{60}$ . This would probably be seen by change of the vanadium concentration in fig. 31, or from a shift of the C1s core level. The spectra for the annealing of the V and O overlayer on  $C_{60}$  are shown in the bottom row of fig. 32. The C1s core level is shown in the middle part of the figure, and there is no shift of the core level binding energy towards the binding energy of the C1s in HOPG after the final annealing step.

The  $V2p$  and  $O1s$  core levels for annealing of the vanadium and oxygen

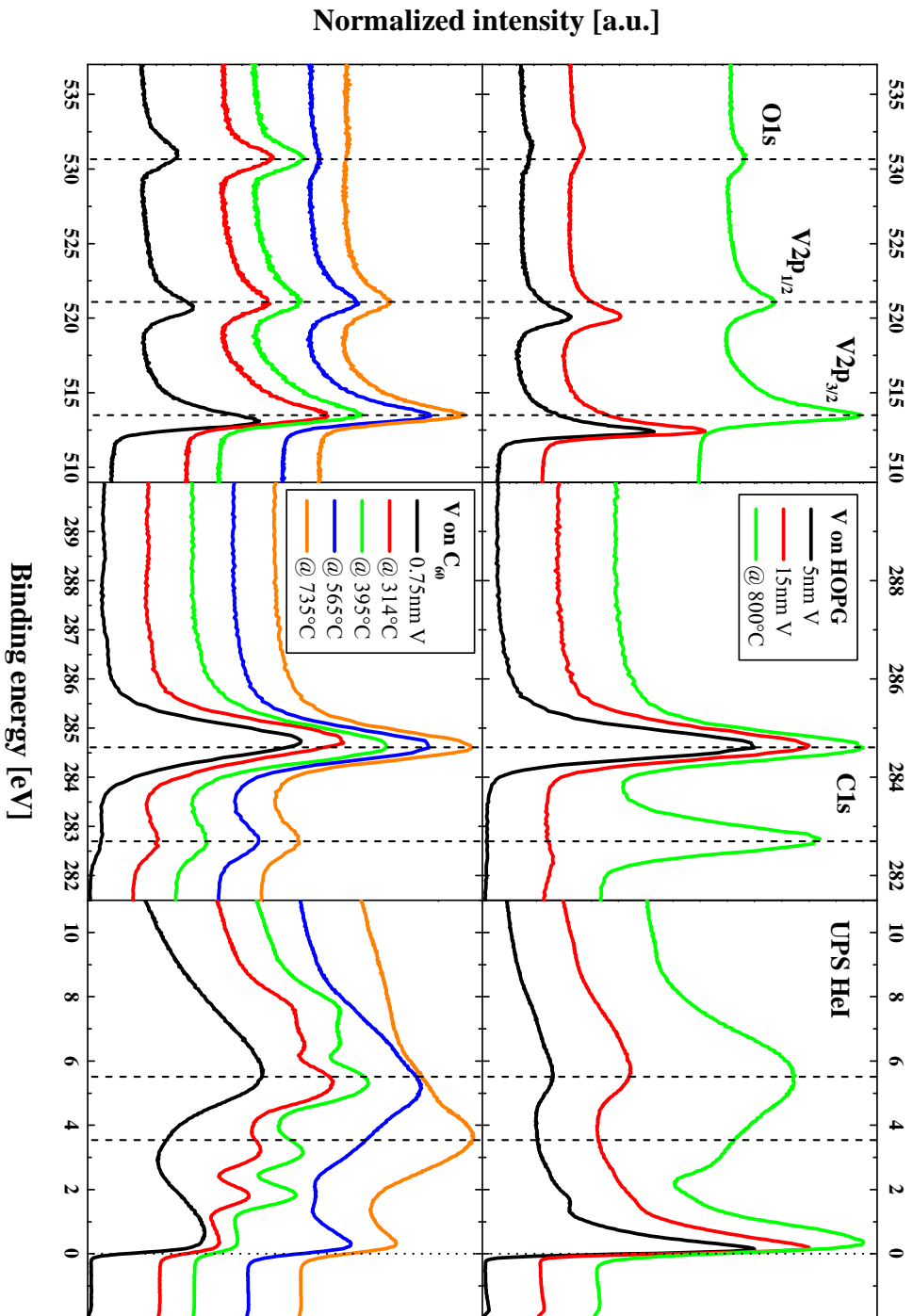


Figure 32: MXPS ( $h\nu = 1486.6$  eV) core level and UPS ( $h\nu = 21.22$  eV) VB spectra taken during annealing. Top row: V on HOPG. Bottom row: V on  $C_{60}$ .



overlayer on  $C_{60}$  are shown in the left part of the bottom row of fig. 32. For the first annealing step of  $314\text{ }^{\circ}\text{C}$  the high binding energy side of the  $V2p_{3/2}$  core level develops a broader shoulder. The enlarged region of the  $V2p_{3/2}$  normalized to unit height is shown in fig. 33. This contribution most likely stems from an increase in vanadium with an oxidation state of  $4+$ , which is associated with  $VO_2$ . Values for the binding energies of the vanadium and oxygen core levels vary in the literature. Some of the core level binding energies for vanadium oxides are listed in table 5. According to Demeter *et al.*, the  $4+$  oxidation state corresponds to a core level binding energy of  $516\text{ eV}$  [242], while Sawatzky and Post found a value of  $516.2\text{ eV}$  (see table 5). When the oxygen content of the sample drops from  $10\text{ at}\%$  to  $3\text{ at}\%$  at an annealing temperature of  $565\text{ }^{\circ}\text{C}$ , the shoulder on the high energy side disappears again, indicating that the oxide is breaking up. The center of the  $V2p_{3/2}$  core level shifts after the first annealing step towards higher binding energy. This is in

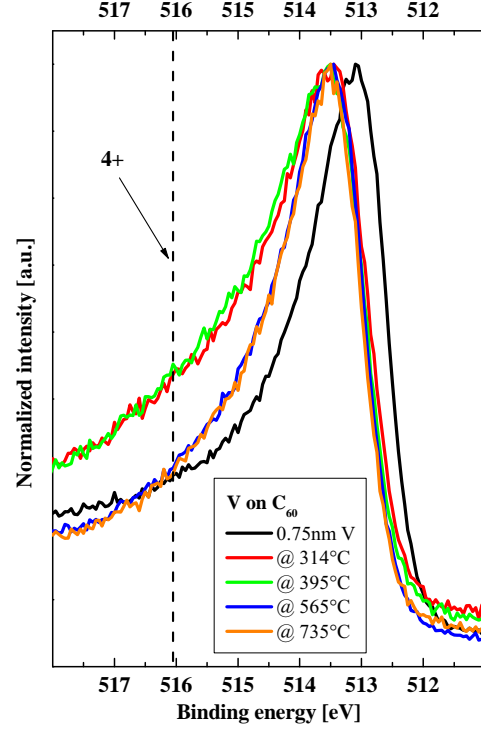


Figure 33:  $V2p_{3/2}$  core level measured with XPS for the annealing of  $0.75\text{ nm V}$  on  $C_{60}$ , normalized to unit height. The line indicates the binding energy value of the  $V2p_{3/2}$   $4+$  oxidation state.

Material	O1s binding energy	$V2p_{3/2}$ binding energy	$V2p_{1/2}$ binding energy
$V_2O_5$	$529.8\text{ eV}$	$516.9\text{ eV}$	$524.3\text{ eV}$
$VO_2$	$529.9\text{ eV}$	$516.2\text{ eV}$	$523.5\text{ eV}$
$V_2O_3$	$530.1\text{ eV}$	$515.7\text{ eV}$	$523.3\text{ eV}$
$V$		$512.4\text{ eV}$	$519.9\text{ eV}$

Table 5: Core level binding energies at room temperature of some of the mixed-valence vanadium oxides and metallic vanadium (adapted from ref. [243]).

agreement with the increase in the carbide fraction of the C1s core level. However, from the core level spectra it is difficult to tell how much of the vanadium is bound to carbon, but the binding energy of the V2p<sub>3/2</sub> core level agrees with that associated with vanadium carbide (indicated by the dashed line in fig. 32).

While the core level spectra for annealing of the overlayer of V and O on C<sub>60</sub> in the bottom row of fig. 32 reveal only minor changes in the binding energies, the UPS VB spectra in the right-hand part show some more drastic changes in the top layer of the sample. The spectrum of the vanadium and oxygen overlayer (shown in black) clearly resembles a metallic vanadium film with oxygen (dotted line at 5.6 eV) and carbide (dotted line at 3.8 eV) contributions. Annealing at 314 °C leads to the reappearance of the characteristic fullerene peaks. Therefore, there appears to be a rearrangement of the surface layer. Judging from the core level spectra, it seems possible that the formerly closed layer breaks up and at least partially forms a vanadium oxide cluster layer, revealing part of the fullerene substrate in the process. The oxidation is in agreement with the shift of the vanadium core levels to higher binding energies. At the same time the concentration of V and C in fig. 31 remains almost constant. This indicates a possible mixing of the vanadium and carbon from the fullerenes in the forming VC structure. If the carbon stays underneath the growing layer, then there should be a change in the concentration ratios. The fullerene features remain visible until the annealing step of 565 °C, when the UPS spectrum mainly shows metallic V and with an oxygen contribution again, even though the core level spectra show that the oxygen concentration in the sample drops significantly. This indicates that the film might undergo a transition back from clusters to a layer, thus covering the fullerene surface. This would suppress the detection of the fullerene contribution. The fullerene-related peak is still visible in the C1s core level spectra, and a complete transformation into the carbide is therefore excluded. The strong oxygen signal is due to the high sensitivity of UPS to oxygen. In the last annealing step the oxygen is almost completely depleted, and the UPS signal drops accordingly. This reveals the weaker carbide related peak at about 3.8 eV. All of the UPS spectra for this experiment show a clear Fermi edge due to the metallic character of the deposited overlayer.

To compare the growth of the vanadium overlayer to a flat surface of mainly  $\pi$ -bound carbon, a thick film of vanadium was deposited on to HOPG. In two steps

a thickness of approximately 15 nm was deposited, and then annealed in a single step at 800 °C. The core level and UPS VB spectra for this experiment are shown in the top row of fig. 32. This film contains less oxygen than in the stepwise deposition of V on  $C_{60}$  discussed previously. The reason for this is probably the higher temperature of the evaporation source, which was used to achieve a higher deposition rate and deposit 15 nm V in a reasonable amount of time. This high rate could not be employed for the sub-monolayer coverages. The C1s core level is shown in the middle part of fig. 32. For the deposition steps of V on HOPG, there is clearly less carbide formation than there is for V on  $C_{60}$ . The analysis of the substrate signal strength as a function of the deposited amount of V is shown in fig. 34. There is a strong deviation from the layer-by-layer growth described by the Lambert-Beer function, in contrast to the growth on the highly corrugated  $C_{60}$  surface. Annealing at 800 °C leads to a strong carbide formation. 45 % of the C1s intensity is contained in the peak at the carbide binding energy. This also indicates that the binding energy of 513.4 eV of the  $V2p_{3/2}$  for this layer is representative of vanadium carbide, even though this is not in agreement with the literature (513.0 eV [239]). Most likely, this is due to the presence of oxygen in the film, which shifts the binding energy to higher binding energy. The position of the carbide  $V2p_{3/2}$  peak from the deposition of V on HOPG is in good agreement with that from the annealed V layer on  $C_{60}$  with a carbide fraction of 11.4 % and a very low oxygen contribution, showing that the data are consistent. The annealing leads to a loss of vanadium from the analyzing range of MXPS. This

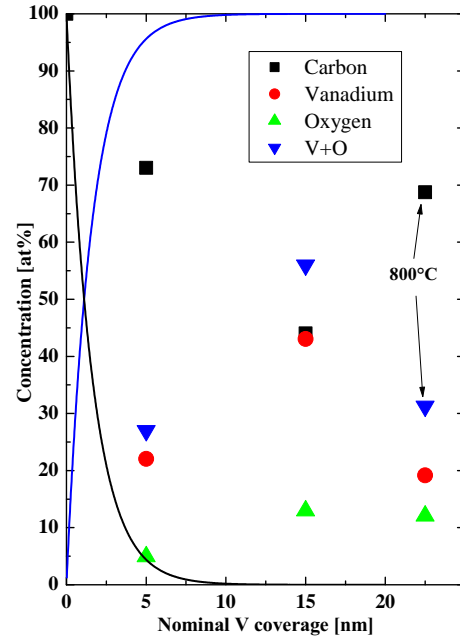


Figure 34: Intensity of the substrate core level as a function of the amount of V deposited onto HOPG. The lines are the representation of the Lambert-Beer function for a layer-by-layer growth model (black for the substrate signal, blue for the overlayer signal).

could be due to a mixing of vanadium and carbon, which is indicated by the strong carbide peak in the C1s core level. It could also represent a diffusion of vanadium into the graphite substrate. The vanadium core level does not show any sign of an oxygen component. Interestingly, the oxygen content remains constant during this annealing, which is contrary to the annealing of V on  $C_{60}$ , where during annealing the oxygen leaves the film. Comparing the UPS VB spectra to that of V on  $C_{60}$ , one can see that the assignment of the 3.8 eV feature to carbide and of 5.8 eV to oxygen is correct. The deposited film shows a steep Fermi edge, that gets less steep during the annealing. This is consistent with the formation of VC, which has a lower density of states at the Fermi edge, which leads to a less steep slope.

In the next experiment, the oxidation *ex situ* in air of a V film on top of a  $C_{60}$  film was investigated. For the *ex situ* oxidation a fresh monolayer of vanadium was deposited on 20 nm of  $C_{60}$ . This sample was then taken out of the vacuum system and kept in air for two days before re-introducing it into the vacuum system. The sample surface was then investigated with PES and annealed according to the steps indicated in table 4. The results from the core level and UPS VB spectra are shown in the top row of fig. 35. The  $V2p_{3/2}$  core level clearly shows that after two days in air the metallic vanadium layer has been transformed into the insulating  $V_2O_5$ . The binding energy of 517.4 eV is in good agreement with the value reported by Dzhurinskii *et al.* [244], while it disagrees with that reported by Sawatzky *et al.* of 516.9 eV [243]. However, since  $V_2O_5$  is an insulator, it has a very distinct and clearly identifiable peak structure, and the binding energy is well separated from that of the other vanadium oxides. Therefore it is clear that the spectrum corresponds to  $V_2O_5$  and the dashed line through the  $V2p_{3/2}$  peak has been labeled "5+" according to the associated oxidation of the vanadium. The double peak structure of the O1s core level is due to the oxygen from the carbon-oxygen bonding environment, which is probably due to carbon dioxide that accumulated in the surface region during the two days in air. It causes the peak at the high binding energy side. This is supported by the C1s core level, which clearly shows a second peak that stems from carbon bound to oxygen at a binding energy of 286.5 eV.

Annealing at 320 °C causes strong changes in the overlayer configuration. The vanadium and oxygen core levels show that the  $V_2O_5$  is almost completely

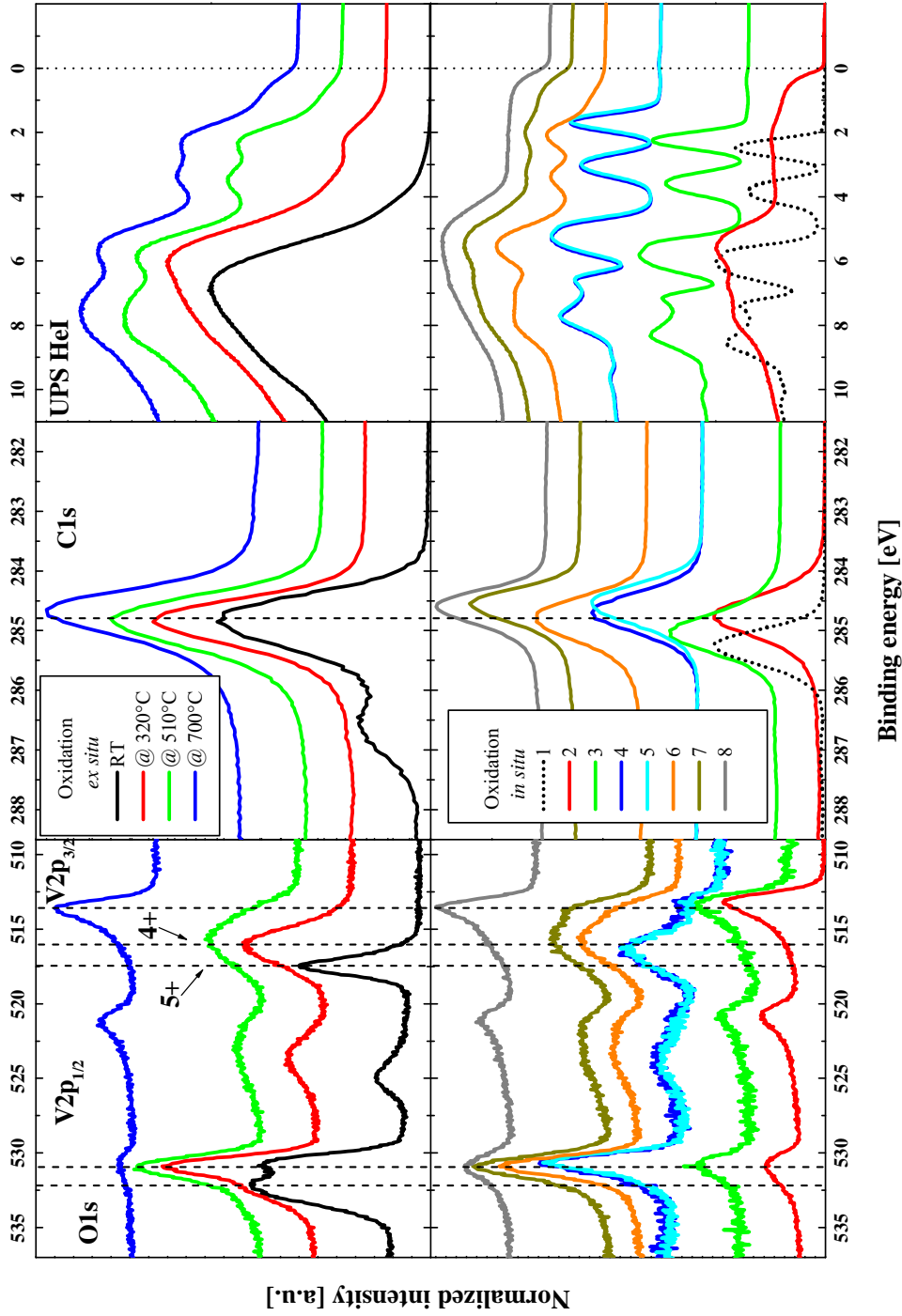


Figure 35: MXPS ( $h\nu = 1486.6 \text{ eV}$ ) core level and UPS ( $h\nu = 21.22 \text{ eV}$ ) VB spectra measured during *in situ* and *ex situ* oxidation of V on top of  $C_{60}$  and V buried within a  $C_{60}$  film. Top row: 1 *ML* V on  $C_{60}$ , measurement after 2 days in air. Bottom row: 1 *ML* V buried underneath 3 *ML*  $C_{60}$ . The caption is according to table 4.

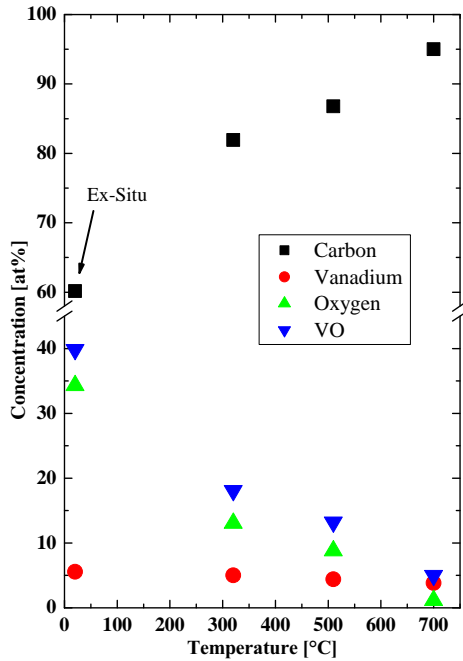


Figure 36: Intensity of the fullerene substrate C1s core level as a function of the annealing temperature for the *ex situ* oxidation of 1 ML V on  $C_{60}$ .

dium. This is supported by results from the C1s core level spectra, which no longer show signs of carbon dioxide. The VB spectra do not show any sign of the fullerene substrate, therefore it can be assumed that the layer is closed.

At 510 °C the layer is modified again. The  $V2p_{3/2}$  core level exhibits signs of metallic V again, as well as  $V^{5+}$ , which was almost completely absent at 320 °C. The vanadium concentration in the sample stays constant throughout the annealing process, only the oxygen concentration drops with increasing annealing temperature (see fig. 36). There is no apparent change in the C1s core level for this annealing step, but the VB spectrum shows signs of fullerene features. This indicates that with the change of the vanadium oxide configuration the layer breaks up, revealing part of the substrate. Along with the small metallic fraction of the V core level there seems to be a Fermi edge forming in the VB spectrum. There is no formation of vanadium carbide for this annealing temperature. This could either be due to the presence of the oxygen in the layer or the fact that there is too little vanadium

transformed into a different mixed-valence oxide. Judging from the peak shape of the O1s [243] it is most likely  $VO_2$ . The binding energy of the  $V2p_{3/2}$  (515.95 eV) is also in good agreement with this interpretation. The position of this peak has therefore been assigned the "4+" label. At this temperature there appears to be no contribution from metallic vanadium, which would be visible at the right hand dashed line. This is supported by the UPS VB spectra, which do not show a Fermi edge (see the top right of fig. 35). For the room temperature UPS spectra this is expected, as there will be a lot of adsorbed water or carbon dioxide from the prolonged exposure to air. The first annealing step will lead to a desorption or reaction of the adsorbates with the vanadium.

present to trigger the carbide formation. In the spectra for the deposition of V on  $C_{60}$  the carbide formation onset is the deposition step from 1.0  $ML$  to 1.5  $ML$  V (see fig. 32).

In the last annealing step, the oxygen almost completely leaves the vanadium layer, just like in the annealing of the sequential deposition experiment (see top left of fig. 32). The vanadium core levels return to their metallic state, although the position is shifted to higher binding energy by 0.5  $eV$  compared to the freshly deposited film. The position of the  $C1s$  core level, however, matches that from the freshly deposited sample. The VB spectrum for this annealing step changes only slightly. The developing Fermi edge gets steeper, but is still shifted. The fullerene features are less pronounced, but still clearly visible. In the spectrum of the stepwise deposition for the same nominal coverage (blue spectrum in the right part of fig. 30) there is a fully developed Fermi edge and the fullerene features have almost completely vanished. As the V concentration for 1  $ML$  V from the stepwise deposition matches that of V in this experiment at 700  $^{\circ}C$ , there appears to be a different topography. Part of the fullerene substrate in this case is still accessible by UPS, indicating that the vanadium layer may not be closed, possibly due to the formation of islands. These may also cause the shift in binding energy of the vanadium core level as mentioned above.

Finally, the last experiment was designed to test the permeability of a fullerene layer. For this a monolayer of vanadium was buried underneath 3  $ML$  of  $C_{60}$ . The core level and VB UPS spectra measured are shown in the bottom row of fig. 35. From the UPS spectrum of the deposited  $C_{60}$  on V it can be seen that there is a closed fullerene film on top of the vanadium. The spectrum is a perfect reproduction of the substrate fullerene film (dotted line), except that it is shifted to lower binding energy by 0.25  $eV$ . The same shift is visible in the  $C1s$  core level. Most likely, this is a band bending effect due to the chemical interaction of the vanadium with the carbon present in the fullerenes. The same kind of band bending is seen for the deposition of  $C_{60}$  on Au (see chapter 4.1 or ref. [221]). The vanadium core levels are shifted to slightly higher binding energy by almost the same amount that the  $C1s$  and VB fullerene features are shifted towards lower binding energy.

This buried layer was then exposed twice *in situ* to an oxygen atmosphere of  $1 \cdot 10^{-2}$   $mbar$   $O_2$  for five minutes (spectra labeled 4 and 5 in fig. 35). The changes

in the vanadium core level spectra are strong. For the first exposure, the  $V2p_{3/2}$  core level turns almost completely from a metallic to a  $4+$  state, resembling the spectrum for annealing the *ex situ* oxidized surface layer at  $320\text{ }^\circ\text{C}$ . However, there is still a small metallic component to the peak. The spectra clearly show that there is no more change for the second exposure, indicating that the oxygen content is saturated for this system. It seems that the system is highly permeable to oxygen. In contrast to the surface layer oxidation, the formation of  $V_2O_5$  is suppressed, which might be due to the surrounding fullerene matrix. Interestingly, the VB spectra for this oxidized system show a large shift of the fullerene features towards lower binding energy. The HOMO in this system is positioned at  $1.7\text{ eV}$ , a total shift of  $0.8\text{ eV}$  from its substrate position of  $2.5\text{ eV}$ . The spectra themselves are still a perfect reproduction of the substrate spectrum, except for the shift. The position of the HOMO is identical to that seen for the first layer of  $C_{60}$  in contact with a gold substrate (see fig. 27). In the case of the Au substrate it is most likely a chemisorption effect [221]. In the case at hand, it is more likely a Fermi level pinning at the interface and associated band bending, since the UPS VB spectra show only the molecules of the very surface. The interface to the buried monolayer of vanadium should be out of the depth-sensitivity range of the UPS method. In contrast to the  $C_{60}$  on Au system, the band bending is much stronger, but only once the vanadium has been oxidized. It could also be the influence of oxygen within the  $C_{60}$  layer, which may also lead to the band bending observed. The  $C1s$  core level is also shifted to lower binding energy and in fact this is the only apparent difference in the two oxidation steps. The shift increases for the second oxidation cycle, reaching the same value as that of the VB features.

Annealing the buried layer at  $300\text{ }^\circ\text{C}$  leads to the desorption of the fullerene layer on top of the vanadium. This can be seen from the VB spectrum, which corresponds to that for the *ex situ* oxidized surface layer annealed at  $510\text{ }^\circ\text{C}$ . This is expected, as the desorption temperature for fullerenes is about  $300\text{ }^\circ\text{C}$ . Since the features of the fullerenes are still visible, there may be residual fullerenes on the vanadium layer. The vanadium core level spectra also show that most of the fullerene layer covering the vanadium has disappeared, because the intensity of the vanadium signal is almost back to that of the non-buried layer. The structure of the  $V2p_{3/2}$  peak resembles that of the *ex situ* oxidized surface layer annealed at



510 °C, just like the VB spectrum does. It shows an oxidation value of mainly 4+ for the vanadium, with some admixture of 5+ and some metallic vanadium. All of the spectra taken at 300 °C for the buried layer look very similar to those of the surface layer at 510 °C. Since the main difference to the surface oxidation experiment is the covering layer of  $C_{60}$ , it seems that the presence of the  $C_{60}$  on top of the vanadium oxide layer lowers the energy necessary to reduce the oxidation state of the vanadium.

Increasing the annealing temperature to 500 °C does not bring about much change in any of the core level or VB spectra. The metallic fraction of the  $V2p_{3/2}$  core level increases slightly. The VB spectrum shows that at this temperature most of the remaining  $C_{60}$  molecules on the surface have desorbed as well, because the fullerene features are barely noticeable anymore. The most prominent change can be seen in the  $C1s$  core level, which shifts to lower binding energy. The reason for this remains unclear, as one would expect the binding energy to be the same as in the surface layer oxidation experiment (indicated by the dashed line).

In the final annealing step of 700 °C, most of the vanadium changes back to its metallic state. The  $V2p_{3/2}$  core level only shows a small admixture of the 4+ and 5+ oxidation states. However, there remains a comparatively large amount of oxygen in the vanadium layer. The VB spectrum exhibits no remaining fullerene features, showing a closed vanadium layer on top of the fullerene substrate. It even appears to be more fully closed than the initially deposited layer, which in comparison showed a slight presence of  $C_{60}$  related features.

### 4.2.1 Conclusions

The stepwise deposition of vanadium on a fullerene substrate shows a growth mode closely resembling a layer-by-layer growth, which can be described by the Lambert-Beer function. The deposited layer is comprised of 60 at% vanadium and 40 at% oxygen. The vanadium core levels show a metallic state, which indicates that the oxygen is not bound to the vanadium. For coverages exceeding 1 monolayer vanadium carbide is formed. In contrast to on the fullerene substrate, vanadium grows on HOPG in a cluster or island growth mode. In addition, at room temperature there is almost no detectable carbide formation for V on HOPG.

Annealing of V on  $C_{60}$  leads to increasing vanadium carbide formation. The

oxygen concentration drops for each annealing step, while the vanadium concentration remains constant. The core level analysis indicates a change in the oxidation state of the vanadium for annealing temperatures of 300 – 400 °C. A small fraction of the vanadium has a 4+ oxidation state. The 4+ oxidation state shows the formation of a vanadium oxide, but most of the vanadium is still metallic. The change in the oxidation state is accompanied by a structural change of the overlayer. The formerly closed overlayer breaks up and re-arranges itself into clusters or islands. Annealing at higher temperatures causes the overlayer to close up again. At the highest annealing temperature of 735 °C, there is no residual oxygen left in the vanadium layer. At this temperature, about 12% of the detected carbon atoms are bound to vanadium. For V on HOPG the carbide formation at high temperature (800 °C) is strong compared to that of V on  $C_{60}$ . Almost half of the detected carbon at this temperature is bound to vanadium. The detected vanadium concentration drops by 50%. This could either be due to diffusion of the vanadium into the HOPG or evaporation of the vanadium from the clusters or islands.

A monolayer of vanadium on top of a fullerene substrate exposed to air for two days is transformed into  $V_2O_5$ . Annealing of this film at 320 °C leads to a change in the oxidation state of the vanadium. The film is transformed into  $VO_2$  with an oxidation state of the vanadium of 4+. Annealing at higher temperatures leads to a transformation of the oxidation state of the vanadium. The core levels show a mixture of vanadium oxidation states of 0, 4+, and 5+, which reverts back to its metallic state for annealing at 700 °C. As for the annealing of V on  $C_{60}$ , the film is not entirely closed when the oxidation state has a 4+ component.

The permeability of a fullerene film with respect to oxygen was tested with a monolayer of vanadium buried under 3 ML of  $C_{60}$  by exposing it twice to an oxygen atmosphere of  $10^{-2}$  mbar  $O_2$  for 5 minutes. The first exposure leads to the oxidation of most of the vanadium, only a small metallic fraction remains. The second exposure to oxygen does not lead to further changes in the buried vanadium layer. This demonstrates that the permeability of  $C_{60}$  with respect to oxygen is high. The oxidized layer closely resembles the oxidized overlayer annealed at 320 °C. The dominant oxidation state of the vanadium after oxidation is 4+ and the oxide formed is  $VO_2$ . The  $C_{60}$  overlayer seems to prevent the vanadium from forming  $V_2O_5$ , instead it appears to favor the formation of  $VO_2$ . The C1s core level

---

and the VB spectra show a large shift of the fullerene-related peaks towards the Fermi energy. This indicates a chemical interaction of the vanadium oxide with the surrounding fullerene molecules. Annealing this oxidized sandwich structure leads to a desorption of the covering fullerene layers. Otherwise the formerly buried layer behaves similarly to the oxidized overlayer for annealing at higher temperatures.

## 5 3D systems

The gold 2D system showed the formation of clusters on a fullerene surface. The expansion of the system into three dimensions bears the possibility of creating clusters with a fullerene matrix. To investigate this, composite samples of  $C_{60}$  and materials, which seemed likely to grow clusters, were created by co-deposition of the two species under UHV conditions.

### 5.1 Gold

Thin films composed of fullerenes ( $C_{60}$ ) and gold (Au) were deposited onto p-type silicon, polished quartz, and copper TEM grids to accommodate the requirements for different analytical methods. The samples were prepared in a UHV chamber at a base pressure of  $1 \cdot 10^{-10} mbar$  by co-deposition of  $C_{60}$  and Au. The fullerenes were deposited from a BN crucible, which was heated by a tungsten filament wire wrapped around the crucible. Four different concentrations were used: 1.5 at% Au, 5 at% Au, 11 at% Au, and 25 at% Au. Thin films for each experiment were deposited onto all three kinds of substrates. For this, on the one side of the sample holder, a silicon substrate was mounted together with a TEM grid. On the other side of the sample holder, a quartz substrate was mounted. Before starting a deposition, the deposition rate of the two elements was determined by employing a quartz crystal monitor. The deposition rate of Au was determined prior to switching on the fullerene source. Subsequently, the Au beam was interrupted by a mechanical shutter and the fullerene deposition rate was established. The fullerene source was a broad beam source and mechanical shuttering proved to be inefficient. The sample was therefore exposed to a pure fullerene beam in the early stage of deposition until the evaporation rate of the  $C_{60}$  was fully stabilized. At this point the shutter to the gold beam was opened and a composite beam reached the substrate. Also, there was usually a slight drop in the fullerene deposition rate of about 10 % during the deposition of the sample. Final film thicknesses lay in the range of 20 – 30 nm.

The samples on Si were investigated with RBS to determine whether segregation of the gold occurs. Fig. 37 shows the RBS spectrum of the 25 at% Au sample and a fit to the data points. The distribution of Au throughout the sample is obtained from the fit, and the results are depicted in the inset. The error of the

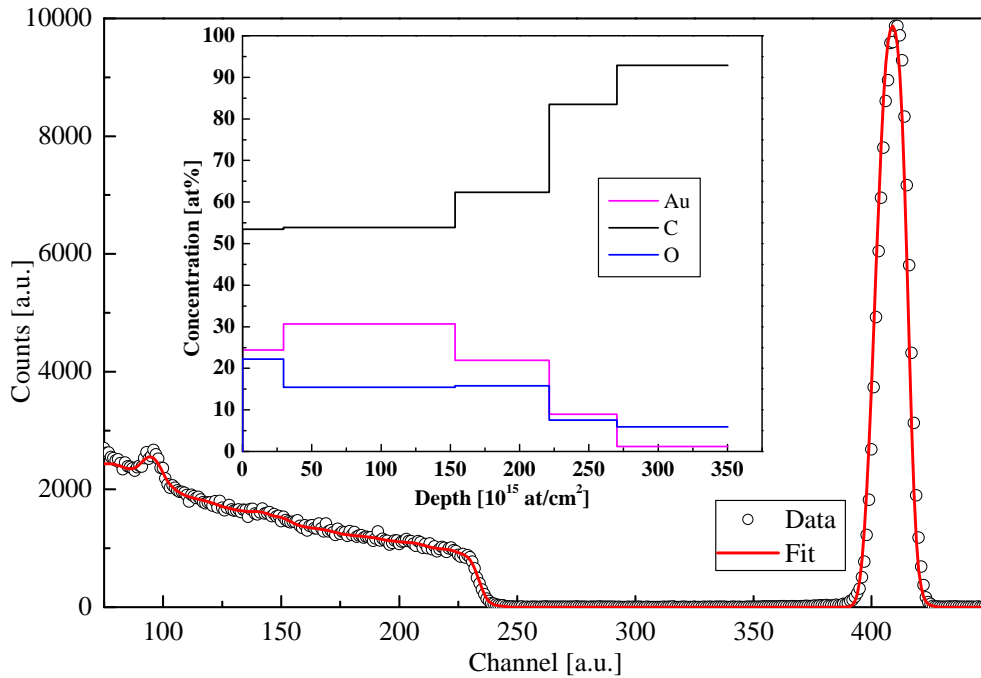


Figure 37: RBS spectrum of the 25 at% Au sample. The line represents the fit depicted in the inset.

fit is approximately  $\pm 2.5\%$ . At a depth of  $350 \cdot 10^{15} \text{ at/cm}^2$  the substrate begins. The distribution reflects the deposition sequence described above, and a lower Au concentration is observed closer to the substrate interface. After the initial increase in Au concentration the Au percentage in the sample stays relatively constant at about 25 at%. These two thirds of the film contain approximately 75 – 80 % of the Au in the film. Also, there is a high oxygen concentration visible in the spectrum. The relatively high oxygen concentration is attributable to the incorporation of water and other environmental gases in the film due to an extended exposure to air. The RBS causes irradiation damage and was therefore performed at the end of the sample characterization, about 8 weeks after the deposition. *In-situ* deposition and analysis of  $C_{60} - Au$  layers with X-ray photoelectron spectroscopy (XPS) at comparable base pressures show that the films are nearly oxygen free immediately

after deposition. Some  $Au - C_{60}$  samples were analyzed with XPS after prolonged storage in air and increased oxygen concentration is clearly present. The majority of the oxygen is bound in carboxyl or carbonate groups, which are identified by their characteristic chemical shift. The oxygen concentration in the RBS spectrum in 37 decreases as the gold concentration in the sample decreases. This could indicate an diffusion of oxygen into the sample. Another possibility would be that the Au is acting as a catalyst to oxidize the fullerene molecules. From the data gathered, it is not possible to decide on the role of the Au in the film. The RBS spectra for the other samples look similar, in every case the gold is distributed throughout the sample.

Fig. 38 shows four sample HRTEM micrographs of films containing 1.5 at% Au (top left), 5 at% Au (top right), 11 at% Au (bottom left), and 25 at% Au (bottom right). Numerous clusters are visible in every sample. There is a difference in cluster-size as well as cluster density in the pictures. The clusters are generally getting bigger for increasing Au concentration. Fast Fourier transform analysis of the HRTEM pictures shows that for the Au clusters showing lattice planes more than 90 % of the clusters are  $\langle 111 \rangle$  oriented. However, the cluster orientation with respect to each other is random, as opposed to ion implanted clusters which show a preferred orientation [245].

It is apparent in the TEM micrographs presented in fig. 38, that for higher Au concentrations the cluster-size increases, and the area density increases as well. In general, a larger cluster size and cluster density is observed for higher gold concentrations. As seen from the RBS spectra, about 70 – 80 % of the gold inventory is located in the sample section with a stable Au concentration, while the rest is located in the interface region to the substrate, which is characterized by a decreasing Au concentration. Fig. 39 shows the cluster-size distribution as a function of Au concentration. The Au cluster size is directly related to the concentration of the Au in the matrix (see TEM image for 1.5 at% Au in fig. 38), and the region closer to the substrate will therefore only contribute to the smaller cluster-size side of the size distribution shown in fig. 39. For low Au concentrations the cluster-size distribution is very narrow, with a mean cluster-size of about 1.8 nm for the lowest Au concentration of 1.5 at%, and 2 nm for the sample with 5 at% Au, respectively. The envelope of the distribution can be described by a Gaussian distribution for

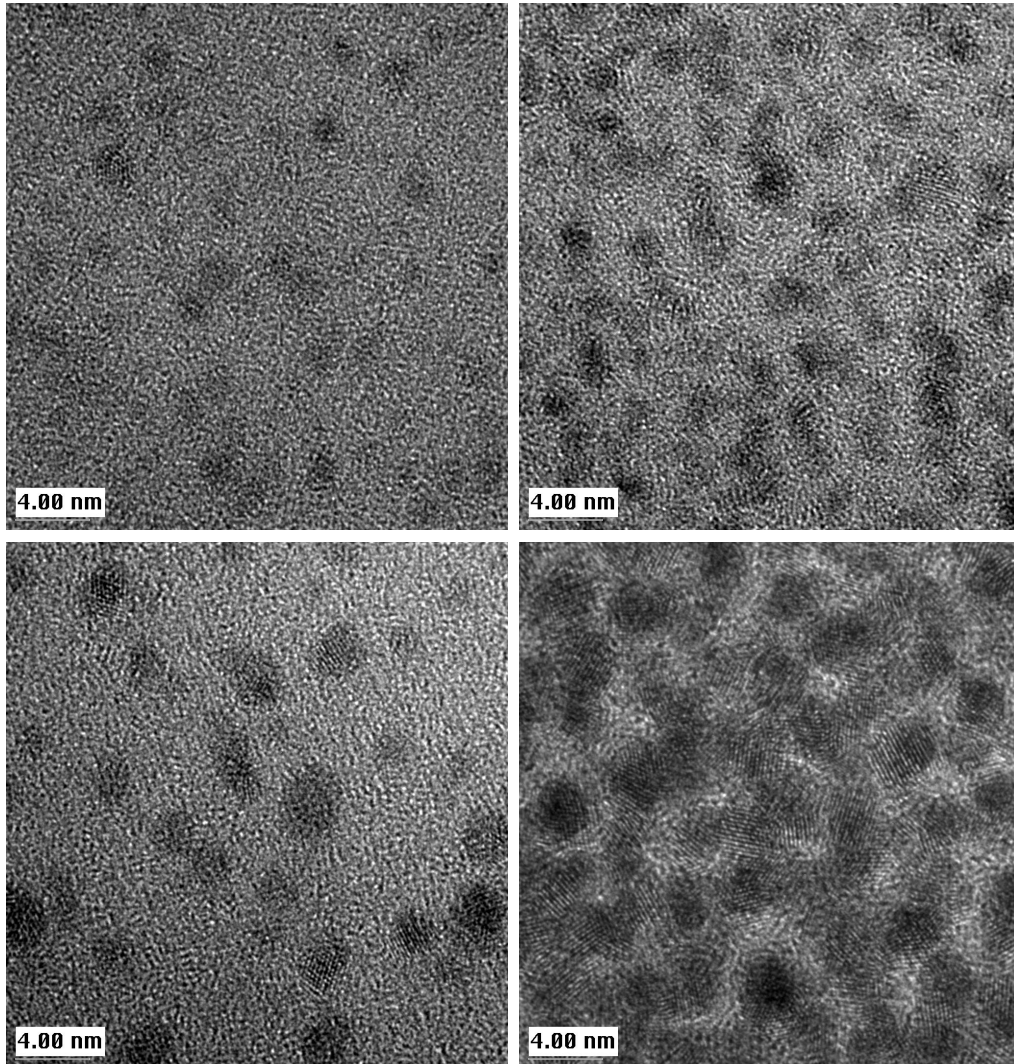


Figure 38: High resolution plain view TEM micrographs of samples with 1.5 *at%* Au (top left), 5 *at%* Au (top right), 11 *at%* Au (bottom left), and 25 *at%* Au (bottom right)

these two samples, and the full width at half maximum (FWHM) is about 0.4 *nm*. This is a narrow size distribution compared to clusters produced by other methods [246, 22, 247, 248]. For higher Au concentrations the distribution is significantly broadened and shifts to larger cluster-sizes. Also, these distributions cannot be

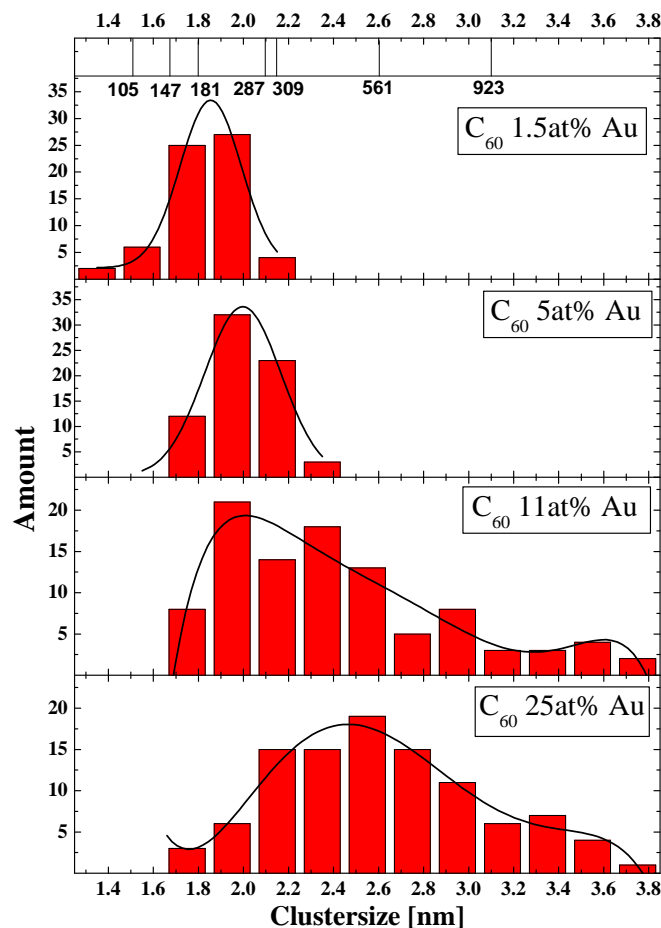


Figure 39: Size distribution of the Au clusters for the four different deposited Au concentrations. The theoretical size of magic clusters is indicated in the top of the figure, and the number is the actual number of Au atoms in those clusters. The data was compiled from all of the HRTEM pictures obtained.

fitted by a Gaussian distribution. To account for the broadening and the asymmetry of the distribution of the 11 at% Au and 25 at% Au samples, a high order polynomial had to be used. The FWHM for these envelopes is about twice that of the Gaussian's for the low concentrations.

For free clusters there are certain cluster sizes, which exhibit exceptional stability due to their symmetric configuration, the so called magic clusters [150]. They are



considered to be thermodynamically more stable, and, at least for  $Au_{55}$ , this has been demonstrated experimentally [151]. However, for clusters within a dielectric matrix, it is unclear whether the closed shell configuration is still energetically preferable. The cluster size distributions for higher Au concentrations at 11 *at%* and 25 *at%* in fig. 39 exhibit maxima at certain cluster sizes, indicative of an increased stability of some cluster sizes. It has to be conceded that these fluctuations in the size distribution are close to the limit of the statistical reliability of the analysis and a larger number of samples is required in the future to unambiguously support this observation. Some of the maxima appear to coincide with the size of magic clusters, but a simplified approach has been employed here, because the calculation of the actual cluster size requires a knowledge of the lattice structure and cluster density. For the estimate of the cluster size used in fig. 39, it was assumed that

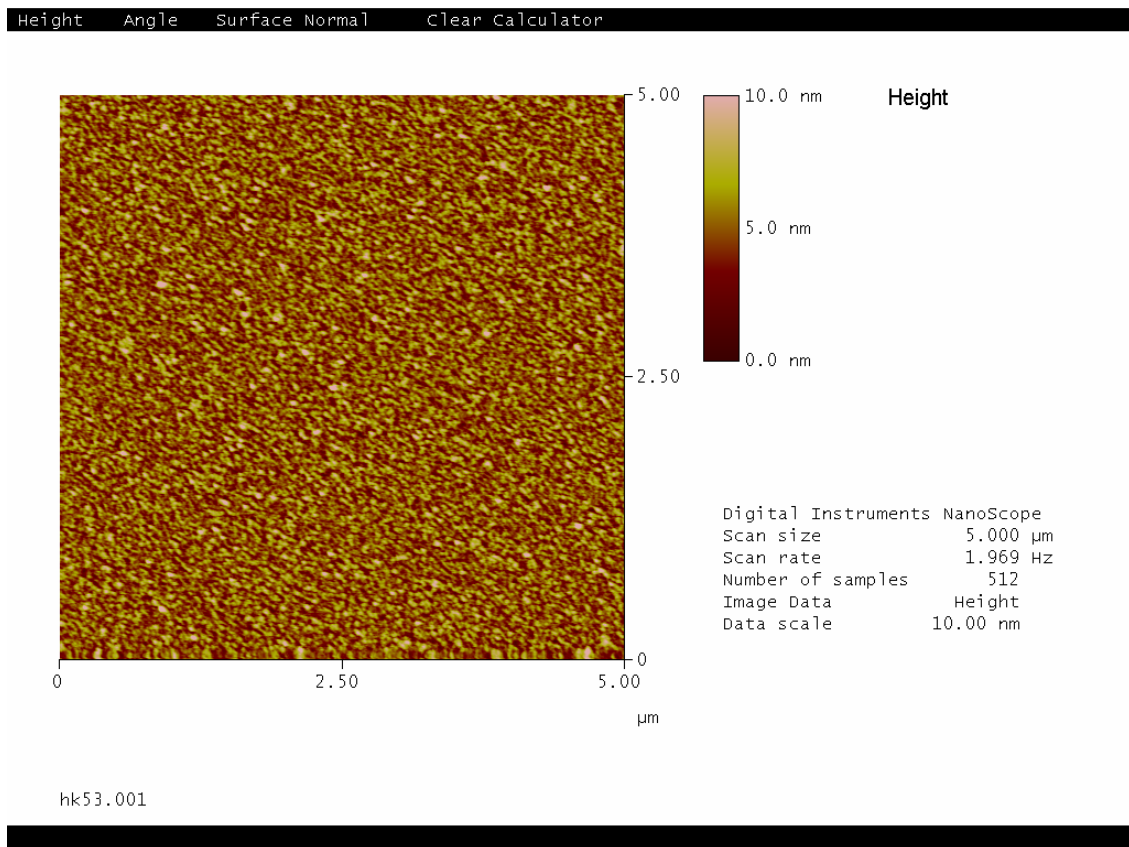


Figure 40: AFM image of the surface of a composite sample of  $C_{60}$  and 11 *at%* Au.

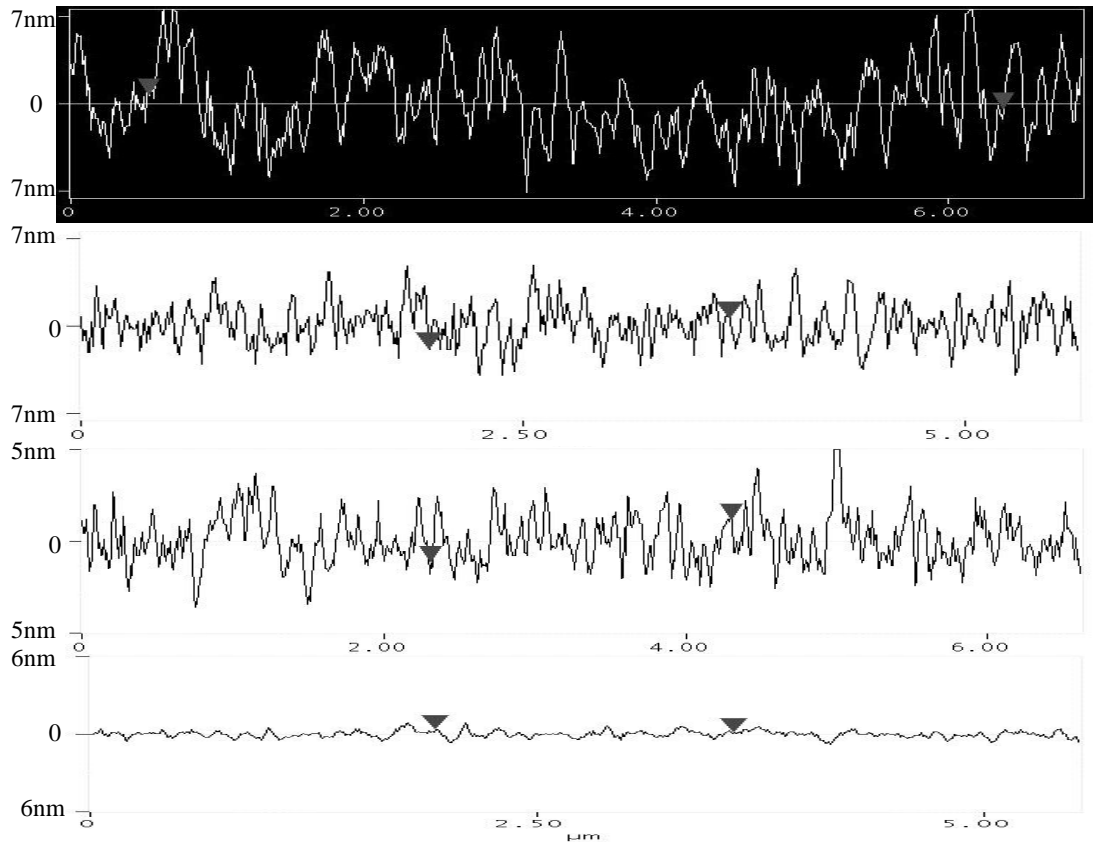


Figure 41: AFM linescans of samples of  $C_{60}$  (top), 5 at% Au (second from top), 11 at% Au (third from top), and 25 at% Au (bottom).

the Au atoms occupy a volume, which is defined by a sphere with the diameter of the lattice constant of Au  $\langle 111 \rangle$ . In fact, cluster sizes in the literature for  $Au_{55}$  vary from 1.4 to 1.6 nm, whereas the estimate employed here yields 1.2 nm. Future investigations will focus on the influence of the matrix on the cluster size distribution.

The surface of the deposited samples was also investigated. The surface topography is closely related to the growth mechanism of a thin film. The roughness of a surface is a decisive characteristic as to its use for optical applications. To investigate this, AFM was employed, which allows to determine the topography and the roughness of the thin film surface. The convolution of the surface topography with the AFM tip limits the resolution, and clusters with a diameter in the nanometer

range cannot be resolved.

Fig. 40 shows an example of an AFM image of the surface of a composite sample of  $C_{60}$  and 11 *at%* Au. The surface appears to be smooth, and there are no structures visible in the image that have the dimension of the clusters seen in the TEM micrographs. The smallest features in any of the images are still about 30 *nm* in size, whereas TEM shows that the size of the Au clusters is in the size range of about 2 – 4 *nm*. An overview of the linescans of the samples of pure  $C_{60}$ , 5 *at%* Au, 11 *at%* Au, and 25 *at%* Au is given in fig. 41. There is clearly a decreasing surface roughness for increasing Au concentration in the samples. Fig. 42 shows a comparison of the cluster size from the TEM measurements and the mean roughness

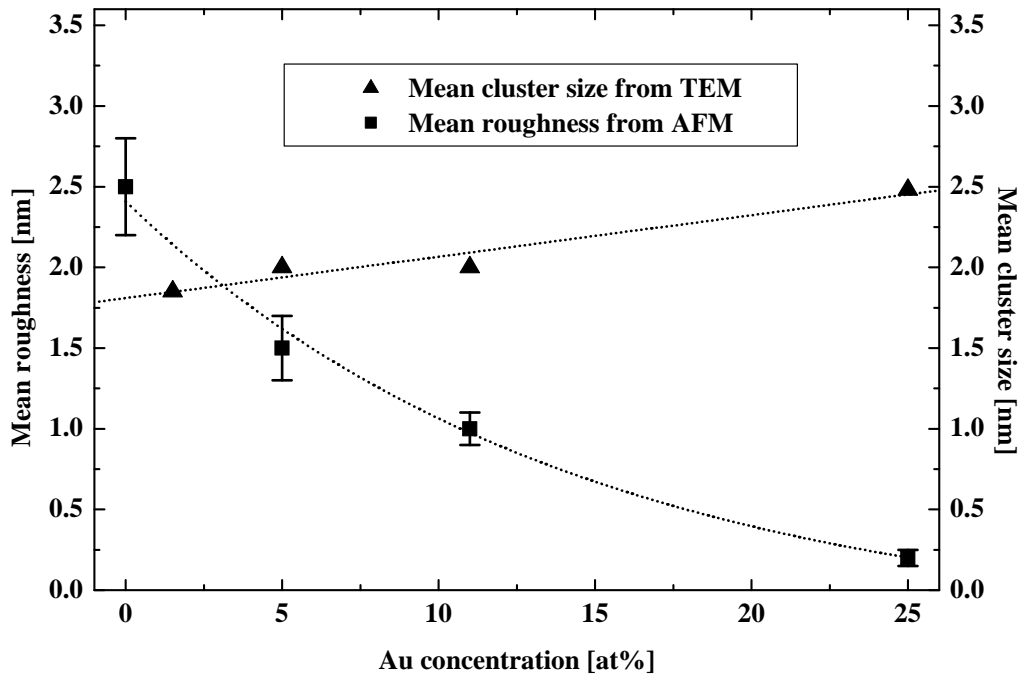


Figure 42: Comparison of the mean roughness  $R_a$  with Au cluster size from TEM measurements as a function of nominal coverage. The mean Au cluster size for the samples is ascertained from the maximum of the respective cluster size distribution in fig. 39. The lines are included as a guide for the eye.

$R_a$  from the AFM measurements.  $R_a$  decreases with increasing Au content, as does the lateral dimension of the features in the AFM images. On the other hand, the cluster size determined by TEM increases with increasing nominal coverage. Not only does the average roughness decrease, but also the absolute height differences between peaks and valleys decreases as the Au concentration increases. The pure  $C_{60}$  sample surface shows height differences of up to 20 nm (which is a stack of 20 fullerene molecules), whereas the 25 at% Au sample shows peak to valley height differences of at most half a nm. This is well below the diameter of a fullerene molecule and shows that the presence of gold leads to a smoothing of the surface. The smoothing may be due to a kind of surfactant effect, i.e. the Au clusters provide further nucleation centers for the fullerene molecules. That way, the film closes up more rapidly compared to the growth of a pure  $C_{60}$  film on Si.

To investigate the interaction of the Au clusters with the fullerene matrix, PL spectra of the composite samples were taken at 10 K. It has to be noted, that the Au clusters appear to show no luminescence in the composite samples produced for this work. Due to an (as of yet) unexplained artifact of the PL setup in the range of the expected cluster luminescence, the discussion has to be restricted to the influence of the Au on the luminescence of the  $C_{60}$  molecules. Usually, nanosize Au clusters exhibit a broad PL peak at about 440 nm, which is due to a blue shifted surface plasmon of the clusters [249]. The results for the PL of the  $C_{60}$  in the composite samples are shown in fig. 43. The pure  $C_{60}$  film shows the typical luminescence of poly-crystalline fullerene films [250, 251, 252, 212]. The main feature at 1.7 eV is sometimes referred to as the zero phonon line (ZPL), which is caused by an exciton polaron process. The features at lower energies are mainly due to impurities in the crystal, which offer radiative de-excitation centers different from the fullerene lattice. In the case at hand, the impurities will consist mainly of water, which propagates into the samples during prolonged exposure to air. These features are considerably smaller than the ZPL. Spectra taken at higher temperatures are usually dominated by these features [250, 212], as the rotation of the  $C_{60}$  molecules hinders the ZPL de-excitation. The rotation of the  $C_{60}$  molecules starts to freeze at 261 °K (see chapter 2.1.3). The last degree of freedom generally freezes below 90 °K. The main modification of the spectra for low Au concentrations is a red-shift of the features of the spectra. The ZPL shifts by

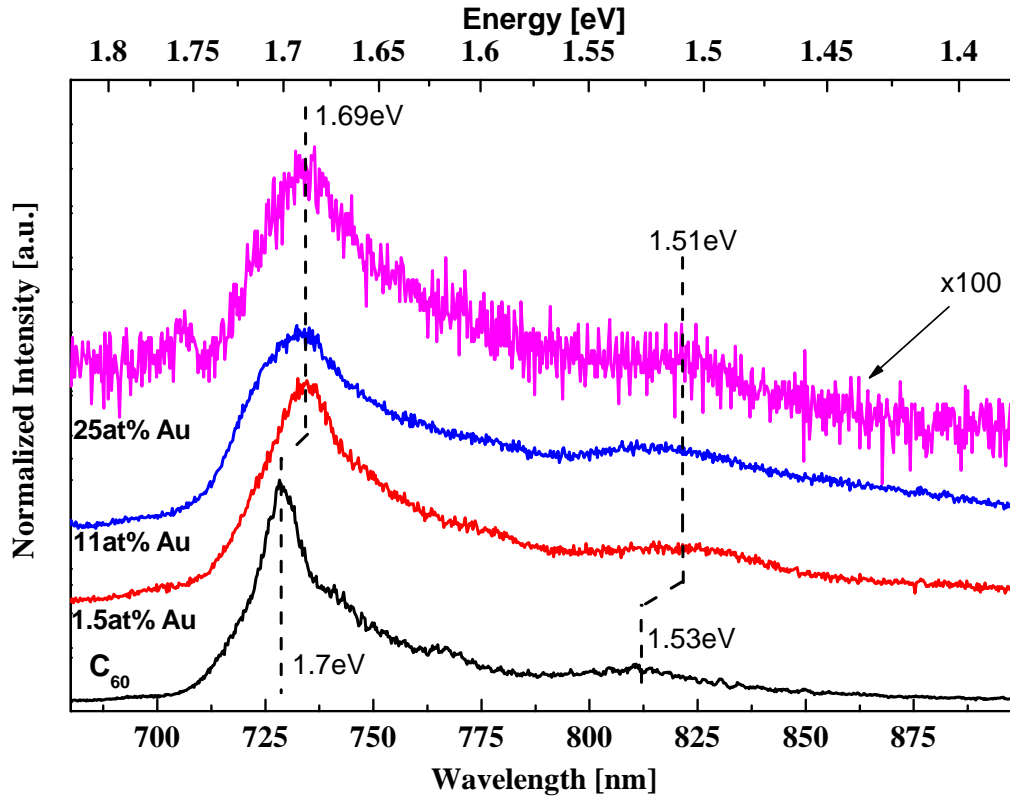


Figure 43: Normalized PL spectra of samples with three different concentrations of Au and a pure  $C_{60}$  film. The spectra were taken at  $T = 10 K$ .

0.01 eV towards lower energies. The broad peak at about 1.5 eV also shifts towards lower energies, although in this case the shift is more difficult to determine. This red shift is probably due to a chemisorption of the Au to the fullerene molecules, which is in agreement with results from the 2D experiments, in which  $C_{60}$  was deposited on a Au substrate and investigated by photoelectron spectroscopy (see chapter 4.1 and ref [221]). The experiment showed that the first layer of  $C_{60}$  is chemisorbed. In a composite sample, the Au clusters are spread throughout the thin film. Therefore, many of the  $C_{60}$  molecules are in contact with a gold clusters. This in turn means, that probably most of the molecules in contact with an Au cluster will also be chemisorbed to it. This possibly could cause the observed red

shift in the fullerene luminescence. In addition, the defect luminescence increases compared to the ZPL, which is expected, as additional defects in the lattice are introduced by adding Au atoms to the growing  $C_{60}$  crystal. The ZPL broadens and there appears to be a second component, expressed as a weak shoulder on the high energy side of the ZPL at about  $1.71\text{ eV}$ . It gains in intensity with increasing Au content. As the underlying structure of the poly-crystalline  $C_{60}$  luminescence is very complex, it is difficult to attribute this second component to a specific transition. The overall intensity of the luminescence drops by about 20% for the 11 *at%*Au film, which is reasonable, as the overall amount of  $C_{60}$  molecules is reduced as the Au content increases. The most significant change in the spectra occurs for a high Au concentration of 25 *at%*. The spectrum for this concentration shown in fig. 43 is multiplied by a factor of 100. For this high Au concentration the luminescence is almost completely subdued. Intriguingly, what little remains of the luminescence still looks like the spectrum for a lower Au content, the features are red shifted compared to the pure  $C_{60}$  luminescence. The decrease in luminescence most probably is due to an increase of radiationless transitions provided by the large amount of Au clusters in the sample. The spectra seem to indicate that this is not a linear phenomenon, as the drop in luminescence intensity of the 25 *at%* Au sample is much stronger than what would be expected under this assumption. The reason for this radical change in luminescence intensity is unclear, but not entirely unexpected, as a large portion of the film consists of Au. However, the PL results clearly show that the gold clusters are only weakly interacting for concentrations of 11 *at%*Au and less, as the fullerene based luminescence is only weakly affected by the presence of the gold. Because of the complex structure of the PL spectra, a detailed analysis will require an analytical simulation of the spectra. This way, the influence of the Au clusters on the PL of the fullerene molecules could probably be determined.

Further insight into the interaction of the two species in the films can be gained by investigating the optical properties with UV-Visible spectroscopy. Fig. 44 shows an overview of the normalized transmission spectra of the investigated samples. The high energy part of the spectra is clearly dominated by the fullerene features, as can be seen by the inset in fig. 44. The absorption maxima correspond well to the  $C_{60}$  level scheme depicted in the inset. The maximum at  $2\text{ eV}$  is only weak

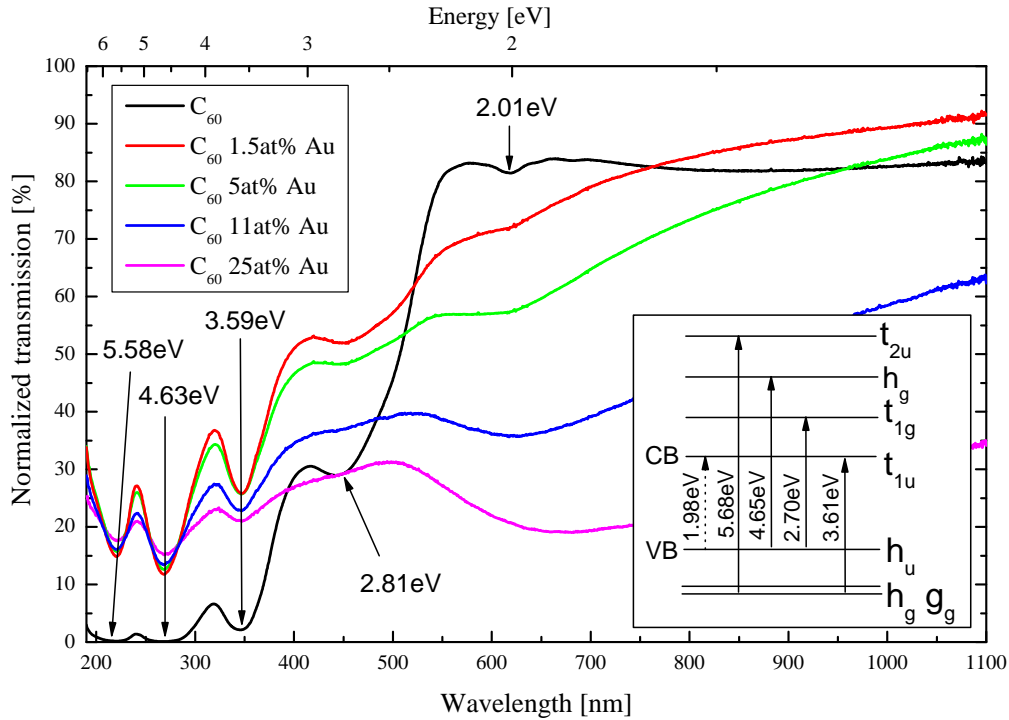


Figure 44: Normalized transmission spectra of the composite samples. The inset shows the corresponding level scheme of  $C_{60}$  (after ref. [252]).

because the bandgap transition is optically forbidden. The three features at  $5.58\text{ eV}$ ,  $4.63\text{ eV}$ , and  $3.59\text{ eV}$  change only slightly with increasing Au content. The most prominent change happens in the first step to a gold content of  $1.5\text{ at}\%$ , for which the absorption decreases by approximately  $10 - 15\%$ . Higher Au content only leads to slight changes in this regime. The influence of the gold is mostly limited to the low energy part of the absorption spectra. The strongest changes are visible in the regime between  $1$  and  $3\text{ eV}$ . The maximum at  $2.7\text{ eV}$  is flattened out and almost undetectable for a gold concentration of  $11\text{ at}\%$  and higher. The formation of a bond between Au and  $C_{60}$  is unlikely, as there is no indication of a preferred bonding site for Au on a 2D fullerene surface (see chapter 4.1). A possible explanation could be that the scattering from the gold atoms leads to the increase in transmission

at this specific energy. A surface plasmon peak is expected for small Au clusters at an energy of about 2.3 eV or approximately 530 nm (see fig. 7 in chapter 2.2). There is a change in the low energy region of the spectrum, which slowly gains intensity with increasing Au content, but is clearly positioned at lower energies in the spectra. If this is the plasmon peak of the Au clusters, the red shift could be due to the influence of the surrounding fullerene matrix. A dielectric matrix like the fullerenes can cause the plasmon peak of Au clusters to broaden [246], which might be the case here.

### 5.1.1 Conclusions

It has been demonstrated that it is possible to grow Au clusters with a very narrow size distribution within a fullerene thin film by co-deposition of Au and  $C_{60}$ . The cluster size is controlled by the amount of gold incorporated into the film. The cluster sizes range from about 1.6 nm at the lowest Au concentration to about 4 nm for the highest Au concentration of 25 at%. The clusters are dispersed throughout the film and no segregation is observed. The film topography strongly depends on the amount of gold in the film. With increasing Au concentration the mean roughness of the surface decreases from 2.5 nm for pure  $C_{60}$  to 0.2 nm for films with 25 at% Au, which is well below the diameter of a  $C_{60}$  molecule. This could be due to the Au clusters providing new nucleation sites for the co-deposited  $C_{60}$  molecules.

The optical properties of the composite films have been investigated with PL and UV-VIS. The PL signal from the fullerenes in the film is slightly red shifted for films containing Au clusters. The shift seems to be independent of the Au concentration in the sample. The intensity of the PL decreases with increasing Au concentration, and the structure of the luminescence changes. With increasing Au concentration, the ZPL intensity decreases while the defect related peaks gain in intensity. This is to be expected, because for increasing Au concentration there are more clusters in the sample, which can provide radiative de-excitation centers different from the fullerene lattice. The fact that the overall structure of the luminescence still resembles the known fullerene luminescence, and that it is not significantly quenched for Au concentrations below 25 at% shows, that the Au clusters are not strongly interacting with the surrounding fullerene matrix. From the UV-VIS it is clear, that the



$C_{60}$  molecules remain intact, because the absorption seen in the transmission spectra clearly resembles that of a fullerene sample. The transmission increases slightly for all samples containing Au. The most prominent changes in the spectra appear in the energy range below 2.5 eV. This is most likely due to a surface plasmon of the Au clusters. As also seen from the PL spectra, the interaction of Au with the surrounding  $C_{60}$  matrix seen in the UV-VIS spectra appears to be only small.

## 5.2 Germanium and iron

Thin films containing  $C_{60}$  and varying concentrations of germanium (Ge) as well as  $C_{60}$  with varying concentrations of iron (Fe) were deposited onto p-type silicon, quartz, and TEM grids. As with the  $C_{60}$  Au composite samples, these were analyzed with PL, UV-VIS, and TEM.

Since germanium is chemically quite similar to silicon, it is likely that it will also form clusters like silicon has been shown to do on  $C_{60}$  [12]. There are also strong indications that germanium forms clusters on  $C_{60}$  [10]. To investigate the possible cluster formation of the germanium, the samples were measured with TEM. Unfortunately it was not possible to achieve high-resolution TEM micrographs for any of the germanium samples. The image always appeared to be vibrating, which could be due to a charging effect in the samples. The inability to stabilize the images is most likely connected to the semiconducting nature of both Ge and  $C_{60}$ . The cluster formation in the Ge/ $C_{60}$  system can therefore not be studied with TEM. RBS spectra confirm that an even distribution of Ge throughout the thickness of the film can be achieved (see fig. 45), in agreement with the observations from Au and iron samples. This indicates that composite samples of Ge and  $C_{60}$  can be synthesized by co-deposition of the two species by thermal evaporation, in the same manner that it has been achieved for silicon [13] and Au.

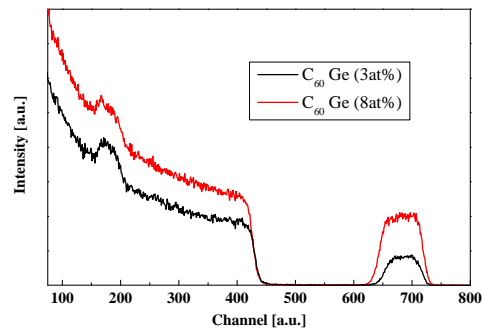


Figure 45: RBS spectra of two composite samples of  $C_{60}$  and Ge.

The samples deposited on silicon substrates were used to investigate the lumi-

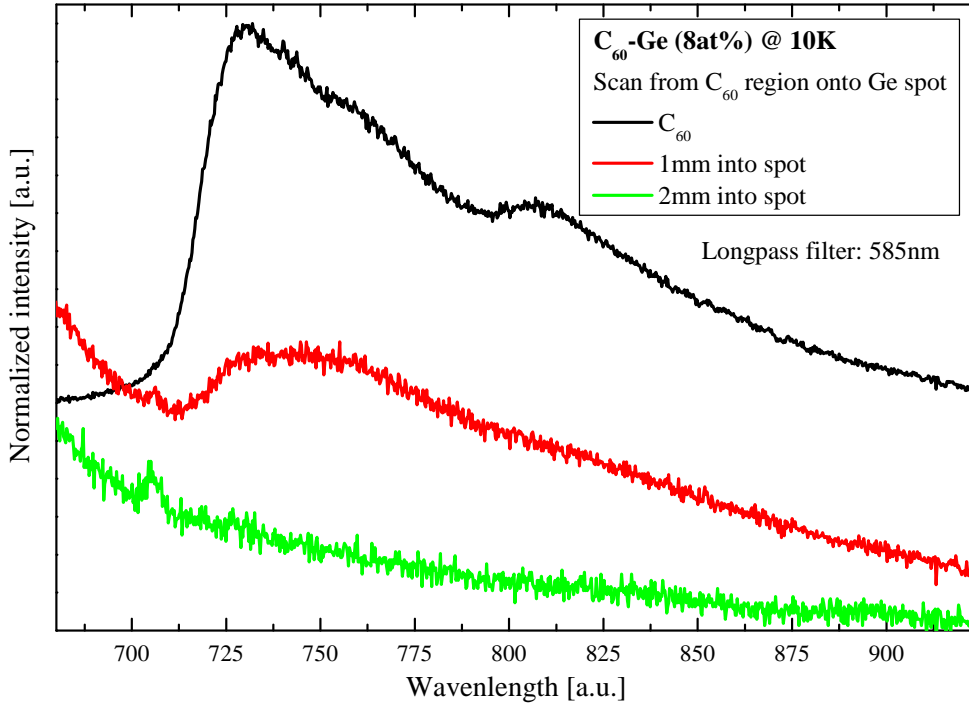


Figure 46: PL spectra for the composite sample of  $C_{60}$  and 8 at% Ge. The spectra show the PL intensity for moving the target area of the excitation laser from a pure  $C_{60}$  region onto the beam spot of the deposited Ge.

nescence properties of the composite films. Fig. 46 shows the PL spectra for a composite sample of  $C_{60}$  and 8 at% Ge. The spectra were measured at 10 K and the luminescence light passed a long pass filter (cutoff: 585 nm). The black colored spectrum stems from a pure  $C_{60}$  region right outside the area in which Ge was deposited. The intensity of the luminescence signal rapidly drops when the target area of the excitation laser is moved into the mixed  $C_{60}$ -Ge area (red colored spectrum) of the sample. Once the incident light from the excitation laser is completely within the composite area of the sample, the  $C_{60}$  luminescence is no longer detectable. The presence of the germanium in the fullerene matrix seems to effectively quench the indigenous  $C_{60}$  luminescence. This effect is not limited to higher germanium con-

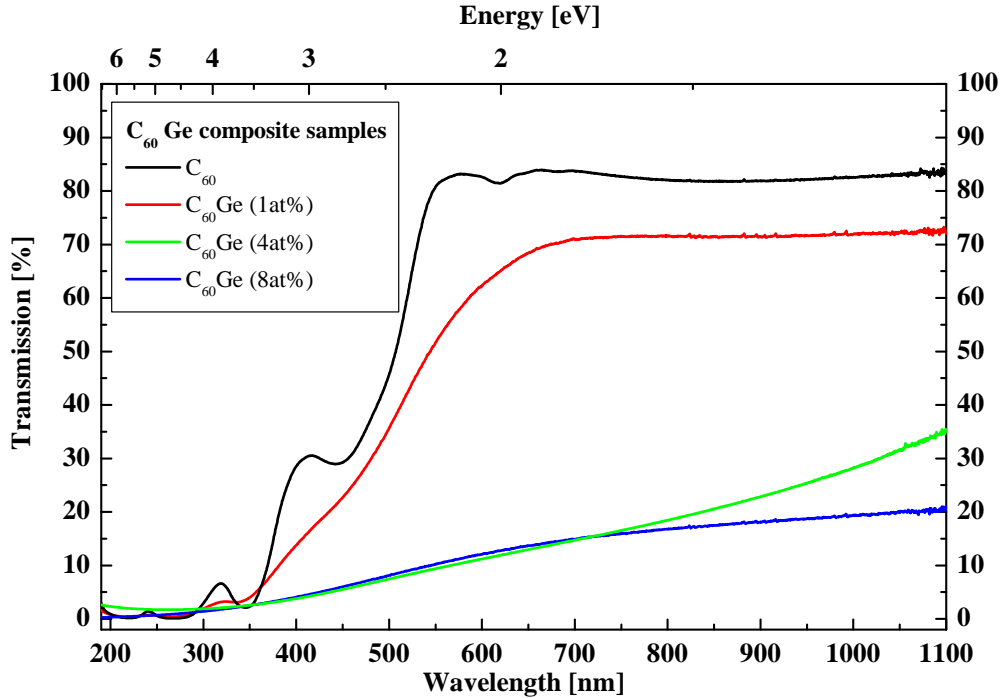


Figure 47: Transmission spectra of composite samples made up of  $C_{60}$  and varying concentrations of germanium.

centrations. None of the composite samples containing germanium showed fullerene luminescence and the smallest Ge concentration was 1 *at%*. The possible luminescence expected at about 1.1 *eV* or 1100 *nm* for germanium nanoclusters in the size regime of 1 – 9 *nm* was absent.

The samples were also investigated with UV-VIS spectroscopy. The transmission spectra recorded are shown in fig. 47. From the spectra, it can be seen clearly that even for a germanium content of only 1 *at%*, the typical fullerene absorption maxima flatten out. At this Ge concentration, an absorption edge is still discernible. For higher Ge concentrations, the spectra level out almost completely. This indicates a strong interaction of the germanium with the surrounding fullerene matrix. Due to the complications with the TEM measurements, the decision was made to first focus on the Au- $C_{60}$  system and the reactivity of the V- $C_{60}$  system. The development of

the Ge- $C_{60}$  system was not pursued any further.

The formation of a binary cluster material made up of iron and  $C_{60}$  was also investigated by TEM and the goal was to produce magnetic clusters in a densely packed 3D structure. Iron was chosen specifically, since the Fe bonding environment in the 3D Fe- $C_{60}$  system can be investigated in detail with Mössbauer spectroscopy. Like with germanium, the TEM analysis of the nanoclusters was also elusive for the Fe- $C_{60}$  system. While clusters could be seen by the TEM operator, the clusters appeared to disintegrate when exposed to the electron beam for more than a few seconds. Therefore, no pictures of iron clusters can be presented here. Molecular-

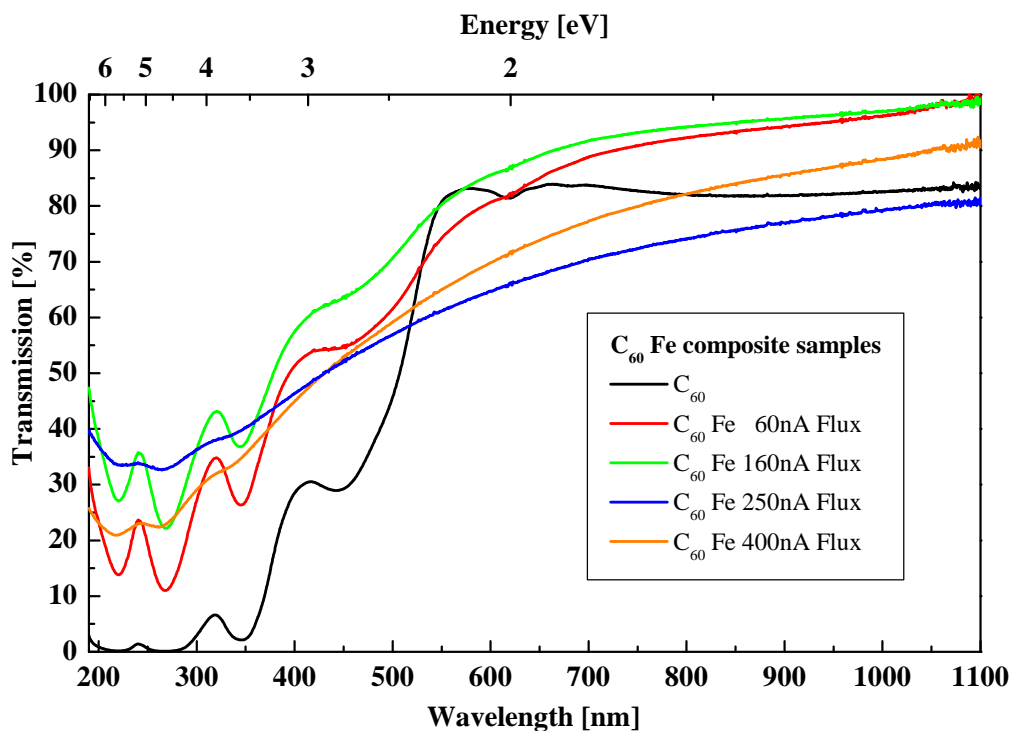


Figure 48: Transmission spectra of composite samples of  $C_{60}$  and varying concentrations of iron. The concentration could not be determined by the use of the quartz crystal monitor. This is probably due to a misalignment of the crucible containing the iron. The flux is measured by the EBE and is directly proportional to the deposited iron concentration.

dynamics studies on the melting of iron nano-clusters suggest that the surface of the clusters melts at far lower temperatures than expected [253, 254], but still at temperatures of about 800 °C, which cannot be reached within a TEM electron beam. The clusters produced here are likely to be oxidized, as the permeability of the  $C_{60}$  with respect to oxygen is high (see chapter 4.2). This may have an effect on the melting temperature of the clusters. Another possibility is the electron beam induced formation of iron carbide, although this is thermodynamically unstable. Unfortunately, this question cannot be answered satisfactorily.

The samples deposited on quartz substrates were analyzed with UV-VIS spectroscopy. The results are presented in fig. 48. It was not possible to accurately determine the deposition rates for the iron samples, which was probably due to a geometrical problem (the crucible may have not been focussed on the position of the quartz crystal monitor). The spectra are labeled according to the flux measured by the EBE, which is directly proportional to the deposited amount of iron. If the concentration for one sample can be determined by RBS, it is possible to deduce the concentration of the other samples. For a flux of 60 nA the characteristic absorption of the fullerene molecules increases significantly. This behavior is similar to the composite samples of  $C_{60}$  and gold (see chapter 5.1). However, for increasing iron flux, the peaks caused by the fullerene molecules quickly flatten out. The spectra for a flux of 250 nA and 400 nA look similar to those from the germanium samples at higher concentrations (see fig. 47). This indicates a strong interaction of the iron with the surrounding fullerene matrix. The UV-VIS analysis alone is unable to determine if there is a chemical interaction of the iron within the  $C_{60}$  matrix. Due to the problems with the TEM analysis and the indicated instability of the clusters in the  $C_{60}$  matrix, the investigation of the fullerene-iron system was discontinued, because the cooperation of all the different analysis methods is important to obtain satisfactory information on the system. The information on cluster sizes from the TEM analysis is especially important for evaluating information from any other measurement in the 3D systems. For this reason, Mössbauer spectroscopy samples have not been deposited and no detailed RBS analysis has been performed for the Fe- $C_{60}$  system. The desired formation of magnetic iron nanoclusters within a fullerene matrix does not seem likely.

## 6 Summary and outlook

The discovery of the highly stable carbon cluster  $C_{60}$  in the mid 1980s opened up a whole new range of materials research. The unique structure of the highly symmetric molecule provides many different opportunities to modify materials based upon it. The possible doping routes lead to interesting new materials with intriguing physical properties. The creation of such binary cluster materials has been the objective of this work.

Binary cluster materials made up of  $C_{60}$  fullerene molecules and clusters of a foreign species closely resemble exohedrally doped fullerenes, so called fullerides. The long term goal of this work is to find pathways to the formation of ordered 2D and 3D arrays of metal and semiconductor clusters within a fullerene matrix, where the fullerene matrix serves as a "mold" for a large number of material combinations. Four different systems have been investigated in this work. To understand the cluster formation of a certain species within a fullerene matrix, it can be helpful to first investigate the growth of that species on a fullerene surface. For the fullerene-gold system, this was done by depositing sub-monolayer amounts of gold on a fullerene substrate. The growth was observed in between deposition steps by monochromatized x-ray photoelectron spectroscopy (MXPS) and ultra-violet photoelectron spectroscopy (UPS). The substrate signal analysis shows that the growth mode deviates strongly from a layer-by-layer growth mode, which can be described by the Lambert-Beer function. To better understand the bonding of the  $C_{60}$  to the present Au, sub-monolayer amounts of  $C_{60}$  were deposited onto a gold substrate, because this way the valence band features of the fullerene molecules in contact with Au can be observed independently from a fullerene substrate signal. The core level and valence band analysis clearly shows a shift of the fullerene-related features towards lower binding energies for the first layer of  $C_{60}$  molecules. There is no filling of the LUMO, which would be expected in case of a charge transfer from the Au to the fullerene molecules. This indicates a chemisorption of the  $C_{60}$ , which can be described by a covalent bonding of the Au with the  $\pi$ -electron system of the fullerenes. The second layer of  $C_{60}$  shows a band bending effect, that persists even for a deposited nominal coverage of approximately 7 nm.

The analysis of the Au5d band in the VB spectra as well as the shift of the

---

Au $4f_{7/2}$  peak allow the cluster size of the Au deposited on  $C_{60}$  to be determined. The clusters grow with increasing nominal coverage. The smallest clusters are approximately comprised of 50 atoms and for the largest nominal coverages the Au shows bulk features. The film has been annealed *in situ* to test its thermal stability. There is no loss of Au from the surface for moderate annealing temperatures of up to 500 °C, but the cluster size increases due to the annealing. The fullerene desorption is suppressed at this temperature. Annealing above 500 °C leads to a loss of Au from the surface, which could be either due to diffusion into the sample or evaporation of Au from the clusters.

From the 2D surface growth experiment, there are no indications that the fullerene surface provides preferential bonding sites or determines the cluster size. Nevertheless, because of the strong cluster formation on the fullerene surface, the system is a good choice for the extension to a 3D binary cluster material. For this, composite samples made up of  $C_{60}$  and varying amounts of gold were deposited simultaneously under UHV conditions. Transmission electron microscopy (TEM) analysis of the samples shows that Au clusters are formed in each of the samples. From Rutherford backscattering spectroscopy (RBS) it was determined that the Au is distributed throughout the samples. Very narrow size distributions of the clusters are found. They range from about 1.6 nm with a full width at half maximum (fwhm) of 0.5 nm for a gold concentration of 1.5 at% to about 2.5 nm with a fwhm of about 1 nm. With increasing Au concentration the size distribution is broadened and the general cluster size increases. Atomic force microscopy (AFM) reveals that the topography of the samples also depends strongly on the Au concentration. For increasing Au content in the sample, the mean roughness  $R_a$  decreases from 5(1) nm for pure  $C_{60}$  down to 0.2(1) nm for  $C_{60}$  with 25 at% Au. This is well below the diameter of a  $C_{60}$  molecule and could be useful, for example, for the application in opto-electronic devices, because surface roughness is an important factor in the degradation of the optical performance of such devices.

The optical properties of the 3D composite samples of  $C_{60}$  and Au have been investigated with photoluminescence (PL) measurements and UV-VIS spectroscopy. Due to an unexplained artifact in the PL spectra, the possible luminescence of the Au clusters could not be observed. The luminescence of the fullerenes for the different composite samples has been measured. The pure  $C_{60}$  sample shows

luminescence representative of a typical amorphous fullerene thin film. For the composite samples the luminescence is slightly red shifted. The intensity of the zero phonon line (ZPL) is decreasing while the defect luminescence increases with increasing Au content. The reason for the red shift of the PL signal is unclear. Ab initio calculations of the composite systems will be needed to determine the exact role of the Au clusters in the samples. The fact that the PL signal of the  $C_{60}$  is only quenched for the highest Au concentration of 25 *at%* shows that the Au is only weakly interacting with the surrounding fullerene matrix. This is also supported by UV-VIS transmission spectra, which clearly show the characteristic absorption peaks of the  $C_{60}$  molecules for all of the composite samples. This indicates that the fullerene molecules are still intact. As with the PL spectra, detailed simulations of the composite system will be needed to extract the interaction of the Au clusters with the surrounding fullerene matrix.

The investigation of the fullerene gold system has shown, that it is possible to create a binary cluster material made up of  $C_{60}$  and Au by co-evaporation under UHV conditions. The cluster size distribution can be controlled through changing the amount of gold offered during the deposition process. PL and UV-VIS measurements indicate that the interaction of the Au and the surrounding fullerene matrix is minimal. Therefore, it is possible to create evenly distributed Au clusters of a narrow size distribution within the di-electric fullerene matrix.

The usefulness of nanosize clusters as catalysts in a fullerene matrix depends on the permeability of that fullerene matrix with respect to oxygen. To investigate this question, an experiment with a highly reactive metal buried under a few nanometers of  $C_{60}$  was devised. Vanadium is used in the form of vanadium oxide as a catalyst in many applications. The high reactivity of vanadium can be exploited to answer the question of oxygen-permeability of the fullerene matrix, because the different vanadium oxides and the vanadium metal have distinct and clearly separable core levels when investigated using MXPS. A monolayer of vanadium buried underneath 3 *nm*  $C_{60}$  has been employed in this experiment. The sample was exposed to an oxygen atmosphere and the core level spectra show that almost all of the vanadium is oxidized in the process. Further exposure to oxygen does not cause further changes in the core level spectra, showing the high permeability of the fullerene layer with regard to oxygen. The oxide formed in this manner is  $VO_2$ , which is in contrast to



---

the exposure of a surface layer of vanadium to air. The surface layer forms  $V_2O_5$ . Annealing of the two oxidized samples leads to a mixture of oxidation states of the vanadium, and ultimately the layers revert back to their metallic state at a temperature of  $700\text{ }^\circ\text{C}$ . The experiment shows that it should be possible to create a layered structure of  $C_{60}$  and  $VO_2$  by depositing vanadium and  $C_{60}$  in sequence and then exposing the material to oxygen, which will lead to the formation of  $VO_2$ . The creation of a layered  $C_{60}$ - $V_2O_5$  system should also be possible by exposing the freshly deposited surface layers to oxygen before continuing with the  $C_{60}$  deposition.

As with gold, the growth of vanadium on top of a fullerene substrate has been investigated. But unlike gold, vanadium deposited onto  $C_{60}$  shows a layer-by-layer growth. However, due to its high reactivity it is very difficult to obtain pure vanadium films. MXPS always shows oxygen contained in the deposited layer, although it appears to not be bound to the vanadium, as this would be seen in the core level spectra. For nominal coverages in excess of a monolayer of vanadium, the formation of vanadium carbide is observed. The carbide fraction increases with increasing vanadium thickness. Annealing of such an overlayer facilitates the carbide formation. Also, at moderate temperatures of less than  $500\text{ }^\circ\text{C}$ , annealing leads to the partial formation of a vanadium oxide, but most of the vanadium remains in its metallic state. Along with the partial formation of an oxide, the overlayer undergoes some re-configuration. The layer opens up and reveals some of the substrate, which indicates the formation of vanadium oxide islands or clusters.

As the surface of a  $C_{60}$  film is highly corrugated, a vanadium film has also been deposited onto a  $\pi$ -electron-bound flat surface of highly oriented pyrolytic graphite (HOPG) to investigate the possible effect of the surface topography on the overlayer formation and compare two different  $\pi$ -bonded systems. At room temperature, the vanadium overlayer growth does not lead to a strong carbide formation. The layer shows a strong island or cluster growth, clearly deviating from the growth of vanadium on  $C_{60}$ . The reason for the wetting properties of the vanadium and oxygen layer on  $C_{60}$  are not clear. Annealing of the vanadium overlayer on HOPG at  $800\text{ }^\circ\text{C}$  leads to stronger carbide formation than the annealing of vanadium on  $C_{60}$ . This shows that the fullerene molecule is more stable against carbide formation than the graphite layers in HOPG.

The results for the vanadium-fullerene system show, that fullerene films are

highly permeable to oxygen, which is an important property for the creation of possible catalyst clusters within a fullerene matrix. Vanadium grows in a layer-by-layer mode and is capable of breaking up the fullerene molecules, thereby forming vanadium carbide. The vanadium layer can be oxidized after deposition and the oxidation state of the vanadium can be controlled by annealing the sample. The formation of the vanadium oxide leads to a re-organization of the layer, resulting in a cluster or island formation.

The 3D systems of  $C_{60}$  and germanium as well as  $C_{60}$  and iron were investigated. In case of germanium, it was possible to create composite samples with evenly distributed dopants. For neither material the cluster size distribution could be determined due to a variety of experimental problems in imaging these type of systems. For example, it was impossible to obtain high-resolution TEM images for the germanium samples. Most likely this was due to charging of the clusters, which might be oxidized. In the case of iron, clusters could be seen, but seemed to evaporate/disintegrate within seconds due to the electron beam exposure.

Both materials were investigated with UV-VIS spectroscopy. In both cases a strong interaction of the foreign species with the  $C_{60}$  was evident from the elimination of the typical  $C_{60}$  molecular features in the transmission spectra. This could be due to the formation of ionic bonds between the fullerenes and either germanium or iron. For the fullerene-germanium system, this is also supported by PL measurements. None of the composite samples containing germanium showed the typical  $C_{60}$  luminescence.

Since both germanium and iron seem to disrupt the  $C_{60}$  cage structure, the materials do not seem to be suitable candidates for creating binary cluster materials. However, further experiments may be needed to fully understand the role of the iron and the germanium in these systems. The creation of magnetic nanoclusters in a fullerene matrix may still be achieved with a different material like nickel or cobalt, for example.

The next step in the investigation of the presented systems should be to study the possible luminescence of the nanoclusters with a different setup. In addition, further experiments both with gold and vanadium should be conducted to determine the catalytical properties of the materials within a fullerene matrix. The investigated systems have demonstrated the possibility of creating binary cluster

materials employing  $C_{60}$  as a di-electric matrix. This is an encouraging start in the exploration of these materials.

## List of Figures

1	Regular truncated icosahedron and $C_{60}$ molecule. . . . .	6
2	Stereographic projection of $C_{60}$ . . . . .	8
3	American pavilion of the EXPO 1967 in Montreal and commemorative stamp of Buckminster Fuller. . . . .	9
4	$C_{60}$ molecule, showing single bonds ( $a_5$ ) and double bonds ( $a_6$ ). . .	9
5	Some general categories of reactions known to occur with $C_{60}$ . . . .	12
6	Basal plane projection of the low temperature crystal structure of solid $C_{60}$ (space group $Pa\bar{3}$ ) [103] (taken from ref. [7]). . . . .	14
7	Experimental Au cluster absorption spectra. . . . .	16
8	Different crystal structures for exohedral doped alkali metal fullerenes.	24
9	Picture of the UHV chamber constructed for the deposition of composite samples of $C_{60}$ and metals or semiconductors. . . . .	26
10	Top: top view of the UHV chamber. Bottom: view of the inside of the UHV chamber. . . . .	27
11	Sketch of a modern PES experiment. . . . .	30
12	Relationship between the energy levels in a solid and the electron energy distribution produced by photons of energy $\hbar\omega$ . . . . .	31
13	Electron mean free path as a function of their kinetic energy for various metals. . . . .	32
14	Sketch of the three step model. . . . .	35
15	Schematic picture of the Varian Cary 50 spectrometer used for the UV-VIS measurements. . . . .	41
16	Diagram of possible electron transitions in an organic molecule (taken from <a href="http://www.cem.msu.edu">www.cem.msu.edu</a> ). . . . .	41
17	Photoluminescence spectrum of a polycrystalline 300 nm fullerene film.	42
18	Schematic diagram of the luminescence setup (taken from ref. [213]).	43
19	Diagram of a typical TEM setup. . . . .	44
20	Schematic setup of an AFM. . . . .	46
21	Schematic geometry in RBS. . . . .	47
22	PES substrate intensity for $C_{60}$ on Au and vice versa. . . . .	50

---

23	Development of the C1s core level for the deposition of Au on $C_{60}$ and vice versa. . . . .	52
24	Fit results of the C1s core level for $C_{60}$ on Au. . . . .	53
25	PES results for Au on $C_{60}$ . . . . .	55
26	Plot of the binding energy of the Au4f <sub>7/2</sub> core level as a function of the splitting energy of the two main components of the Au5d band. . . . .	57
27	Comparison of UPS VB spectra of $C_{60}$ on Au and vice versa. . . . .	58
28	Results for the annealing of a 0.2 nm Au film. . . . .	61
29	Intensity of the substrate core level as a function of the amount of V deposited onto $C_{60}$ . . . . .	65
30	Core level spectra and UPS VB spectra of the V overlayer formation on $C_{60}$ . . . . .	66
31	Concentration of V, C, and O as a function of the annealing temperature for an overlayer of 0.75 nm V on $C_{60}$ . . . . .	69
32	Overview of core level and UPS spectra taken during annealing of V on $C_{60}$ and V on HOPG. . . . .	70
33	V2p <sub>3/2</sub> core level measured with MXPS for the annealing of 0.75 nm V on $C_{60}$ , normalized to unit height. . . . .	71
34	Intensity of the substrate core level as a function of the amount of V deposited onto HOPG . . . . .	73
35	Overview of core level and UPS spectra measured during <i>in situ</i> and <i>ex situ</i> oxidation of V on top of $C_{60}$ and V buried within a $C_{60}$ film. . . . .	75
36	Intensity of the fullerene substrate C1s core level as a function of the annealing temperature for the <i>ex situ</i> oxidation of 1 ML V on $C_{60}$ . . . . .	76
37	RBS spectrum of the 25 at% Au sample. . . . .	83
38	High resolution TEM micrographs of four Au- $C_{60}$ composite samples with different Au concentrations. . . . .	85
39	Size distribution of the Au clusters for the four different deposited Au concentrations. . . . .	86
40	AFM image of the surface of a composite sample of $C_{60}$ and 11 at% Au. . . . .	87
41	AFM linescans of samples of $C_{60}$ (top), 5 at% Au (second from top), 11 at% Au (third from top), and 25 at% Au (bottom). . . . .	88

---

42	Comparison of the mean roughness $R_a$ with Au cluster size from TEM measurements as a function of nominal coverage. . . . .	89
43	Normalized PL spectra of samples with three different concentrations of Au and a pure $C_{60}$ film. The spectra were taken at $T = 10 K$ . . .	91
44	Normalized transmission spectra of the composite samples. The inset shows the corresponding level scheme of $C_{60}$ (after ref. [252]). . . .	93
45	RBS spectra of two composite samples of $C_{60}$ and Ge. . . . .	95
46	PL spectra for the composite sample of $C_{60}$ and 8 at% Ge. . . . .	96
47	Transmission spectra of composite samples made up of $C_{60}$ and varying concentrations of germanium. . . . .	97
48	Transmission spectra of composite samples of $C_{60}$ and varying concentrations of iron. . . . .	98

## List of Tables

1	Physical constants for $C_{60}$ molecules. . . . .	11
2	Physical constants for crystalline $C_{60}$ in the solid state . . . . .	13
3	Industrial catalytic processes using vanadium oxides [23, 24, 25, 26, 27, 28, 29, 30] (taken from [154]). . . . .	20
4	Overview of the vanadium experiments. . . . .	64
5	Core level binding energies at room temperature of some of the mixed-valence vanadium oxides and metallic vanadium (adapted from ref. [243]). . . . .	71

## References

- [1] J. v. Ruitenbeek, *Metal Clusters at Surfaces*, (Springer-Verlag, Berlin, 2000).
- [2] H.-G. Boyen et al., Phys. Rev. Lett. **87**, 276401 (2001).
- [3] O. Cheshnovsky, K. Taylor, J. Conceicao, and R. Smalley, Phys. Rev. Lett. **64**, 1785 (1990).
- [4] H. Wu, S. Desal, and L.-S. Wang, Phys. Rev. Lett. **76**, 212 (1996).
- [5] M. Lin, R. Andres, and R. Reifengerger, Phys. Rev. Lett. **67**, 477 (1991).
- [6] R. Palmer, S. Pratontep, and H.-G. Boyen, Nature Materials **2**, 443 (2003).
- [7] M. Dresselhaus, G. Dresselhaus, and P. Eklund, *Science of Fullerenes and Carbon Nanotubes*, (Academic Press, 1996).
- [8] M. Abel et al., Phys. Rev. B **67**, 245407 (2003).
- [9] M. Grobis, X. Lu, and M. Crommie, Phys. Rev. B **66**, 161408 (2002).
- [10] D. Klyachko and D. Chen, J. Vac. Sci. Technol. **B15**, 1295 (1997).
- [11] K. Kobayashi, H. Yamada, T. Horiuchi, and K. Matsushige, Appl. Surf. Sci. **157**, 228 (2000).
- [12] P. Reinke and P. Oelhafen, Phys. Rev. B **71**, 045420 (2005).
- [13] P. Reinke, P. Oelhafen, and S. Christiansen, Surf. Sci. **507-510**, 630 (2002).
- [14] T. Lee et al., J. Nanoparticle Research **2**, 345 (2000).
- [15] P. Radojkovic et al., J. Vac. Sci. Technol. B **14**, 1229 (1996).
- [16] X. Hu, D. Sarid, and P. von Blanckenhagen, Nanotechnology **10**, 209 (1999).
- [17] L. Gheber, G. Gorodetsky, and V. Volterra, Thin Solid Films **238**, 1 (1994).
- [18] T. Lee et al., Appl. Phys. Lett. **74**, 2869 (1999).
- [19] T. Lee et al., Appl. Phys. Lett. **76**, 212 (2000).



- 
- [20] T. Irawan, I. Barke, and H. Hövel, *Appl. Phys. A* **80**, 929 (2005).
- [21] H. Fujihara and H. Nakai, *Langmuir* **17**, 6393 (2001).
- [22] N. Vandamme, E. Janssens, F. Vanhoutte, P. Lievens, and C. V. Haesendonck, *J. Phys.: Condens. Matter* **15**, S2983 (2003).
- [23] M. Baltes, *Synthesis and characterization of vanadium oxide catalysts*, PhD thesis, University of Antwerp, Belgium, 2001.
- [24] F. Trifiro, B. Grzybowska-Swierkosz, and J. Viedrine, editors, *Vanadia Catalysts for Selective Oxidation of Hydrocarbons and Their Derivatives*, volume 157 of *J. Appl. Catal.*, 1997.
- [25] G. Bond and D. Thompson, *Catal. Rev.-Sci. Eng.* **41**, 319 (1999).
- [26] G. Deo, I. Wachs, and J. Haber, *Crit. Rev. Surf. Chem.* **4**, 141 (1994).
- [27] G. Ertl, H. Knozinger, and J. Weitkamp, editors, *Handbook of Heterogeneous Catalysis*, (Wiley-VCH, Weinheim, 1997).
- [28] J. Thomas and W. Thomas, *Principles and Practise of Heterogeneous Catalysis*, (Wiley-VCH, Weinheim, 1997).
- [29] J. Hagen, *Industrial Catalysis, A Practical Approach*, (Wiley-VCH, Weinheim, 1999).
- [30] H. Rase, *Handbook of Commercial Catalysis*, (CRC Press, New York, 2000).
- [31] T. Yildirim et al., *Nature* **360**, 568 (1992).
- [32] O. Gunnarsson, *Rev. Mod. Phys.* **69**, 575 (1997).
- [33] C. Gu et al., *Phys. Rev. B* **45**, 6348 (1992).
- [34] Y. Chen, F. Stepniak, J. Weaver, L. Chibante, and R. Smalley, *Phys. Rev. B* **45**, 8845 (1992).
- [35] T. Ohno, G. Kroll, J. Weaver, L. Chibante, and R. Smalley, *Phys. Rev. B* **46**, 10437 (1992).

- 
- [36] L. Quian et al., Phys. Rev. B **59**, 12667 (1999).
- [37] A. Talyzin, H. Högbert, and U. Jansson, Thin Solid Films **405**, 42 (2002).
- [38] A. Talyzin and U. Jansson, Thin Solid Films **429**, 96 (2003).
- [39] M. Haruta et al., J. Catal. **144**, 175 (1993).
- [40] J. Heath, J. Shiang, and P. Alivisatos, J. Chem. Phys. **101**, 1607 (1994).
- [41] L. Saffaro, Proc. of the First Italian Workshop on Fullerenes: Status and Perspectives **2**, 55 (1992).
- [42] F. Chung and S. Sternberg, American Scientist **81**, 56 (1993).
- [43] L. Tisza, Zeitschrift f. Physik **82**, 48 (1933).
- [44] H. Kroto, J. Heath, S. O'Brian, R. Curl, and R. Smalley, Nature **318**, 162 (1985).
- [45] H. Kroto, Chem. Soc. Rev. **11**, 435 (1982).
- [46] E. Herbig, Astrophys. J. **196**, 129 (1975).
- [47] A. Leger and J. Puget, Astr. Astrophys. Lett. **137**, L5 (1984).
- [48] T. Dietz, M. Duncan, D. Powers, and R. Smalley, J. Chem. Phys. **74**, 6511 (1981).
- [49] H. Kroto, Carbon **30**, 1139 (1992).
- [50] R. Curl, Carbon **30**, 1149 (1992).
- [51] R. Marks, *The Dynamics World of Buckminster Fuller*, (Southern Illinois University Press, 1960).
- [52] R. Fuller, *The Artifacts of R. Buckminster Fuller: A Comprehensive Collection of His Designs and Drawings*, (Garland Publishers, Inc., New York, 1984).

- 
- [53] D. Koruga, S. Hameroff, J. Withers, R. Loutfy, and M. Sundareshan, *Fullerene C<sub>60</sub>: History, Physics, Nanobiology, Nanotechnology*, (North-Holland, Amsterdam, 1993).
- [54] D. Thompson, *Growth and Form*, (Cambridge at the University Press, 1963).
- [55] L. Paquette, R. Ternansky, D. Balogh, and G. Kentgen, *J. Am. Chem. Soc.* **105**, 5441 (1983).
- [56] W. David et al., *Nature* **353**, 147 (1991).
- [57] R. Johnson, G. Meijer, and D. Bethune, *J. Am. Chem. Soc.* **112**, 518 (1991).
- [58] R. Johnson, D. Bethune, and C. Yannoni, *Accounts of Chem. Res.* **25**, 169 (1992).
- [59] C. Christides et al., *Phys. Rev. B* **49**, 2897 (1994).
- [60] S. Saito and A. Oshiyama, *Phys. Rev. B* **44**, 11532 (1991).
- [61] H. Beckhaus, C. R uchart, M. Kas, F. Diederich, and C. Foote, *Angew. Chem. int. Edn. engl* **31**, 63 (1992).
- [62] D. Lichtenberger, K. Nebesny, C. Ray, D. Huffman, and L. Lamb, *Chem. Phys. Lett.* **176**, 203 (1991).
- [63] A. Tokmakoff, D. . Haynes, and S. George, *Chem. Phys. Lett.* **186**, 450 (1991).
- [64] G. Dresselhaus, M. Dresselhaus, and J. Mavroides, *Carbon* **4**, 433 (1966).
- [65] J. de Vries et al., *Chem. Phys. Lett.* **188**, 159 (1992).
- [66] H. Steger, J. de Vries, B. Kamke, W. Kamke, and T. Drewello, *Chem. Phys. Lett.* **194**, 452 (1992).
- [67] R. Ruoff and A. Ruoff, *Appl. Phys. Lett.* **59**, 1553 (1991).
- [68] S. Duclos, K. Brister, R. Haddon, A. Kortan, and F. Thiel, *Nature* **351**, 380 (1991).

- 
- [69] R. Haddon, *Science* **261**, 1545 (1993).
- [70] R. Taylor and D. Walton, *Nature* **363**, 685 (1993).
- [71] F. Wudl, *Acc. Chem. Res.* **25** (1992).
- [72] P. Stephens et al., *Nature* **355**, 529 (1991).
- [73] A. Kortan et al., *Nature* **355**, 529 (1992).
- [74] M. Jost et al., *Phys. Rev. B* **44**, 1966 (1991).
- [75] J. Fischer et al., *Science* **252**, 1288 (1991).
- [76] A. Lundin and B. Sundqvist, *Europhys. Lett.* **27**, 463 (1994).
- [77] A. Lundin, B. Sundqvist, P. Skoglund, A. Fransson, and S. Pettersson, *Solid State Commun.* **84**, 879 (1992).
- [78] X. Shi et al., *Phys. Rev. Lett.* **68**, 827 (1992).
- [79] J. Fischer, *Materials Science and Engineering* **B19**, 90 (1993).
- [80] G. Samara et al., *Phys. Rev. Lett.* **67**, 3136 (1991).
- [81] G. Kriza et al., *J. Phys. I, France* **1**, 1361 (1991).
- [82] P. Heiney et al., *Phys. Rev. B* **45**, 4544 (1992).
- [83] A. Rao et al., *Science* **259**, 955 (1993).
- [84] G. Gensterblum et al., *Phys. Rev. B* **50**, 11981 (1994).
- [85] M. Manfredini, C. Bottani, and P. Milani, *Chem. Phys. Lett.* **226**, 600 (1994).
- [86] E. Grivei, B. Nysten, M. Cassart, A. Demain, and J. Issi, *Solid State Commun.* **85**, 73 (1993).
- [87] E. Grivei et al., *Phys. Rev. B* **48**, 8514 (1993).
- [88] R. Yu, N. Tea, M. Salamon, D. Lorens, and R. Malhotra, *Phys. Rev. Lett.* **68**, 2050 (1995).

- 
- [89] C. Wen et al., *Appl. Phys. Lett.* **61**, 2162 (1992).
- [90] S. Ren et al., *Appl. Phys. Lett.* **59**, 2678 (1991).
- [91] Y. Wang et al., *Phys. Rev. B* **45**, 14396 (1992).
- [92] J. Fischer and P. Heiney, *J. Phys. Chem. Solids* **54**, 1725 (1993).
- [93] C. Pan, M. Sampson, Y. Chai, R. Hauge, and J. Margrave, *J. Phys. Chem.* **95**, 2944 (1991).
- [94] E. Kim, Y. Lee, and J. Lee, *Phys. Rev. B* **48**, 18230 (1993).
- [95] S. Woo et al., *Phys. Lett. A* **162**, 501 (1992).
- [96] Y. Wang, D. Tománek, and G. Bertsch, *Phys. Rev. B* **44**, 6562 (1992).
- [97] C. Eom, A. Hebard, L. Trimble, G. Celler, and R. Haddon, *Science* **259**, 1887 (1993).
- [98] C. Yannoni, R. Johnson, G. Meijer, D. Bethune, and J. Salem, *J. Phys. Chem.* **95**, 9 (1991).
- [99] R. Tycko et al., *J. Phys. Chem.* **95**, 518 (1991).
- [100] Q. Zhang, J. Yi, and J. Bernhole, *Phys. Rev. Lett.* **66**, 2633 (1991).
- [101] R. Tycko et al., *Phys. Rev. Lett.* **67**, 1886 (1991).
- [102] R. Johnson, C. Yannoni, H. Dorn, J. Salem, and D. Bethune, *Science* **255**, 1235 (1992).
- [103] K. Prassides et al., *Carbon* **30**, 1277 (1992).
- [104] R. Fleming et al., *Nature* **352**, 787 (1991).
- [105] P. Heiney et al., *Phys. Rev. Lett.* **67**, 1468 (1991).
- [106] R. Moret, S. Ravey, and J. Godard, *J. Phys. I (France)* **2**, 1699 (1992).
- [107] M. Sprik, A. Cheng, and M. Klein, *J. Phys. Chem.* **96**, 2027 (1992).

- 
- [108] C. Yannoni, P. Bernier, D. Bethune, G. Meijer, and J. Salem, *J. Am. Chem. Soc.* **113**, 3190 (1991).
- [109] W. David, R. Ibberson, T. Dennis, J. Hare, and K. Prassides, *Europhys. Lett.* **18**, 219 (1992).
- [110] W. David, R. Ibberson, T. Dennis, J. Hare, and K. Prassides, *Europhys. Lett.* **18**, 735 (1992).
- [111] P. Heiney, *J. Phys. Chem. Solids* **53**, 1333 (1992).
- [112] A. Dworkin et al., *C.R. Acad. Sci., Paris Serie II* **312**, 979 (1991).
- [113] T. Atake et al., *Physica C* **185-189**, 427 (1991).
- [114] T. Matsuo et al., *Solid State Commun.* **83**, 711 (1992).
- [115] Y. Maruyama et al., *Chem. Lett.* **10**, 1849 (1991).
- [116] R. Taylor, J. Hare, A. Abdul-Sada, and H. Kroto, *J. Chem. Soc. Chem. Commun.* **20**, 1423 (1990).
- [117] D. Neumann et al., *Phys. Rev. Lett.* **67**, 3808 (1991).
- [118] L. Pintschovius et al., *Phys. Rev. Lett.* **69**, 2662 (1992).
- [119] D. Neumann et al., *J. Chem. Phys.* **96**, 8631 (1992).
- [120] G. V. Tendeloo, S. Amelinckx, S. Muto, M. V. P. van Loosdrecht, and G. Meijer, *Ultramicroscopy* **51**, 168 (1993).
- [121] S. Hoen et al., *Phys. Rev. B* **46**, 12737 (1992).
- [122] W. Schranz et al., *Phys. Rev. Lett.* **71**, 1561 (1993).
- [123] P. van Loosdrecht, P. van Bentum, and G. Meijer, *Phys. Rev. Lett.* **68**, 1176 (1992).
- [124] P. van Loosdrecht, P. van Bentum, M. Verheijen, and G. Meijer, *Chem. Phys. Lett.* **198**, 587 (1992).

- [125] M. Matus and H. Kuzmany, *Appl. Phys. A* **56**, 241 (1993).
- [126] S. Love et al., *Chem. Phys. Lett.* **225**, 170 (1994).
- [127] F. Gugenberger et al., *Phys. Rev. Lett.* **60**, 3774 (1992).
- [128] G. Mie, *Ann. Phys.* **25**, 377 (1908).
- [129] W. de Heer, W. Knight, M. Chou, and M. Cohen, *Solid State Physics*, volume 40, pages 94–180, (Academic Press, New York, 1987).
- [130] P. Jena, B. Rao, and S. Khanna, editors, *Physics and Chemistry of Small Clusters*, (Plenum, New York, 1987).
- [131] W. de Heer, *Rev. Mod. Phys.* **65**, 611 (1993).
- [132] P. Jena, S. Khanna, and B. Rao, editors, *Physics and Chemistry of Finite Systems: From Clusters to Crystals*, (NATO ASI series, Kluwer, Dordrecht, 1992).
- [133] C. Bréchnac and P. Cahuzac, editors, *Nuclear Aspects of Simple Metal Clusters*, volume 31, (OPA, Amsterdam, 1995).
- [134] H. Haberland, editor, *Clusters of Atoms and Molecules*, volume I+II, (Springer, Berlin, 1995).
- [135] T. Martin, editor, *Large Clusters of Atoms and Molecules*, volume 313 of NATO ASI Series E: Applied Sciences, (Kluwer, Dordrecht, 1996).
- [136] S. Sugano and H. Koizumi, *Microcluster Physics*, volume 20 of Springer Series in Material Sciences, (Springer, Berlin, 1996).
- [137] C. Kittel, *Introduction to Solid State Physics*, (Wiley, New York, 1976).
- [138] U. Kreibig and M. Vollmer, *Optical Properties of Metal Clusters*, (Springer, Berlin, 1995).
- [139] M. Alvarez et al., *J. Phys. Chem.* **101**, 3706 (1997).
- [140] K. Meiwes-Broer, *Metal clusters at surfaces*, Springer Verlag, Berlin, 2000.

- 
- [141] V. Kresin, Phys. Rep. **220**, 1 (1992).
- [142] W. de Heer et al., Phys. Rev. Lett. **59**, 1805 (1987).
- [143] A. Kawabata and R. Kubo, J. Phys. Soc. Jap. **21**, 1765 (1966).
- [144] C. Yannouleas, Nucl. Phys. A **439**, 336 (1985).
- [145] C. Yannouleas and R. Broglia, Ann. Phys. **217**, 105 (1992).
- [146] N. Ashcroft and N. Mermin, *Solid State Physics*, (Holt, Rinehart and Winston, New York, 1976).
- [147] V. Bonačić-Koutecký, P. Fantucci, and J. Koutecký, Chem. Rev. **91**, 1035 (1991).
- [148] R. Johnston, *Atomic and Molecular Clusters*, (Taylor & Francis, London, 2002).
- [149] W. Knight et al., Chem. Phys. Lett. **134**, 1 (1987).
- [150] K. Koga, H. Takeo, T. Ikeda, and K. Oshima, Phys. Rev. B **57**, 4053 (1998).
- [151] H.-G. Boyen et al., Phys. Rev. Lett. **94**, 016804 (2005).
- [152] M. Zayats, R. Baron, I. Popov, and I. Willner, Nano Letters **5**, 21 (2005).
- [153] M. Haruta, The Chemical Record **3**, 75 (2003).
- [154] B. Weckhuysen and D. Keller, Catal. Today **78**, 25 (2003).
- [155] J. Magee and M. Mitchel, Stud. Surf. Sci. Catal. **76**, 105 (1993).
- [156] A. Putris and R. Liebermann, editors, *Mineralogical Applications of Crystal Field Theory, 2nd edition*, (Cambridge University Press, Cambridge, 1993).
- [157] F. Tast et al., Phys. Rev. Lett. **77**, 3529 (1996).
- [158] A. Nakajima, S. Nagao, H. Takeda, T. Kurikawa, and K. Kaya, J. Chem. Phys. **107**, 6491 (1997).



- 
- [159] T. Takagahara and K. Takeda, *Phys. Rev. B* **46**, 15578 (1992).
- [160] S. Hayashi, M. Fujii, and K. Yamamoto, *Jpn. J. Appl. Phys., Part 2* **28**, L1464 (1989).
- [161] Y. Maeda, N. Tsukamoto, Y. Yazawa, Y. Kanemitsu, and Y. Masumoto, *Appl. Phys. Lett.* **59**, 3168 (1991).
- [162] Y. Kanemitsu, H. Uto, Y. Masumoto, and Y. Maeda, *Appl. Phys. Lett.* **61**, 2187 (1992).
- [163] M. Zacharias and P. Fauchert, *Appl. Phys. Lett.* **71**, 380 (1997).
- [164] S.-T. Ngiam, K. Jensen, and K. Kolenbrander, *J. Appl. Phys.* **76**, 8201 (1994).
- [165] M. Nogami and Y. Abe, *Appl. Phys. Lett.* **65**, 2545 (1994).
- [166] J. Zhu, C. White, J. Budai, and S. Withrow, *J. Appl. Phys.* **78**, 4386 (1995).
- [167] J. Wilcoxon, P. Provencio, and G. Samara, *Phys. Rev. B* **64**, 035417 (2001).
- [168] J. Lohau, A. Carl, S. Kirsch, and E. Wassermann, *Appl. Phys. Lett.* **78**, 2020 (2001).
- [169] W. Wernsdorfer et al., *Phys. Rev. Lett.* **78**, 1791 (1997).
- [170] R. Cowburn, D. Koltsov, A. Adeyeye, and M. Welland, *Appl. Phys. Lett.* **73**, 3947 (1998).
- [171] R. Cowburn, D. Koltsov, A. Adeyeye, M. Welland, and D. Tricker, *Phys. Rev. Lett.* **83**, 1042 (1999).
- [172] V. Novosad et al., *Phys. Rev. B* **65**, 060402 (2002).
- [173] M. Hwang et al., *J. Appl. Phys.* **87**, 5108 (2000).
- [174] E. Petrakovskaya, V. Isakova, O. Bayukov, and D. Velikanov, *Techn. Phys.* **50**, 790 (2005).
- [175] D. Bethune et al., *Nature* **366**, 123 (1993).

- 
- [176] R. Smalley, *Materials Science and Engineering* **B19**, 1 (1993).
- [177] J. Heath et al., *J. Am. Chem. Soc.* **107**, 7779 (1985).
- [178] A. Rosén and B. Wästberg, *J. Am. Chem. Soc.* **110**, 8701 (1988).
- [179] G. Hammond and V. Kuck, editors, *Large Carbon Clusters*, page 199, (American Chemical Society, Washington, DC, 1991).
- [180] D. Poirier et al., *Phys. Rev. B* **49**, 17403 (1994).
- [181] H. Shinohara et al., *Materials Science and Engineering* **B19**, 25 (1993).
- [182] L. Turker, *J. Molecular Structure - Theochem* **593**, 149 (2002).
- [183] L. Turker, *J. Molecular Structure - Theochem* **624**, 233 (2003).
- [184] Y. Miyamoto, A. Oshiyama, and S. Saito, *Solid State Commun.* **82**, 437 (1992).
- [185] Y. Miyamoto, N. Hamada, A. Oshiyama, and S. Saito, *Phys. Rev. B* **46**, 1749 (1992).
- [186] R. Averback, J. Bernholc, and D. Nelson, editors, *Clusters and Cluster-Assembled Materials, MRS Symposia Proceedings, Boston*, volume 206, pages 691–696, (Materials Research Society Press, Pittsburgh, PA, 1991).
- [187] G. Wertheim and D. Buchanan, *Solid State Commun.* **88**, 97 (1993).
- [188] Q. Zhu et al., *Science* **254**, 545 (1992).
- [189] P. Stephens et al., *Phys. Rev. B* **45**, 543 (1992).
- [190] D. Poirier, *Appl. Phys. Lett.* **64**, 1356 (1993).
- [191] G. Sauerbrey, *Phys. Verhandlungen* **8**, 193 (1957).
- [192] G. Sauerbrey, *Z. Phys.* **155**, 206 (1959).
- [193] P. Lostis, *Rev. Opt.* **38**, 1 (1959).

- 
- [194] H. Hertz, *Ann. Physik* **31**, 983 (1887).
- [195] S. Hüfner, *Photoelectron Spectroscopy - Principles and Applications*, (Springer-Verlag, Berlin, 2003).
- [196] A. Einstein, *Ann. Physik* **17**, 132 (1905).
- [197] H. Ibach, *Electron Spectroscopy for Surface Analysis*, (Springer Verlag, Berlin, Heidelberg 1977).
- [198] P. Reinke and P. Oelhafen, *J. Chem. Phys.* **116**, 9850 (2002).
- [199] M. Seah and W. Dench, *Surf. Interface Anal.* **1**, 2 (1979).
- [200] K. Siegbahn et al., *ESCA, Atomic, Molecular, and Solid State Structure Studies by Means of Electron Spectroscopy*, (Nova Acta Regiae Soc. Sci., Upsaliensis, Ser. IV, Vol. 20, 1967).
- [201] C. Fadley, *Electron Spectroscopy: Theory, Techniques and Applications II*, (Academic, New York, 1978).
- [202] W. Bardyszewski and L. Hedin, *Phys. Scripta* **32**, 439 (1985).
- [203] C. Almladh and L. Hedin, *Handbook on Synchrotron Radiation, Vol. 1b*, North-Holland, Amsterdam, 1983.
- [204] L. Hedin and S. Lundquist, *Solid State Physics* **23**, 1 (1969).
- [205] J. Braun, *Rep. Prog. Phys.* **59**, 1267 (1996).
- [206] A. Kotani, T. Jo, and C. Parlebas, *Adv. Phys.* **37**, 37 (1988).
- [207] L. Hedin, *J. Phys. Condens. Matter* **11 R**, 489 (1999).
- [208] L. Hedin, J. Michiels, and J. Inglesfield, *Phys. Rev. B* **58**, 15565 (1998).
- [209] G. Wertheim, S. DiCenzo, and S. Youngquist, *Phys. Rev. Lett.* **51**, 2310 (1983).
- [210] G. Wertheim and S. DiCenzo, *Phys. Rev. B* **37**, 844 (1988).

- [211] H. H. B. Grimm, M. Pollmann, and B. Reihl, *Phys. Rev. Lett.* **81**, 4608 (1998).
- [212] V. Capozzi, G. Celentano, G. Perna, G. Lorusso, and A. Minafra, *J. Luminescence* **86**, 129 (2000).
- [213] U. Vetter, *Lanthanide Doped Wide Band Gap Semiconductors: Intra-4f Luminescence and Lattice Location Studies*, PhD thesis, Universität Göttingen, Germany, 2003.
- [214] D. Schwen, *Untersuchungen zur Feldemission von Ionenspuren in diamantähnlichem Kohlenstoff*, (Diploma thesis, Universität Göttingen, 2002, unpublished).
- [215] Q. Zhong, D. Innis, K. Kjoller, and V. Elings, *Surf. Sci. Lett.* **290**, L688 (1993).
- [216] S. Gąsiorek, *Solid Phase Epitaxial Regrowth of alkali ion irradiated  $\alpha$ -quartz*, PhD thesis, Universität Göttingen, Germany, 2003.
- [217] M. Uhrmacher, K. Pampus, F. Bergmeister, D. Purschke, and K. Lieb, *Nucl. Instrum. Meth. B* **9**, 234 (1985).
- [218] J. Ziegler, *The Stopping and Ranges of Ions in Matter*, New York, Vol. 4, 1977.
- [219] N. Bohr, *Mat. Fys. Medd. Dan. Vid. Selsk* **18**, 8 (1948).
- [220] N. Barradas, C. Jaynes, and R. Webb, *Appl. Phys. Lett.* **71**, 291 (1997).
- [221] H. Kröger, P. Reinke, M. Büttner, and P. Oelhafen, *J. Chem. Phys.* **123**, 114706 (2005).
- [222] P. Reinke, H. Feldermann, and P. Oelhafen, *J. Chem. Phys.* **119**, 12547 (2003).
- [223] M. Kawasaki, Y. Matsuzaki, and H. Koinuma, *Phys. Rev. B* **39**, 13316 (1989).
- [224] K. Narumi and H. Naramoto, *Diamond Relat. Mater.* **10**, 980 (2001).

- 
- [225] S. Guo, D. Fogarty, P. Nagel, and S. Kandel, *J. Phys. Chem. B* **108**, 14074 (2004).
- [226] W. Xu, *J. Crystal Growth* **220**, 96 (2000).
- [227] A. Kuzume, E. Herrero, J. Felin, R. Nichols, and D. Schiffrin, *Phys. Chem. Chem. Phys.* **6**, 619 (2004).
- [228] J. Yao, Y. Zou, X. Zhang, and G. Chen, *Thin Solid Films* **305**, 22 (1997).
- [229] S. Doniach and M. Sunjic, *J. Phys. C* **3**, 285 (1970).
- [230] D. Shirley, *Phys. Rev. B* **5**, 4709 (1972).
- [231] D. Marquardt, *J. Spc. Ind. Appl. Math.* **11**, 431 (1963).
- [232] M. Seidl, K.-H. Meiwes-Broer, and M. Brack, *J. Chem. Phys.* **95**, 1295 (1991).
- [233] S. DiCenzo, S. Berry, and E. H. Jr., *Phys. Rev. B* **38**, 8465 (1988).
- [234] B. Hoogenboom, R. Hesper, L. Tjeng, and G. Sawatzky, *Phys. Rev. B* **57**, 11939 (1998).
- [235] T. Ohno et al., *Phys. Rev. B* **44**, 13474 (1991).
- [236] J. Gimzewski, S. Modesti, and R. Schlittler, *Phys. Rev. Lett.* **72**, 1036 (1994).
- [237] T. Ohno et al., *Phys. Rev. B* **47**, 2389 (1993).
- [238] S. Didziulis and P. Frantz, *J. Phys. Chem. B* **105**, 5196 (2001).
- [239] P. Frantz and S. Didziulis, *Surf. Sci.* **412/413**, 384 (1998).
- [240] F. Beguin et al., *Eur. Polym. J.* **34**, 905 (1998).
- [241] C. Cardinaud, G. Lemperiere, M. Peignon, and P. Jouan, *Appl. Surf. Sci.* **68**, 595 (1993).
- [242] M. Demeter, M. Neumann, and W. Reichelt, *Surf. Sci.* **454-456**, 41 (2000).
- [243] G. Sawatzky and D. Post, *Phys. Rev. B* **20**, 1546 (1979).

- 
- [244] B. Dzhurinskii, D. Gati, N. Sergushin, V. Nefedov, and Y. Salyn, *Russ. J. of Inorganic Chem.* **20**, 2307 (1975).
- [245] E. Thune, E. Carpena, K. Sauthoff, M. Seibt, and P. Reinke, *J. Appl. Phys.* **98**, 034304 (2005).
- [246] B. Palpant et al., *Phys. Rev. B* **57**, 1963 (1998).
- [247] M.-K. Kim et al., *Chem. Comm.* **7**, 667 (2001).
- [248] P. Pengo, S. Polizzi, M. Battagliarin, L. Pasquato, and P. Scrimin, *J. Mater. Chem.* **13**, 2471 (2003).
- [249] J. Wilcoxon, J. Martin, F. Parsapour, B. Wiedenman, and D. Kelley, *J. Chem. Phys.* **108**, 9137 (1998).
- [250] E. Shin et al., *Chem. Phys. Lett.* **209**, 427 (1993).
- [251] V. Capozzi, T. Trovato, H. Berger, and G. Lorusso, *Carbon* **35**, 763 (1997).
- [252] V. Capozzi et al., *Solid State Commun.* **98**, 853 (1996).
- [253] F. Ding, K. Bolton, and A. Rosén, *Eur. Phys. J. D* **34**, 275 (2004).
- [254] F. Ding, A. Rosén, and K. Bolton, *Phys. Rev. B* **70**, 075416 (2004).

## Acknowledgments

Zunächst möchte ich mich bei meiner Doktormutter Frau Professor Doktor Petra Reinke für die freundschaftliche Betreuung und Unterstützung während meiner gesamten Promotionszeit bedanken. Trotz der sechs Stunden Zeitverschiebung kam mir Virginia nie allzu weit entfernt vor, und ich hoffe, dass das auch in Zukunft so bleiben wird.

Herrn Professor Doktor Reiner Kirchheim danke ich dafür, diese Arbeit zu begutachten.

Bei Professor Doktor Hans Christian Hofsäss möchte ich mich dafür bedanken, dass er in Petras Abwesenheit für meine lokale Betreuung eingesprungen ist.

Michael Büttner und Professor Peter Oelhafen möchte ich für die Zusammenarbeit bei den PES Experimenten in Basel danken, ohne die ein Grossteil dieser Arbeit nicht möglich gewesen wäre.

Für eine unglaublich leckere Hochzeitstorte gebührt mein Dank Inga Hannstein. Dazu kommen noch die unerwartete Ausweitung der Übersetzungstätigkeit, für die meine Schwiegereltern sicherlich auch extrem dankbar gewesen sind. Nicht zu vergessen sind natürlich auch die TEM Bilder, die meine Arbeit sehr voran gebracht haben.

Sören Eyhusen und Daniel Schwen danke ich für die stete Versorgung mit immer neuen Serien, die die gewisse zuweilen nötige Ablenkung in den letzten Jahren gewährleistet haben.

For keeping me company during lunchtime, I would like to express my thanks to Velimir Milinović. Also, the help with the RBS measurements will not be forgotten.

Daniel Stichtenoth und Gregor Oehl möchte ich für die Unterstützung bei den PL Messungen danken.

Bei Dong Du Mai und Jan Müller bedanke ich mich für die Hilfe mit den AFM Messungen.

Ein besonderer Dank gebührt den Werkstätten des 2. Physikalischen Instituts für die grosse Hilfsbereitschaft bei der Lösung all der vielen Probleme, die ich in den letzten Jahren so gehabt habe. Stellvertretend seien hier nur die beiden Werkstatteleiter Klaus Arndt und Kurt Schemmerling genannt. Andreas König gebührt in diesem Zusammenhang auch mein spezieller Dank, da er irgendwie meistens an

meinen zahlreichen Aufträgen hängengeblieben ist.

Die Bewältigung all der kleinen und grossen Alltagsprobleme wäre ohne Christa Wohlfarth, Lucie Hamdi und Heike Ahrens wohl deutlich schwieriger gewesen. Vielen Dank für all die Hilfe in den letzten Jahren.

Bei all meinen Freunden möchte ich mich für die Unterstützung während meines gesamten Studiums bedanken. Danke für all die schönen Jahre!

Meiner Mutter Hannelore Kröger und ihrem Verlobten Helmut Ohlsen möchte ich von ganzem Herzen danken für die uneingeschränkte Unterstützung, die Liebe und den festen Glauben an mich. Ohne Euch wäre diese Arbeit nicht möglich gewesen.

Last but not least, I want to thank my wife Emily. I wouldn't have made it without your support and love. Thank you for believing in me and helping me to believe in myself. You are the love of my life!



## Lebenslauf

Name	Helge Kröger
Geburtstag	14. Juni 1975
Geburtsort	Flensburg, Deutschland
Nationalität	deutsch
Familienstand	verheiratet

## Bildungsweg

1982-1986	Grundschule Tarp
1986-1995	Besuch des Gymnasiums Satrup, Abschluß Abitur
Ab 10/1996	Studium der Physik an der Georg-August Universität Göttingen
10/1998	Vordiplom in Physik an der Georg-August Universität Göttingen,
11/2001	Diplom in Physik, Titel der Diplomarbeit: Fremdatom- und Eigendiffusion in amorphen Kohlenstoffen
Seit 12/2001	Wissenschaftlicher Angestellter am 2. Physikalischen Institut der Universität Göttingen